

Study of ω Resonance Abundance
in 158 A GeV Pb + Pb Collisions at CERN-SPS

Susumu SATO

January, 2001

Study of ω Resonance Abundance
in 158 A GeV Pb + Pb Collisions at CERN-SPS

Susumu SATO

A dissertation submitted to the Doctoral Program
in Physics, the University of Tsukuba
in partial fulfillment of the requirements
for the degree of Doctor of Philosophy (Science)

January, 2001

Abstract

We present the results of single particle spectra and direct measurement of Δ resonance yield in $p\pi^+$ decay channel in Pb + Pb collisions at the energy of 158 A GeV, at WA98 experiment using Super Proton Synchrotron (SPS) of the European organization for nuclear research (CERN).

For systematic study of hadron production in relativistic heavy ion collisions near mid rapidity region, we have constructed a magnetic spectrometer, called Arm-II. It is designed for good particle identification capability under the condition of high particle density and for large momentum coverage in Pb + Pb collisions at SPS. Using the data taken by the Arm-II spectrometer, single particle spectra and Δ resonance yield are analyzed.

For the single particle, we have carried out the analysis of transverse kinetic energy spectra for π^+ and proton. By using single exponential fitting, inverse slope parameter is 142 ± 3 MeV (fitting region $m_t - m > 0.2$ GeV), and 251 ± 25 MeV. In the transverse kinetic energy spectra of pion, we have observed clear low- m_t enhancement.

We have evaluated Δ resonance yield with $p\pi^+$ invariant mass distribution. Considering the isospin asymmetry in incident $^{208}\text{Pb}^{82+}$ nuclei, $\Delta/\text{nucleon}$ ratio is determined as $0.62 \pm 0.28(\text{stat.}) \pm 0.16(\text{sys.})$. This ratio is larger than those measured in the lower beam energy.

Motivated by partial success of collective expanding fireball model, which can explain both single particle spectra and HBT correlation but cannot describe low m_t region in pion spectra, different kinds of contributions are considered. Those are collective motion, the Coulomb effect, and contribution of Δ resonance. As the collective motion and the Coulomb effects are qualitatively smaller than the observed low m_t enhancement, the contribution of Δ resonance is therefore studied. Using the value of temperature and collective velocity, evaluated from single particle spectra and HBT measurement, about 1.5 times more contribution from Δ resonance than measured in the invariant mass is used to follow the shape of pion spectra. The factor is consistent with the results of a cascade simulation. The simulation tells the factor comes from such Δ resonance that decays into proton which is re-scattered and pion which is, however, not re-scattered after decay, and those Δ resonances are not measured in the invariant mass.

Contents

1. Introduction.....	5
1.1 Geometry of Relativistic Heavy Ion Collisions.....	6
1.2 Features of Particle Production Observed in Relativistic Heavy Ion Collisions.....	8
1.2.1 Single-Particle Spectra.....	9
1.2.2 Two-Particle Correlation.....	12
1.2.3 Interpretation with Expanding Fireball Model.....	14
1.3 Delta Resonance.....	19
1.3.1 Delta Resonance in Relativistic Heavy Ion Collisions.....	20
1.3.2 Low m_t Enhancement and Delta Resonance.....	21
1.3.3 Delta Resonance Measurement at SPS Energy.....	22
1.4 Thesis Motivation.....	23
2. Experimental Setup.....	25
2.1 CERN-SPS Accelerator.....	25
2.1.1 Ion Source (Electron Cyclotron Resonance: ECR).....	26
2.1.2 Linac, Boosters and Synchrotrons (PS and SPS).....	26
2.2 WA98 Experiment.....	27
2.2.1 Target.....	28
2.2.2 Magnetic Spectrometer.....	28
2.2.2.1 Magnet: GOLIATH.....	29
2.2.2.2 Pad Chamber: PAD.....	29
2.2.2.3 Steamer Tube Detector: STD.....	31
2.2.2.4 Start Counter: STR.....	32
2.2.2.5 Time of Flight Detector (in Arm-II): JTOF.....	33
2.2.3 Global Detector.....	35
2.2.3.1 Mid-Rapidity Calorimeter: MIRAC.....	35
2.2.3.2 Zero Degree Calorimeter: ZDC.....	35

3.	Data Analysis	37
3.1	Clustering of Hits.	37
3.2	Track Reconstruction	39
3.3	Momentum Reconstruction and Flight Path Length Calculation....	41
3.4	Time of Flight Calibration	45
3.5	Particle Identification	49
3.6	Event Selection.....	52
3.7	Invariant Mass Spectra	53
3.8	Acceptance, Efficiency, and Decay Correction	58
3.9	Isospin Consideration	61
4.	Experimental Results	63
4.1	Error Evaluation.....	63
4.1.1	Statistical Fluctuation in Subtraction of Combinatorial Background.....	63
4.1.2	Fitting Method Dependence in Subtraction of Combinatorial Background.....	65
4.1.3	Dependence on Local Multiplicity	66
4.2	Transverse Momentum Distribution	68
4.3	Δ /Nucleon Ratio.....	70
5.	Discussions.....	73
5.1	\ddot{A} /Nucleon Ratio.....	73
5.2	Single-Particle Spectra and Two-Particle Correlation in Expanding Fireball Picture.	75
5.3	Low m_t Enhancement of Pion Spectra	77
5.3.1	Proton - Proton Collision.....	78
5.3.2	Source of Low mt Enhancement	79
5.3.2.1	Collective Motion.....	80
5.3.2.2	Coulomb Effects	82
5.3.2.3	Contribution from Resonances	83

6. Conclusions.....	87
7. References	88
Appendix A: Relativistic Heavy Ion Accelerators.....	93
Appendix B: Examples of Calculation	94
Appendix C: Parameters Used in Relativistic Kinematics	96
Appendix D: WA98 Experiment Coordinate System	97
Appendix E: Other Detectors in WA98.....	99
Appendix F: Selection of Radiator of Start Counter for Heavy Ion Beam...	105
ACKNOWLEDGEMENTS	107
PUBLISHED PAPER	109
" Δ^{++} production in 158 A GeV $^{208}\text{Pb} + ^{208}\text{Pb}$ interactions at the CERN SPS" (Physics Letters B 477 (2000) 37 - 44)	

1. Introduction

In this chapter, current understanding of particle production in relativistic heavy ion collisions to study of extremely hot and dense nuclear states is described. And as an experimental probe of the state, delta resonance is introduced

In the relativistic heavy ion collisions, hundreds of incident nucleus are interacting for short time period of the order of fm/c in a finite volume of the order of tens fm³. This condition initiates extremely hot and dense nuclear states. Such hot and dense states are expected to exist at the beginning of the universe. To study and characterize high density and high temperature states of nuclear matter on the earth, an effective way is to collide relativistic heavy ions using accelerators. With this motivation, heavy ion accelerators have been constructed or modified from existing proton accelerators. Those are CERN-SPS or BNL-AGS. Using the accelerators, unique features of nuclear matter in particle productions in relativistic heavy ion collisions, like *J/Y suppression*, enhancement of low mass lepton pairs, or collective phenomena, are observed experimentally [e.g. W⁹⁸⁻⁹⁸, N⁴⁴⁻⁹⁶, N⁵⁰⁻⁹⁷, N⁴⁵⁻⁹⁹]. Also lots of theoretical interpretation of these features are reported, including a phase transition to a new phase of matter, called *quark - gluon - plasma*, where the constituent quarks and gluons move asymptotically free [e.g. M^{S-86}, M^{u-85}].

In relativistic heavy ion collisions, collision geometry determines features of observables. A naive geometrical picture of collision, called *participant - spectator model*, is necessary to understand the observables. The picture is described in section 1.1 .

In the next section 1.2 , features of relativistic heavy ion collisions have been studied through observables, like *single particle spectra* and *two - particle correlations*. Trial for systematic description of the observables is introduced. And a disagreement of the description in low transverse kinetic energy regions of pion spectra is pointed out.

The difference between relativistic heavy ion collisions and nucleon - nucleon collisions are discussed in the following section. For this viewpoint, study of delta resonance is introduced in section 1.3 . And a description with the delta resonance for an explanation of the disagreement in pion spectra is

raised.

In the last of this chapter, the thesis motivation is described (sect. 1.4)

1.1 Geometry of Relativistic Heavy Ion Collisions

In relativistic heavy ion collisions, the size of colliding system varies depending on an impact parameter and the evolution of colliding system is known to depending on the size of the system. Since the incoming angular momentum (e.g. 60 GeV fm/c for 158 A GeV Pb + Pb collisions around the center of mass) is much larger than the typical quantum scale, ~ 0.2 GeV fm/c, the impact parameter can be treated as a classical quantity. With the parameter, measured data in relativistic heavy ion collisions should be sorted. When the impact parameter, b , is about a sum of radii of the nuclei, both nuclei are touching on the surface at most closest point, and only the nucleons in this surface will be involved in the collisions. Such collision is called *peripheral collision*. On the contrary, when the impact parameter is zero, most of the nucleons will be involved in the collisions. Such an event is called *central collision*.

In a naive picture for non-central collision, there are two domains for colliding nuclei. One is overlapping part of the incident nuclei which develops into hot and/or dense nuclear matter called *fireball*. Schematic picture before, during, and after collision is shown in Fig. 1 (top, middle, and bottom drawings respectively). In the figure, impact parameter, b , is also shown. Nucleons in the overlapping region (shown as hatched region in the figure) are called *participants*. The other remaining parts, which pass away from the fireball in early stage of the collision, are called *spectators* (shown as P and T in black letter as a projectile spectator and a target spectator, respectively). This naive geometrical picture holds because of the following two reasons.

- (1) Elementary process of nucleus - nucleus collisions is nucleon - nucleon collisions, because the de Broglie wavelength of incident nuclei, λ_{dB} , is much shorter than the size of nuclei, $2r$.
(E.g. $\lambda_{dB} < 1$ fm and $2r \sim 14$ fm for 158 A GeV Pb + Pb collisions in the center of mass frame)
- (2) Each constituent nucleon collides dominantly with nucleons located in tubular region with about nucleon radius and with length in the incident momentum direction. Because collision time, Dt_{col} , is much

shorter than the traversing time, Dt_T , for a nucleon to reach the next (in perpendicular to incident momentum) nucleon.

(E.g. $Dt_{col} < 1$ fm/c and $Dt_T \sim 7$ fm/c for 158 A GeV Pb + Pb collisions in center of mass frame)

With these three reasons, in relativistic heavy ion collisions, geometrical separation of nucleons in participant region and nucleons in spectator regions is considered as a good approximation.

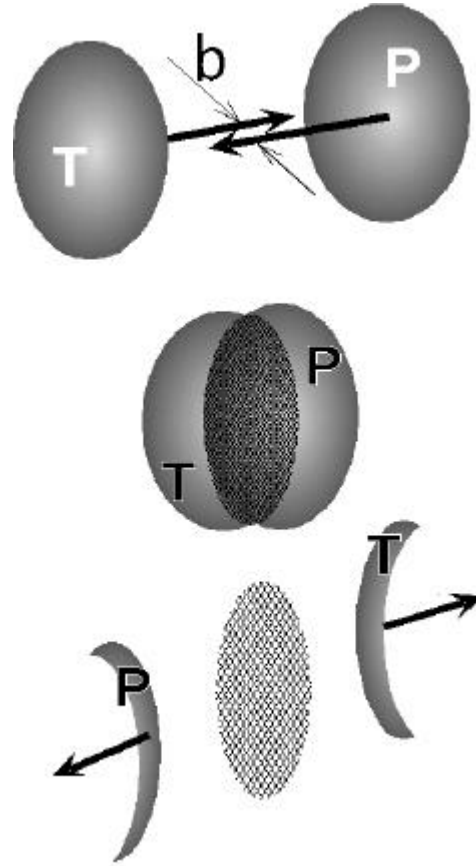


Fig. 1: Schematic picture of relativistic heavy ion collision before (top), during (middle), and after (bottom) the collision. Note that the projectile (P) and the target (T) are Lorentz contracted in their center of mass frame. Hatched regions indicate hot and/or dense fireball. Impact parameter, b , is also shown.

In Fig. 2, dN/dy distribution of protons and anti-protons are shown for 158 A GeV Pb + Pb central (top 5% of minimum bias) collisions. Here rapidity, y , is defined as,

$$y = \frac{1}{2} \ln \left\{ \frac{E + p_{\parallel}}{E - p_{\parallel}} \right\},$$

where E is the total energy, p_{\parallel} is the longitudinal component of the momentum. Rapidity difference, Dy , is Lorentz invariant. Rapidity of the center of mass is defined as zero in the figure. Note that rapidity difference between the beam (or the target) and the center of mass at the SPS beam energy is 2.91.

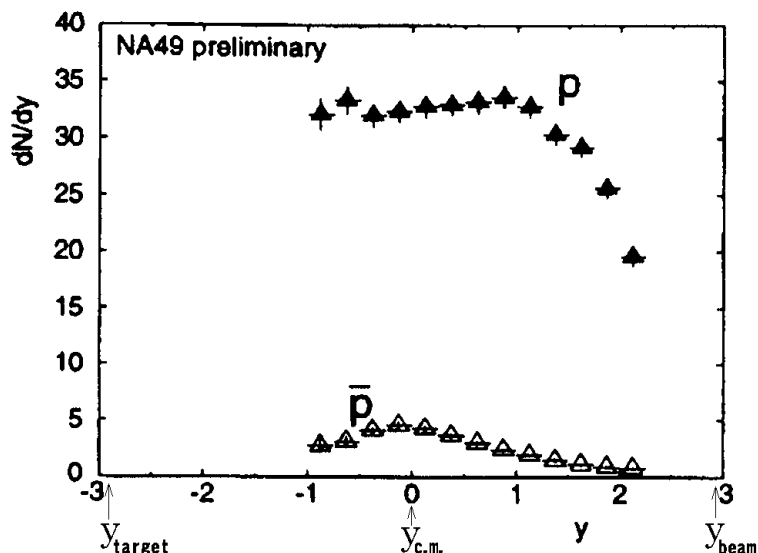


Fig. 2: Baryon rapidity distributions at SPS energy in 158 A GeV $^{208}\text{Pb}^{82+} - ^{208}\text{Pb}^{82+}$ central (top 5%) collisions [N 49-99]. As Dy is Lorentz invariant, rapidity of the center of mass is taken as zero. Note that rapidity difference between the beam (or the target) and the center of mass at the SPS beam energy is 2.91.

Participant nucleons are emitted around mid rapidity. About 35 protons in dN/dy , are emitted in the mid rapidity. By subtracting small yield of anti-particles, net protons correspond to the participant.

1.2 Features of Particle Production Observed in Relativistic Heavy Ion Collisions

Inclusive single particle spectra and two-particles correlations for identified particle should give basic clue to study characteristics of the hot and dense fireball. An interpretation of single particle spectra and two-particle correlation with expanding fireball model is useful to depict collision dynamics of the relativistic heavy ion collisions.

1.2.1 Single-Particle Spectra

Transverse momentum, p_t , has been measured inclusively for various particle species not only in nucleus - nucleus collisions but also in proton - nucleus and in proton - proton collisions. The spectrum is known to be well described in *transverse kinetic energy*, $m_t - m$, rather than the transverse momentum, where m_t is a function of p_t as follows.

$$m_t = \sqrt{p_t^2 + m^2},$$

where m is the rest mass of particle. In proton - proton collisions and proton - nucleus collisions, invariant cross sections show simple exponential shapes in $m_t - m$. And the m_t slope is found to be very similar for various particle species. These phenomena are often called as *m_t -scaling* [BSM-76, A⁺-77, C^r-78]. One of the example of the m_t scaling is shown in Fig. 3 [B^S-75]. The horizontal axis is the transverse kinetic energy, $m_t - m$, and the vertical axis is the invariant cross section. This is plotted for protons, positive kaons, and positive pions in proton - proton collisions at $s^{1/2} = 23$ GeV. Absolute values for kaons and pions are multiplied by 1/1.5 and 1/35, respectively, to show the similarity of the shape. The dashed line is an exponential line for an eye guide. Clear m_t scaling is seen in this collision. As an interpretation of the m_t scaling [Mⁱ-79, H^a-83, T^a-85], a local thermal equilibrium is often assumed where the inverse slope of spectra is considered as the temperature.

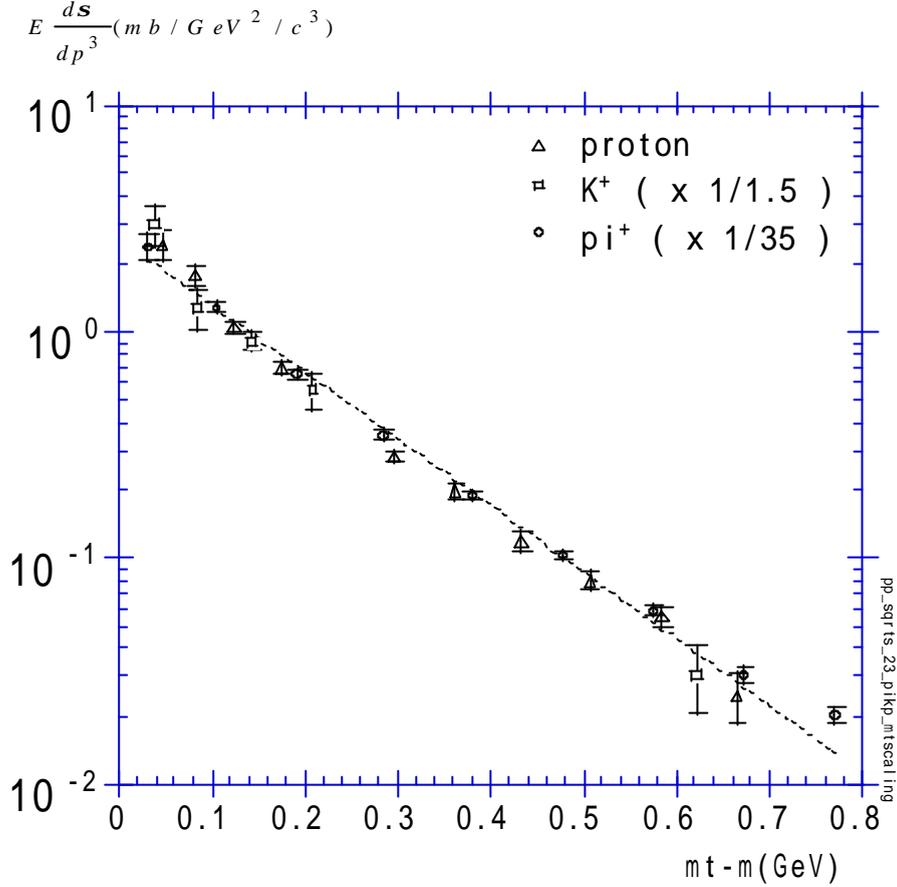


Fig. 3: Invariant cross section of proton and K^+ , and p^+ in proton - proton collisions at $s^{1/2} = 23$ GeV [B^S-75]. Scaling in transverse kinetic energy, m_t , can be seen for different particle species. The dashed line is an eye guide in exponential function in m_t .

Fig. 4 shows inclusive m_t spectra in 158 A GeV Pb + Pb central of collisions for different particle species [N⁴⁴-96]. The horizontal axis is transverse kinetic energy, and vertical axis is invariant differential yield in arbitrary unit. Not that the normalization among different particle species is also in arbitrary. Invariant cross sections are shown to be exponential in m_t as is seen in proton - proton collisions. However distinct differences are observed in nucleus - nucleus collisions.

- (1) Different inverse slope of m_t exponential for different particle species. Exponential fit is done for each particle species and acquired inverse slopes are shown in Fig. 4. The numbers in the brackets are the fitting error only. Except low m_t regions of pion spectra, inverse slopes are in exponential. And acquired inverse

slopes are different from other particle species. On the other hand, particle and anti-particle, e.g. between positive pion and negative pion, show the similar inverse slopes within the errors.

- (2) Deviation from exponential in low m_t region for pion: In low m_t region (< 0.2 GeV) of positive and negative pion spectra, enhancements are seen from m_t exponential. These phenomena are called *low m_t enhancement*. To see clearly, exponential fit done above 0.2 GeV is extrapolated and shown in dotted lines.

As discussed in section 1.2.3, the former distinct feature is shown to be attribute to a radial expansion of the fireball.

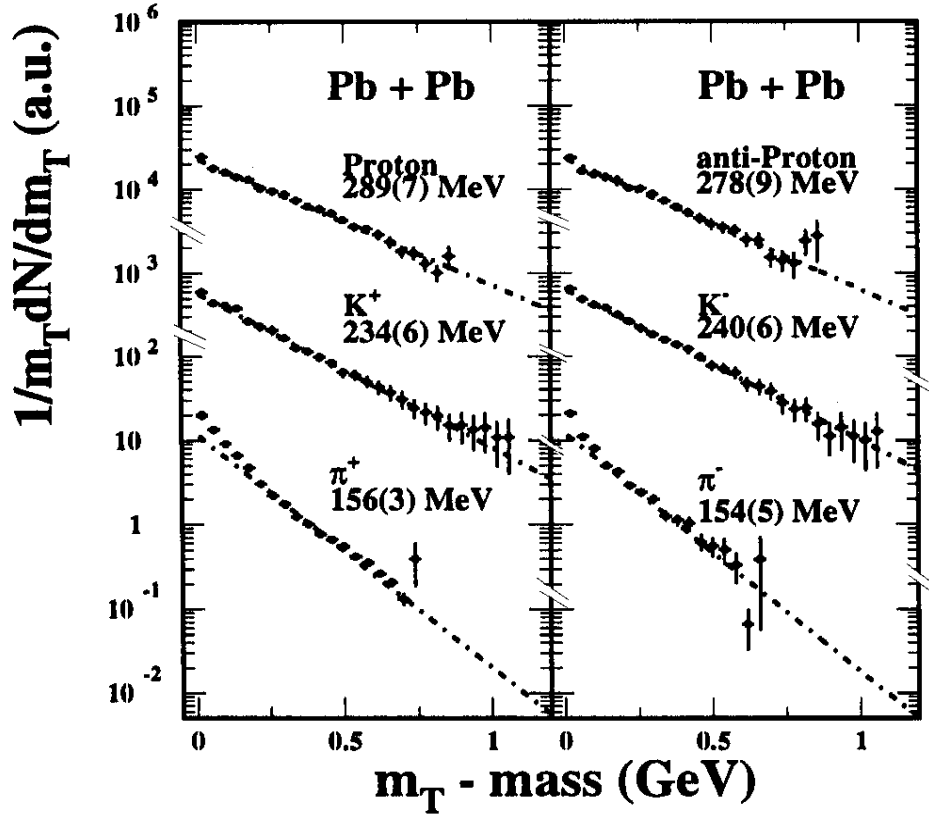


Fig. 4: Invariant differential yield of proton, anti-proton, kaons, pions in central 158 A GeV Pb + Pb collisions. Different slopes (fitted in the region above 0.2 GeV) for different particle species are seen. Also note that the enhancements are seen in low m_t regions for pion spectra [N⁴⁴⁻⁹⁶].

1.2.2 Two-Particle Correlation

Two particle correlations of identified particles have been measured in proton - proton, proton - nucleus, and nucleus - nucleus collisions at several different beam energies. Identical particles are emitted from the fireball of finite size, quantum interference effect should be observed. The interference is used to measure the source size of particle emission, and called as *HBT correlation*, which is originally used for measurements of star size [HT-54]. Two-particle correlation function $C(\mathbf{p}_1, \mathbf{p}_2)$ describes the detection probability of two particles at the momentum of \mathbf{p}_1 and \mathbf{p}_2 . The correlation function is theoretically formalized based on the quantum statistics of bosons (e.g. pions or kaons) or fermions (e.g. protons). Hereafter descriptions for bosons are shown. Assuming the particle emitting source and two detectors as schematically drawn in Fig. 5. For the particle source, two identical bosons are assumed to be emitted from space-time point at \mathbf{x}_1 and \mathbf{x}_2 . For the detection, the two bosons are detected as energy-momentum \mathbf{p}_1 and \mathbf{p}_2 at space-time point at \mathbf{x}_1' and \mathbf{x}_2' .

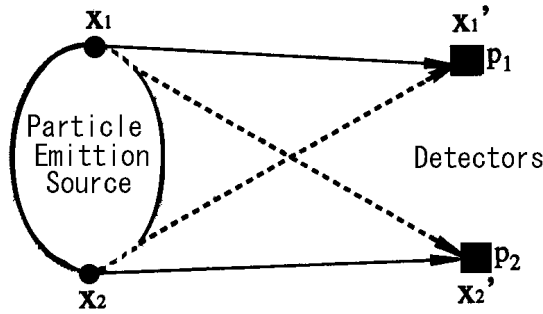


Fig. 5: Schematic drawing for two particle HBT correlation. The identical particle emitted at space-time points \mathbf{x}_1 and \mathbf{x}_2 are detected at \mathbf{x}_1' and \mathbf{x}_2' . Measured energy-momenta are \mathbf{p}_1 and \mathbf{p}_2 , at \mathbf{x}_1' and \mathbf{x}_2' , respectively. Two sets of the arrows (in solid lines or in dashed lines) show possible trajectories of the particles.

The correlation function can be described as follows,

$$C(\mathbf{p}_1, \mathbf{p}_2) = 1 + |\tilde{r}_{eff}(\mathbf{q}, \mathbf{p}_1, \mathbf{p}_2)|^2,$$

where $\tilde{r}_{eff}(\mathbf{q}, \mathbf{p}_1, \mathbf{p}_2)$ is the Fourier transform of effective density, $r_{eff}(\mathbf{x}, \mathbf{p}_1, \mathbf{p}_2)$, $\mathbf{q} = \mathbf{p}_1 - \mathbf{p}_2$, and $\mathbf{x} = \mathbf{x}_1 - \mathbf{x}_2$. When the effective density of particles is

assumed to be the Gaussian distribution,

$$\mathbf{r}_{eff}(\mathbf{x}, \mathbf{p}_1, \mathbf{p}_2) \stackrel{assumed}{=} \frac{N}{4\mathbf{p}^2 R_x R_y R_z \mathbf{s}_t} \times \exp\left[-\frac{x^2}{2R_x^2} - \frac{y^2}{2R_y^2} - \frac{z^2}{2R_z^2} - \frac{t^2}{2\mathbf{s}_t^2}\right],$$

where the normalization constant, N , and the standard deviations R_x , R_y , R_z , and \mathbf{s}_t are valuables as functions of \mathbf{p}_1 and \mathbf{p}_2 . The coordinate is often taken as follows. The incident momentum direction is z-axis, and the center of mass of source is origin of the space coordinate. The x-axis is taken as the direction towards the detector, and for the y-axis is the direction perpendicular to the line joining the source and the detector. The constant, N , is chosen so that the effective density is normalized to 1, by the following way,

$$N = N(\mathbf{p}_1, \mathbf{p}_2) \equiv \int d\mathbf{x} \cdot \mathbf{r}_{eff}(\mathbf{x}, \mathbf{p}_1, \mathbf{p}_2)$$

Therefore the Fourier transform of the effective density is

$$\tilde{\mathbf{r}}_{eff}(\mathbf{q}, \mathbf{p}_1, \mathbf{p}_2) = N \cdot \exp\left[-\frac{R_x^2 q_x^2}{2} - \frac{R_y^2 q_y^2}{2} - \frac{R_z^2 q_z^2}{2} - \frac{\mathbf{s}_t^2 q_t^2}{2}\right].$$

Finally the correlation function for the identical bosons emitted from Gaussian type of source is as follows.

$$C(\mathbf{q}) = 1 + N \cdot \exp\left[-R_x^2 q_x^2 - R_y^2 q_y^2 - R_z^2 q_z^2 - \mathbf{s}_t^2 q_t^2\right]$$

Especially for one dimensional case instead of four dimensions noted by (x, y, z, t), the correlation functions is expressed as a function of q_{inv} as follows.

$$C(\mathbf{q}) = 1 + I \cdot \exp\left[-R_{inv}^2 q_{inv}^2\right]$$

where

$$q_{inv} = \sqrt{q_x^2 + q_y^2 + q_z^2 - q_0^2}.$$

Fig. 6 shows the two-particle correlation function for $R_{inv} = 6$ fm and $I = 1$. The width of the enhanced region around $q_{inv} = 0$ corresponds to the inverse of the source size, $1/R_{inv}$.

As one of the features in nucleus - nucleus collision for HBT measurement

is K_t -dependence of the measured radius, where K_t is average momentum of the particles in pair. This effect is interpreted by the expanding fireball as described in section 1.2.3 .

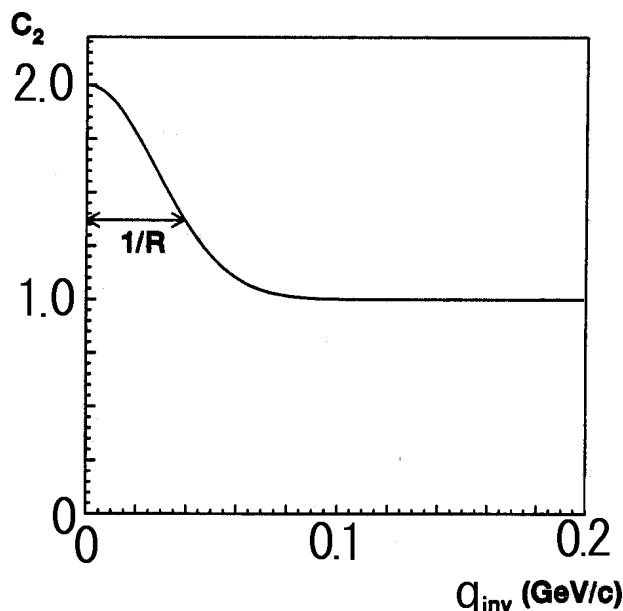


Fig. 6: Two-particle correlation function of a source with $R_{inv} = 6$ fm and $l = 1$ as a function of q_{inv} .

1.2.3 Interpretation with Expanding Fireball Model

To depict the observables in relativistic heavy ion collisions, expanding fireball model is used. This picture is supported by the following two features.

- (1) As mean free paths of the interactions (~ 1.5 fm) are short enough compared with the size of the nucleus (~ 14 fm for lead nucleus). This leads the multiple interactions of emitted particle.
- (2) Average (transverse) kinetic energy (> 100 MeV) of the emitted particles from fireball is much larger than binding energy of nucleus (~ 8 MeV per nucleon). Therefore the fireball cannot keep stationary within a certain volume, but expanding.

When expansion proceeds, the interactions among emitted particles decreases. And when the interaction is ended, the situation is called *freeze out*.

In the heavy ion collisions the slope are different for the different particle species as already shown in Fig. 4. And the collision system dependencies of

slope as a function of particle mass are shown in Fig. 7. Horizontal axis is the particle mass and the vertical axis is the inverse slope parameters in m_T spectra. As low m_T enhancements exist for the pion spectra, only the region above 0.2 GeV in transverse kinetic energy is used for the fitting. For proton - proton collisions the slope is similar for all particle species, while increase of the system size, the difference becomes larger.

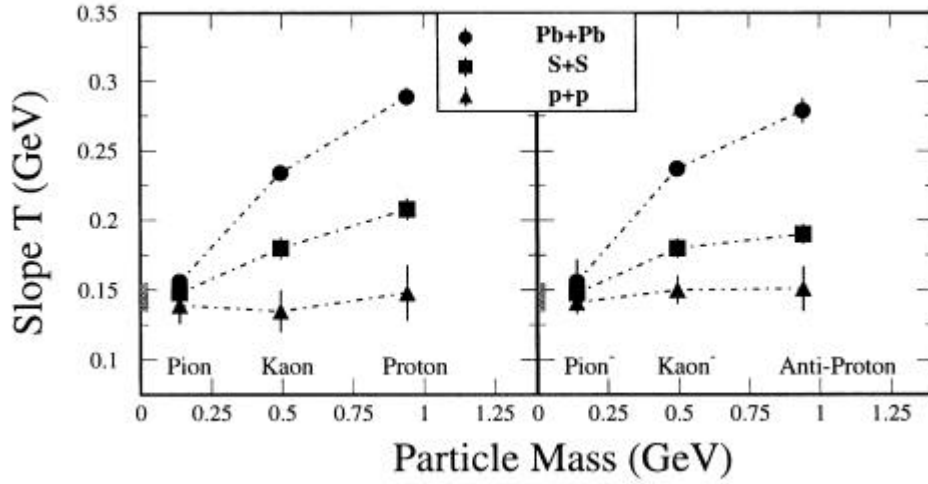


Fig. 7: Observed exponential slope, T , in transverse kinetic energy with respect to the particle mass.

The increase of the inverse slope can be interpreted by assumption the expanding thermal fireball. Namely, phenomenological relation in the following is applicable.

$$T \sim T_0 + m \cdot \langle \mathbf{b} \rangle^2,$$

where m is the particle mass, T_0 corresponds to a temperature at thermal freeze out, and \mathbf{b} corresponds to a collective radial expansion velocity.

In the expanding fireball model, single particle spectra and two particle correlation is studied.

(A) Single Particle Spectra

To evaluate the temperature and the collectivity, single particle (transverse kinetic energy) spectra at mid rapidity in 158 A GeV Pb + Pb central collisions are studied. Fig. 8 shows invariant differential yield of

protons, positive kaons, and positive pions. The horizontal axis is transverse kinetic energy in GeV. The solid line is a parameterization by thermal freeze out temperature, T , and collective (radial) velocity, $\langle b \rangle$, [S^{SX}-98]. The values of parameters are $T = 139$ MeV and $b = 0.42c$, which are common to protons, kaons, and pions. While the low m_{\perp} regions of pion cannot be described, this parameterization tends to follow the differences of the inverse slopes among different particle species.

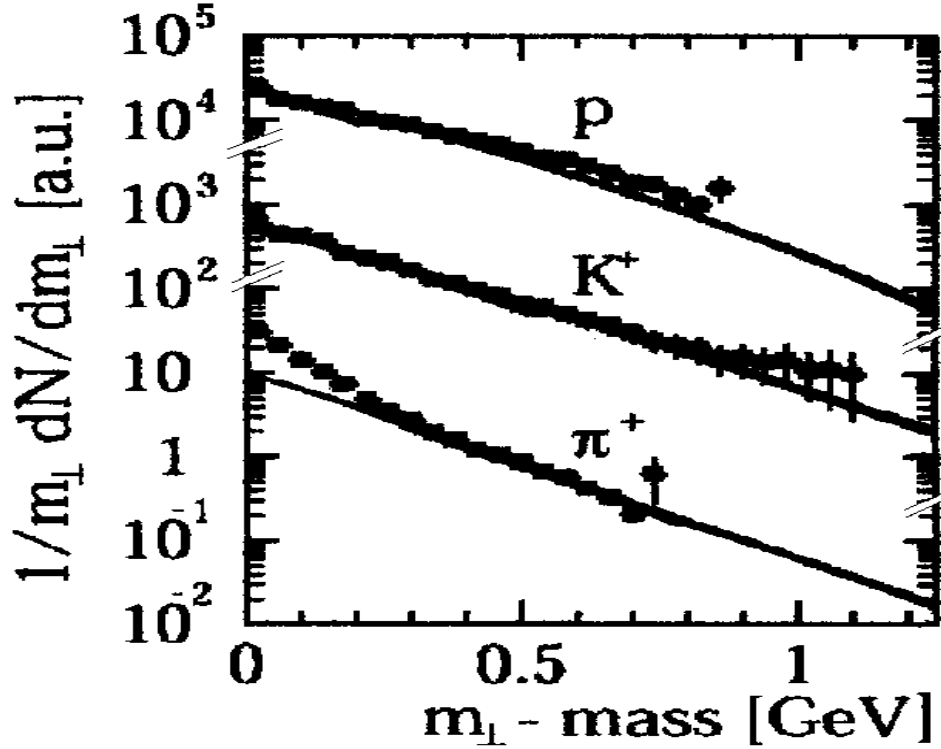


Fig. 8: Single particle spectra parameterized by temperature and collectivity (Temperature, $T = 139$ MeV; Collective velocity (radial) $b = 0.42 c$ [S^{SX}-98]).

(B) Two-Particle Correlation

For the interpretation of the correlation function, emission function, $S(x,K)$, is used. The (Wigner) emission function is the quantum mechanical analogue of the classical phase-space distribution which gives the probability of finding at space-time point x as a source which emits free particles with momentum-energy, K . The correlation function is rewritten with relative momentum, \bar{q} , and mean momentum, \bar{K} , as follows [W⁺-98].

$$C(\bar{\mathbf{q}}, \bar{\mathbf{K}}) \approx 1 + \frac{| \int d^4x S d x, K e^{iq \cdot x} |^2}{| \int d^4x S d s, K |^2},$$

where

$$\bar{\mathbf{q}} \equiv \bar{p}_1 - \bar{p}_2, \text{ and } \bar{\mathbf{K}} \equiv \frac{1}{2}(\bar{p}_1 + \bar{p}_2).$$

By assuming a finite expanding source,

$$S d x, K = \frac{M_T \cosh(\mathbf{h} - Y)}{d^2 \mathbf{p}^3 \sqrt{2 \mathbf{p} d \Delta t}} \times \exp \left[- \frac{K \cdot u d x}{T} \right] \\ \times \exp \left[- \frac{(\mathbf{t} - \mathbf{t}_0)^2}{2 d \Delta t^2} - \frac{r^2}{2 R^2} - \frac{(\mathbf{h} - \mathbf{h}_0)^2}{2 d \Delta \mathbf{h}^2} \right],$$

The first term specifies the shape of the freeze-out hyper surface, the second term is a Lorentz-covariant Boltzmann factor encoding the assumption of local thermal equilibration superimposed by collective expansion. The third factor represent a purely geometrical interpretation. And the values used here are derived as follows.

$$M_T = \sqrt{m^2 + K_T^2}, \quad \mathbf{t} = \sqrt{t^2 - z^2}, \quad Y = \frac{1}{2} \ln \left[\frac{1 + \mathbf{b}_l}{1 - \mathbf{b}_l} \right], \text{ and } \mathbf{h} = \frac{1}{2} \ln \left[\frac{t + z}{t - z} \right].$$

For the expression of thermal equilibrium in Lorentz-covariant way, the following parameterizations are used.

$$K^m = (M_T \cosh Y, K_T, 0, M_T \sinh Y), \text{ and}$$

$$u^m d x = \left(\cosh \mathbf{h}_t d \mathbf{t}, \mathbf{h} \cosh \mathbf{h}_t d r, \frac{x}{r} \sinh \mathbf{h}_t d r, \right. \\ \left. \frac{y}{r} \sinh \mathbf{h}_t d r, \sinh \mathbf{h}_t d \mathbf{t}, \mathbf{h} \cosh \mathbf{h}_t d r \right).$$

By assuming a linear profile of the transverse flow

$$\mathbf{h}_t d r = \mathbf{h}_f \cdot \left[\frac{r}{R} \right],$$

where \mathbf{h}_f is the transverse flow velocity strength, the scalar product in the second term of the emission function is rewritten as follows,

$$K \cdot u d x = M_T \cdot \cosh(\mathbf{h} - Y) \cdot \cosh \mathbf{h}_t d r \\ - K_T \cdot \frac{x}{r} \cdot \sinh \mathbf{h}_t d r$$

From K_T (or M_T) dependence, the strength of the collective flow, h_f , is derived. Fig. 9 shows the M_T dependence of the transverse radius, R_T . For different collective flow strength, h_f , dependences are shown.

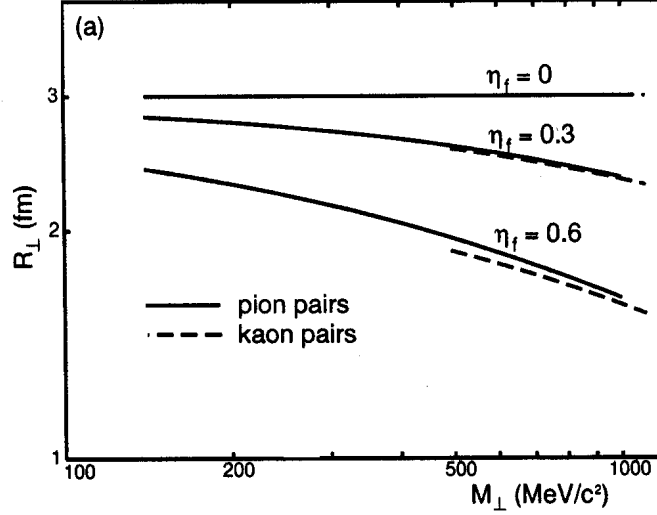


Fig. 9: M_T dependence of transverse radius, R_T , for different strength of the collect flow, h_f (M and R in the figure are M_T and R_T by notations in the text, respectively) [W⁺-98].

Average collective radial velocity, $\langle \mathbf{b} \rangle$, is evaluated as $\langle \mathbf{b} \rangle \sim 5/4 \cdot h_f$ [P^e-97] in the considering region. Fig. 10 shows the relation between the collectivity (h_f) and temperature (T) for the measured negative charged particles. The solid line and the dashed lines correspond to the most probable relation and one sigma deviation, respectively. For the comparison, single particle measurement result for the negative charged hadrons is also shown. One sigma deviation from the χ^2 minimum is shown as the solid line surrounding slant region. The common region for the two particle correlation prefers $T \sim 140$ MeV and $\langle \mathbf{b} \rangle \sim 0.42$. The temperature and the collectivity are well agreed with results evaluated from different particle species in single particle spectra.

One should note that for the extraction of the collectivity and the temperature, low m_t region of the pion spectra is not included. The reason for the enhancements should be studied.

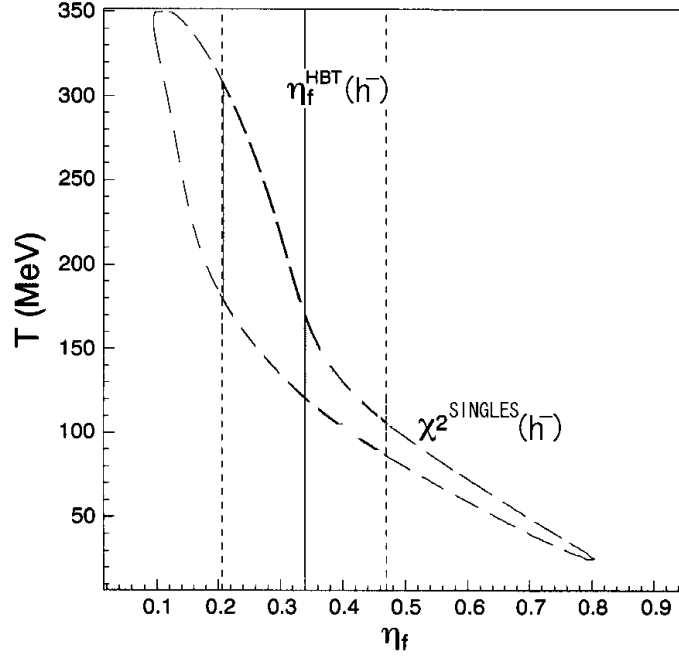


Fig. 10: [Solid line] Two-particle HBT correlation measurement for negative charged particles parameterized by temperature (T) and collectivity (η_f : Transverse flow velocity strength). Note that average collective radial velocity is $\langle b \rangle \sim 5/4 \eta_f$. The dotted lines correspond to one sigma deviations. [Dashed line] For the comparison, single particle measurement result in one sigma deviation from c^2 minimum is shown for the negative charged particles. The common region with two particle correlation prefers $T \sim 140$ MeV and $\langle b \rangle \sim 0.42$ [P e-97].

1.3 Delta Resonance

Collisions of relativistic heavy ions do not simply consist of nucleon - nucleon collisions. To take the difference into account, an idea with excited nuclear is introduced (sect. 1.3.1). As mentioned in section 1.2.1, the failure of thermal model with collective expansion in low m_t region of pion spectra should be addressed in study of heavy ion collisions, and as a possible solution delta resonance is introduced (sect. 1.3.3). First experimental measurement of the delta resonance yield in relativistic heavy ion collisions at 158 A GeV Pb + Pb central collisions is introduced (sect. 1.3.3).

1.3.1 Delta Resonance in Relativistic Heavy Ion Collisions

Relativistic heavy ion collisions does not simply consist of nucleon - nucleon collisions by the following viewpoint. Fig. 11 shows schematic picture for the heavy ion collisions in center of mass frame. Colliding heavy ions are shown by ellipses (T as target, and P as projectile) due to the Lorentz contraction in incident momentum direction (shown in arrows). The constituent nucleons (some of them as examples) are shown in circle inside the ellipses. As explained in sect. 1.1 , the constituent nucleons are mainly colliding with the nucleons in the direction of the incident momentum. In the Fig. 11, the drawn constituent nucleons are mainly colliding with nucleons surrounded by the two dashed lines. One should note that the first pair of nucleons (shown as circles filled in black) are colliding each other, and during collisions with next constituent nucleon (shown as hatched circle) the nucleons are still kept to be in certain excited states for particle formation.

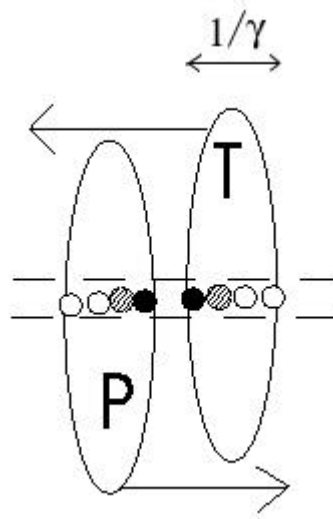


Fig. 11: Schematic picture for the relativistic heavy ion collisions in center of mass frame. The projectile nucleus (P) and target nucleus (T) are Lorentz contracted (in $1/\gamma$) in incident momentum direction (shown in arrows) (see text for detail).

By the following comparison in time scale, importance of excited nucleus, like nucleus including $\Delta(1232)$, can be demonstrated.

- (1) Collision time for each constituent nucleon ($Dt_{col(constituent)}$):

The collision time for each nucleon, $Dt_{col(constituent)}$, is comparable or shorter than particle formation time, $Dt_{form.}$. The collision time in total, Dt_{col} , is < 1 fm/c due to the Lorentz contraction, and the number of constituent nucleons, $N_{(constituent)}$, in incident momentum direction is about 4 for the lead nucleus. Therefore by using following evaluation,

$$Dt_{col(constituent)} \sim Dt_{col} / N_{(constituent)},$$

a typical time for the collision per constituent nucleon, $Dt_{col(constituent)}$, is $1/4$ fm/c.

(2) Typical particle formation time (Dt_{prod}):

Theoretical consideration in QCD give typical time for particle production, Dt_{prod} , is of the order of 1 fm/c [e.g. GR-93].

By comparison of the above two time scale,

$$Dt_{col(constituent)} \ll Dt_{prod}$$

after collision of the first pair of constituent nucleons, the collisions with next coming constituent nucleons is not any more a simple nucleon - nucleon collision. Projectile nucleons in subsequent collision might be in "excited states".

To describe such collisions in the intra nuclear cascade calculation, resonance state of nucleon was introduced as a zero-th order approximation. At the AGS experiments, many theoretical model calculations with such treatment are shown to be successful explaining the experimental data. The $\Delta(1232)$ is the lowest energy level in nuclear resonance with mass of about 1232 MeV/c², width of about 111 MeV, and corresponding lifetime of about 1.8 fm in free space. Isospin and spin of Δ resonance is both 3/2, and there are four charge states (Δ^{++} , Δ^+ , Δ^0 , Δ^-). Based on these arguments, measurements of Δ resonance yield is awaited for the direct confirmation of the model calculation.

1.3.2 Low m_t Enhancement and Delta Resonance

As shown in Fig. 8, expanding fireball picture explains single particle spectra for different particle species and two-particle correlation, with ignoring low m_t enhancement in pion spectra.

As described in the previous section, excited state of nucleon is one of the

major features of nucleus - nucleus collisions. Thus decay product of such resonance have to be taken into account in addition to the thermal with collective expansion for particle production in nucleus - nucleus collisions. The delta resonances contribute in this low m_t region because of the decay kinematics. Delta resonance has a lifetime of 1.8 fm/c (in free space) and decays into pion and nucleon with more than 99% of decay branch as,

$$\Delta \xrightarrow{>99\%} p + N.$$

Due to the large mass difference between pion ($M_p = 0.139 \text{ MeV}/c^2$) and proton ($M_p = 0.938 \text{ MeV}/c^2$), pion carries less momentum. Fig. 12 shows an example of the decay kinematics. The random decay of $\Delta(1232)$'s with (transverse) momentum, p_t , at 0.8 GeV/c, and rapidity, y , at 2.5 are shown. It is clearly shown that momenta of pions are much smaller than those of proton. Thus Δ 's pion contributes dominantly to the low p_t (m_t) region.

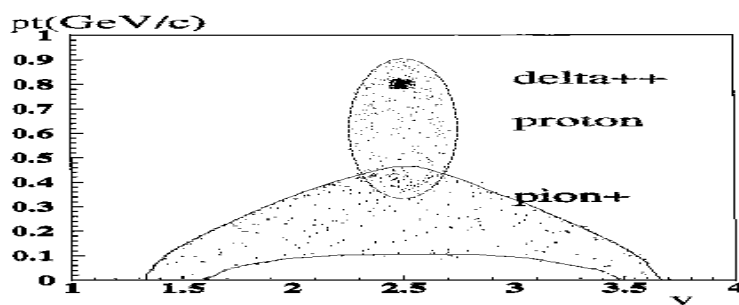


Fig. 12: Example of the decay kinematics of Δ resonance. In this example, Δ 's at $p_t \sim 0.8 \text{ GeV}/c$ and $y \sim 2.5$ (note that Dy is Lorentz invariant) are decayed randomly. Phase space in the transverse momentum, p_t , for daughter pions tends to be lower than that of Δ 's or protons.

For the reason of the low m_t enhancement, other possibilities should be considered, too. An example is Coulomb effects. Due to the highly concentrated charge owing to net protons, positive and negative pions are affected repulsively and attractively, respectively. Such kinds of other effects on low m_t enhancement are discussed in section 5.3.2 .

1.3.3 Delta Resonance Measurement at SPS Energy

Though in relativistic heavy ion collisions at SPS energy the excited states of nucleons should be created and expected to play important roles, experimental measurement of the Δ yield has not yet been carried out before,

which is mainly done due to experimental difficulties described below.

The WA98 collaboration measures the yield of double charged states of delta resonance, namely Δ^{++} . The advantage of the double charged states is that both of decay products, proton and π^+ , are suitable for precise detection by the magnetic spectrometer. Due to the same charge polarity, the systematic error in the detection of the identified particles is reduced (see section 4.1). The yield of the Δ^{++} resonance is measured in the invariant mass of $p\pi^+$ pairs. The difficulty of the measurement, however, is large fraction of combinatorial background. This is partially due to the limited acceptance and dominantly due to the high multiplicity environments in the relativistic heavy ion collisions. The measurements of protons and pions have been done by high resolution of magnetic spectrometer with the high capability of particle identification by time-of-flight method (see sect. 2.2.2). Those detectors are designed for the high multiplicity environments which are unavoidable for relativistic heavy ion collisions.

1.4 Thesis Motivation

This thesis is motivated by the following points, which are introduced in sections from 1.3.1 to 1.3.3 .

- (1) Measurement of particle production of a new particle species; $\Delta(1232)$ in 158 A GeV Pb + Pb central collisions.
- (2) The excited states of nucleons are one of the major characteristics of relativistic nucleus - nucleus collisions. As a prime approximation, lowest states of nucleon, namely $\Delta(1232)$, is meaningful for the consideration of excited states.
- (3) The basic problem to understand both single particle spectra and HBT correlation, low m_t pion enhancement is observed. By using the result of explicit measurement of Δ resonance, the contribution of Δ to the low m_t pion is acquired, and then it is aimed to get the footing of the validity of the expanding fireball model.

The author has contributed to the design of experimental detector (especially, time-of-flight counter (TOF) and optimal alignments of chambers in magnetic spectrometer). He also has devoted in construction and installation of detectors (mainly TOF and streamer tube detectors

(STD)). He has checked performances of TOF after the construction, and readiness of readout electronics (STD). He has programmed operation software (HV control code for TOF and monitoring code for STD). He has operated detector and experiment (especially start counter, TOF, and STD). He has calibrated the detector parameters (TOF, STD) and tuned reconstruction routine (momentum reconstruction). He has produced most of simulation data. And he has studied pion and proton spectrum, and yield of $\Delta(1232)$ resonance.

2.1.1 Ion Source (Electron Cyclotron Resonance: ECR)

In Electron Cyclotron Resonance (ECR) source shown in Fig. 14, which is basically a plasma generator, the lead ions are created by evaporation of from metal surface at a micro oven introduced and injected into plasma chamber.

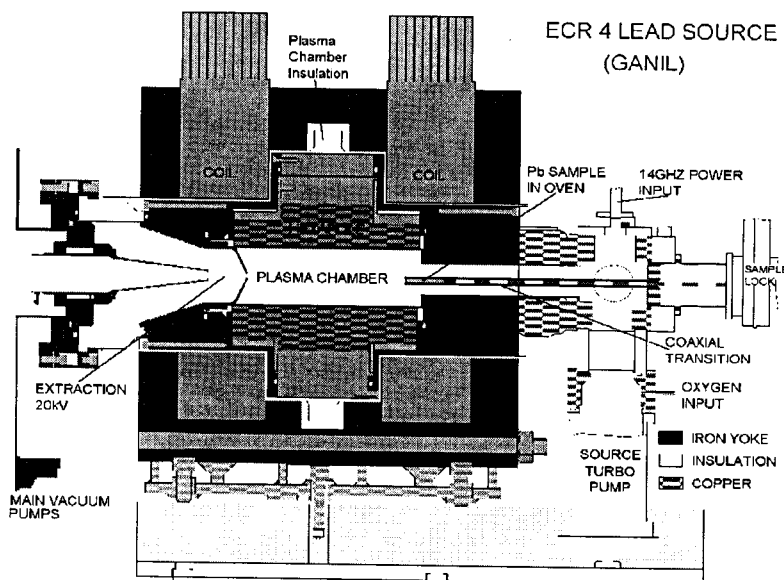


Fig. 14: Electron Cyclotron Resonance (ECR) source.

Plasma is then created by microwave Radio Frequency (RF) ionization at 14.5 GHz. Longitudinal and radial confinement of the plasma is done by a set of two solenoids and by a permanent sextupole magnet. In the acceleration stage, the stripping of the electrons from lead ions is done by passing the projectile through carbon foils.

2.1.2 Linac, Boosters and Synchrotrons (PS and SPS)

Partially stripped $^{208}\text{Pb}^{28+}$ projectiles are injected by the ECR source at the energy of 2.5 keV/nucleon, and accelerated to 4.2 MeV/nucleon by Linear Accelerator 3 (LINAC3). After stripping to $^{208}\text{Pb}^{53+}$, the projectiles are accelerated to 98.5 MeV/nucleon in Proton Synchrotron Booster (PSB), and to 4.25 GeV/nucleon in Proton Synchrotron (PS).

After the second stripping is done to fully stripped $^{208}\text{Pb}^{82+}$, the projectiles are accelerated to 158 GeV/nucleon in Super Proton Synchrotron (SPS). The

fully accelerated 158 A GeV $^{208}\text{Pb}^{82+}$ projectiles are provided to WA98 on H3 beam line at nominal intensity of 10^6 Pb ions per 4.8 seconds of spill.

2.2 WA98 Experiment

On the H3 beam line, the WA98 has following the apparatus, shown in Fig. 15, to measure and to find correlations among several different signals of charged hadrons and of photons.

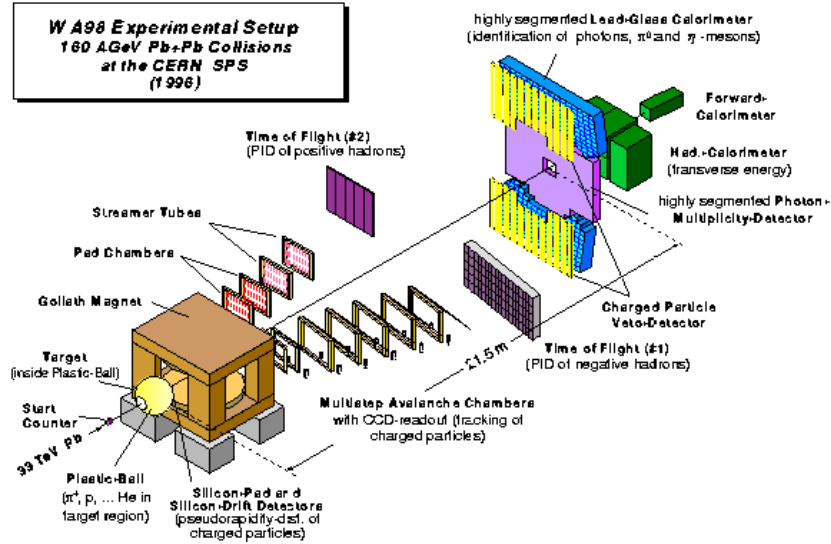


Fig. 15: Experimental setup of WA98 experiment in 1996.

For charged hadrons at mid rapidity, inclusive momentum spectrum, Hanbury-Brown and Twiss (HBT) interferometry, and resonance yield in invariant mass are measured by two arms (*Arm-I* consists of 6 *MSACs* and *RTOF*, and *Arm-II* consists of 2 *PADs*, 2 *STDs* and *JTOF*; the name in *italic in this paragraph* is explained in the following section) of magnetic spectrometers with a dipole magnet. Each spectrometer has particle identification performed by Time-of-Flight (ToF) method (by *JTOF*, $\text{ToF}_{\text{Arm-I}}$, and *Start Counter*).

For event characterizing, several global variables with full azimuthal

coverage are measured. Forward and transverse energy by two calorimeters (*ZDC* and *MIRAC*, respectively), multiplicities of charged and neutral particles at central region (by *PMD* and *SPMD*, respectively), and hadron azimuthal distribution at target region (by *Plastic Ball*) are measured. Energy (or momentum) and emission angles of photons in full azimuth at central region are measured by an electromagnetic calorimeter (*LEDA*).

2.2.1 Target

For target, ^{208}Pb (thickness is 0.210 mm (239 mg/cm²)) is used. Other three kinds of targets (thicker ^{208}Pb (0.436 mm; 495 mg/cm²), ^{93}Nb (0.254 mm; 218 mg/cm²), ^{58}Ni (0.250 mm; 223mg/cm²)) are also used. The summary is in Tab. 1. For the thick and thin lead target, the interaction length is about 1% and 0.5 %, respectively. Minimum bias cross section of each target is shown later in section 3.6 .

<i>Target</i>	<i>Thickness (mm)</i>	<i>Thickness (mg/cm²)</i>
<i>^{208}Pb</i>	<i>0.210</i>	<i>239</i>
<i>^{208}Pb</i>	<i>0.436</i>	<i>495</i>
<i>^{58}Ni</i>	<i>0.250</i>	<i>223</i>
<i>^{93}Nb</i>	<i>0.254</i>	<i>218</i>

Tab. 1: Target used at WA98 experiment.

2.2.2 Magnetic Spectrometer

Charged hadrons at mid rapidity are measured by two arms of magnetic spectrometers with a dipole magnet, including particle identification capability performed by Time-of-Flight (ToF) method,

In this thesis the data taken in the 2nd tracking Arm (Arm-II) (For the historical reason, this is called the second. It is recently installed and operated since 1996 for heavy ion beam) are presented. Arm-II is mainly for positively charged particles, which consists of 2 planes of multi step avalanche chambers with PAD readout system (PADs), 2 planes of Streamer Tube Detectors (STDs) and a Time Of Flight detector (TOF) are implemented. Geometrical acceptances for proton, π^+ and Δ^{++} in the Arm-II are shown in Fig. 16.

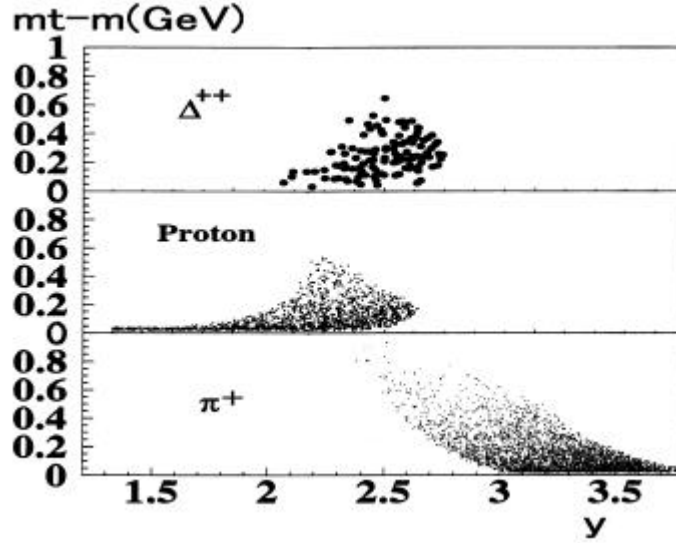


Fig. 16: Geometrical acceptances of proton, p^+ , and D^{++} in Arm-II of WA98 experiment in transverse kinetic energy, $mt-m$, and rapidity, y . Note that the rapidity of center of mass at the SPS energy is 2.9.

On the other side of the beam axis, the 1st tracking Arm (Arm-I), which is mainly for negatively charged particles are placed. Arm-I consists of 6 planes of Multi Step Avalanche Chambers with Camera readout system (MSACs) with another Time Of Flight detector (TOF_{Arm-I}) are installed.

2.2.2.1 Magnet: GOLIATH

Magnetic field is created by a dipole magnet named GOLIATH. During data taking for charge particles, 1.6 Tm of magnetic field was created. The magnetic field is measured with Hall probes at 1.3×10^6 points (in steps of 2 cm along the z-direction, and in steps of 4 cm along the x- and the y-directions).

2.2.2.2 Pad Chamber: PAD

For the tracking, two planes of multi step avalanche chambers with electronic pad-readout system (PAD-1 and PAD-2) [L^{TKG-98}] are placed at $Z_B = 3,850\text{mm}$ and at $Z_B = 4,811\text{mm}$, respectively. Each PAD is 1.2 m (horizontal) \times 1 m (vertical) in size. Each PAD has 35,000 pads which cover about 1 m (horizontal) \times 60 cm (vertical) active area.

Each MSAC has eight stainless-steel mesh planes made of 50 μm diameter

wires in 500 μm pitch, and covered by double mylar windows on both sides. As schematically shown in Fig. 17, position detection of charged particles is performed in following steps.

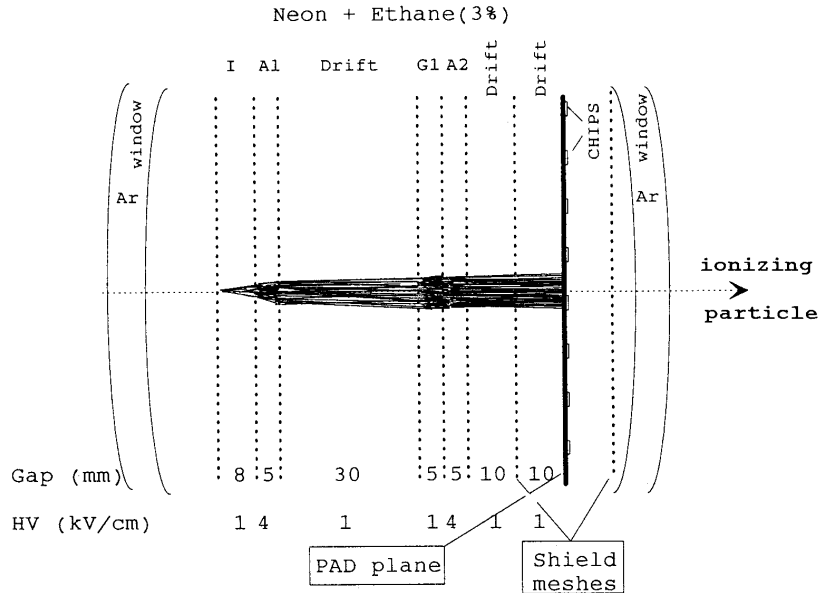


Fig. 17: Schematic drawing of the PAD chamber detector.

A charged particle traversing in the chamber ionizes the filled gas, which is a mixture of Neon and Ethane (3%) in Ionization gap (I). The electrons drifting in the 1st Amplification gap (A1) become an avalanche amplified up to by a factor of 10^3 . In a Gate gap (G), a reversed field of about 100 V/cm prevents electrons drift through. It takes about 700 ns for electrons to reach the gap G. During that time, a gate signal is made by trigger electronics and invokes a pulse of about 200 V with 2 μs length on mesh 4 to change the direction of the field. The electrons are then able to drift to the 2nd Amplification gap (A2), which has slightly less amplification than the gap A1. The last two gaps are for drifting, and mesh 7 and 8 are for protecting and shielding the pad plane from sparks and pickups from the high voltage gating of the chamber.

The electron clouds amplified in the multi step avalanche chambers by a factor about 1.5×10^5 are collected by 1mm (horizontal) \times 17mm (vertical) -size pads as shown in Fig. 18. The most probable charge for a hit is 160 fC, which corresponds to 10^6 electrons. Active area is about 1 m (horizontal) \times 60 cm (vertical) on each PAD chamber.

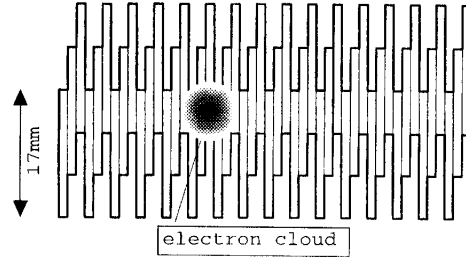


Fig. 18: Schematic illustration of the pad plane.

Readout is done by chips directly mounted on the board. The chip reads 16 pads of induced charge. The chip consists of, from upstream of data transmission, 16 parallel charge integrating amplifier, an analog multiplexer [L^{CGKGT98}], a 4 times amplifier, and a flash 6 bits Analog-to-Digital Converter (ADC). A parity bit is added for consistency check of data transfer to Digital Signal Processor (DSP) located on the bottom of the PADS (called detector DSP in order to distinguish from the other DSPs). Each detector DSP is for a column of 36 ADC chips and suppresses zero data and adds 18 bits of address for non-zero data to identify pad location. The non-zero data on each MSAC chamber are transferred to a DSP (master DSP) located next to VME crate for the WA98 main data acquisition.

2.2.2.3 Steamer Tube Detector: STD

For the tracking, two planes of Iarocci-type Steamer Tube Detectors [Iar-93, B⁺⁻⁷⁹] with electric pad-readout system (STD1 and STD2) are placed at $Z_B = 6,311\text{mm}$ and at $Z_B = 7,811\text{ mm}$, respectively. Capability of being module and low cost performance through automatic production scheme, and easiness of operation, STD becomes popular for larger coverage of position detector. STD is also used as a charge particle veto detector for photon detector on the assumption that it is negligible for high energy photons to be converted into electron-positron pairs. Fig. 19 shows cross section and outer dimensions of STD.

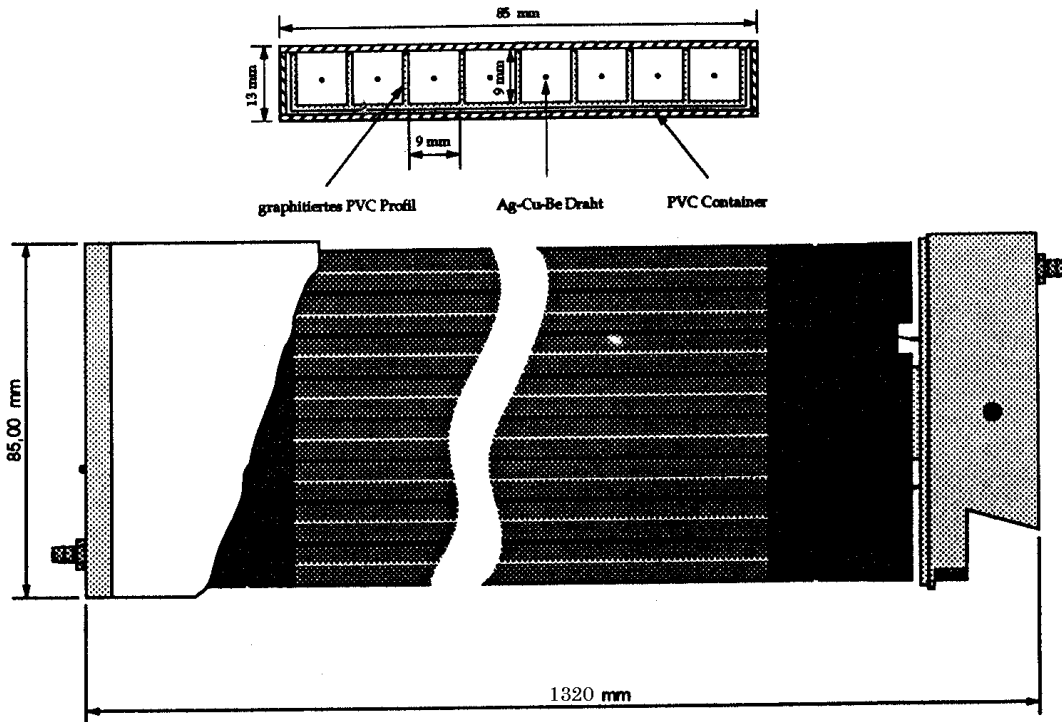


Fig. 19: Cross section view (top) and external dimension (bottom) of STD.

A tube consists of eight horizontally divided rooms made of poly vinyl chloride (PVC). PVC is used for gas tight. Insides of PVC are covered by graphite for electrical ground. Inactive area caused by walls between rooms is 7% of total area. At the center of each room, an $100 \mu\text{m}$ -diameter anode wire is placed. Positive 4.6 kV is applied on the wire during operation. The wires are made of an alloy of copper and beryllium plated with silver. The STD is filled with one atmosphere of mixed gas consisting of 60% carbon dioxide and 30% isobutane as quencher, and of 10% argon as avalanche gas. The read out chips are modified from the original chip used for the charged particle veto detector in the WA98 experiment. Basic architecture is the same as one for the PAD chamber.

2.2.2.4 Start Counter: STR

Start timing for the ToF of the produced particles is measured by Cherenkov light of a lead ion projectile in nitrogen gas (pressure: $p = 1$ [atmosphere], refractive index: $n = 1.0000297$) [T^{su}-96]. In advance of physics run, best radiator is investigated. After injection of 1.5×10^9 lead ions, nitrogen gas has the least deterioration in PMT outputs (9 %), and we

conclude as the gas is the best radiator (see Appendix F).

The timing counter is located 3.4m up stream of the target and has two section of radiator (from upstream, named STR1 and STR2, respectively). Intrinsic time resolution of the timing counter is 30 ps regardless of projectile intensity up to around 3×10^5 projectile ions per second. Using light yield information, events with double or more projectiles coming within 100 ns of window for timing measurement are able to be rejected.

STR1 has 30-mm length of radiator with readout by 1" diameter of photo-multiplier tube (PMT) (Hamamatsu photonics K.K., H5321-MOD). The PMT has quartz window for transparency of Ultra Violet (UV) light, 10 dynodes. On the high voltage divider, booster capacitances at the last three dynodes with additional supplemental High Voltage (HV) power supplies help high rate of detection of beam. The PMT has 0.7 ns of rise time, and 0.16 ns of transit time spread.

STR2 has 45-mm length of radiator with readout by 2" diameter of PMT (Hamamatsu, H2431-02T). The PMT has quartz window for transparency of UV light, 8 dynodes. The booster capacitances at the last three dynodes with additional supplemental HV supplies are also used. The PMT has 0.7 ns of rise time, and 0.37 ns of transit time spread.

At the windows of both PMTs, 30 % transmittance of neutral density filters are installed in order to adjust the amount of photoelectrons.

2.2.2.5 Time of Flight Detector (in Arm -II): JTOF

Stop timing of the ToF of charged particles is measured by the JTOF placed at $Z_B = 14,120$ mm. The JTOF consists of 480 slats, 160 slats in horizontal and 3 slats in vertical, of plastic scintillator (Bicron BC404, characteristics are summarized at Tab. 2).

<i>Physical Constant</i>	<i>Value</i>
<i>Light output (% anthracene)</i>	<i>68</i>
<i>Wavelength of max. emission</i>	<i>408 nm</i>
<i>Decay Constant</i>	<i>1.8 ns</i>
<i>Bulk attenuation length</i>	<i>160 cm</i>
<i>Refractive index (n)</i>	<i>1.58</i>

Tab. 2: Characteristics of BC404 used for JTOF.

The light emitted in the scintillator is collected by two PMTs on the both ends. In order to avoid geometrical conflict among neighboring PMTs, two different lengths of scintillator are used. In each of 160 columns, two of

three slats are 637.7 mm long (named *L*) and the rest one is 433.9 mm long (named *S*). The order in a column is from top, the *S*, the *L*, and then the *L* (the *SLL* configuration) for the most inside column, the *L*, the *L*, and then the *S* (the *LLS* configuration) for the second inside, and the *SLL* configuration comes for the third again. In that way, the *SLL* and the *LLS* configuration come next to next column. After several times of light reflection at the surface of scintillator [T^C-94] and light guide on both edges scintillation light is entered to the PMTs (HAMAMATSU R3478s). Fig. 20 shows the magnified view of the area around the light guide and cathode of the PMT [S^a-95].

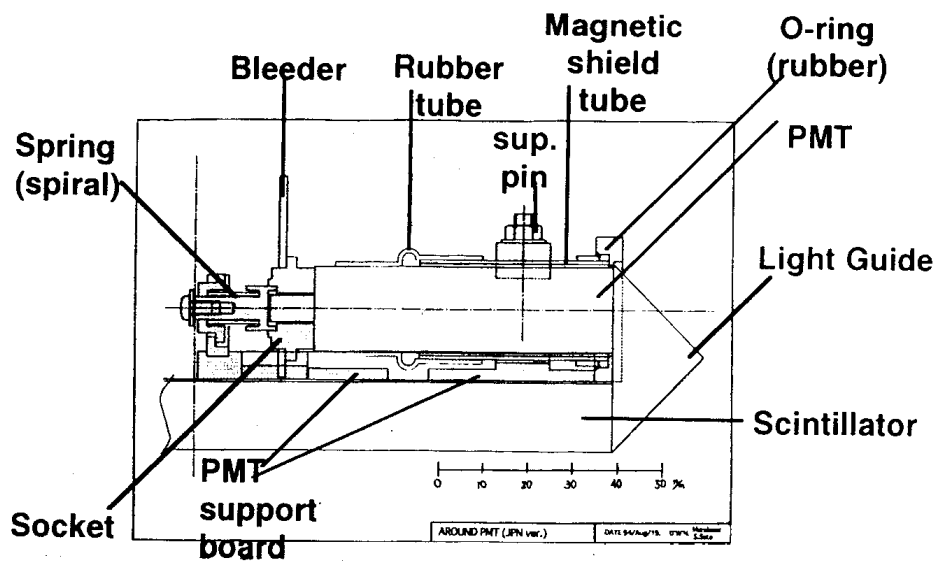


Fig. 20: Schematic drawing around light guide and cathode of PMT.

Typical values for the characters of the PMT are, a factor of 3.9×10^6 for the amplification by 8 dynodes, 14 ns of transit time, 0.36 ns of transit time spread, and 1.3 ns of anode pulse rise time by negative HV at the cathode. Tab. 3 shows the summary of the specification.

Physical Constant	Value
Wavelength of max. response	420nm
Current amplification	$\sim 10^6$
Anode pulse rise time	1.3 ns
Electron transit time	14 ns
Transit time spread (FWHM)	0.36 ns

Tab. 3: Characteristics of R3478s PMT.

With about 2 m of coaxial cable (Fujikura-RG58, 50 ohm impedance), anode of the PTM is connected to custom-made Front End electronics Module (FEM). The input charge is passively split for a Time-to-Voltage Converter (TVC) with a on-board discriminator and for a charge-to-voltage converter followed by a 64-clock-cycles pipeline analog memory unit (AMU) and a 12 bits of analog to digital converter (ADC). The AMU enables delay of AD conversion for about 4.2 micro seconds without external huge amounts of delay coaxial cables. A Front End electronics Module (FEM) covers 16 channels of inputs from PMTs. In the TVC chip, which handles 4 channels, two parallel paths per channel are implemented to subtract cross talk noise inside the chip.

2.2.3 Global Detector

To characterize the event, two hadronic calorimeters are implemented at zero degree (ZDC) and near the mid-rapidity (MIRAC).

2.2.3.1 Mid-Rapidity Calorimeter: MIRAC

For the transverse energy, a calorimeter named MIRAC (Mid-Rapidity Calorimeter; while in 158 A GeV Pb + Pb colliding system, the coverage is more forward in pseudorapidity of $3.5 < \eta < 5.5$) are installed at 24 m downstream from the target. Online event trigger corresponding to selection in impact parameter is possible by hardware-weighted sum of the responses of all towers in MIRAC.

The MIRAC consists of 30 stacks, each divided vertically into six 20 cm \times 20cm towers and segmented longitudinally into electromagnetic and hadronic section. The electromagnetic section is 15.6 radiation lengths deep, and is constructed of alternating layers of lead (3-mm thickness) and scintillating plastic (3mm thickness). The hadronic section is 6.1 absorption lengths deep, and consists of layers of iron (8-mm thickness) and scintillator. The calorimeter has a resolution of 17.9 %/ $(E/\text{GeV})^{1/2}$ for electromagnetic energy and 46.1 %/ $(E/\text{GeV})^{1/2}$ for hadronic energy. A ± 5 cm vertical and ± 20 cm horizontal opening around a beam pipe allow the projectile and projectile spectators to pass through without interacting with MIRAC.

2.2.3.2 Zero Degree Calorimeter: ZDC

The forward energy flux is measured by Zero Degree Calorimeter (ZDC)

located 30 m downstream of the target. The ZDC is constructed of layers of lead and scintillating plastic, and is 105 cm × 75 cm × 202 cm in horizontal, vertical, and longitudinal size, respectively. The ZDC is divided transversely into 35 towers, 7 horizontally and 5 vertically, and each is instrumented with a single PMT.

3. Data Analysis

To reconstruct momentum and to identify particle species, following procedures are done.

- (1) Clustering of hits on each tracking chamber
- (2) Track reconstruction
- (3) Momentum reconstruction
- (4) Track association to TOF
- (5) Particle identification

3.1 Clustering of Hits.

Each pad, sized $1 \times 17 \text{ mm}^2$ for PADs and sized $7 \times 22 \text{ mm}^2$ for STDs, is read out by 6 bits ADC. When ADC value is above a threshold value, it is treated as a fired pad. Adjacent fired pads are treated as a cluster. Fig. 21 shows number of fired pads in PAD1 and PAD2.

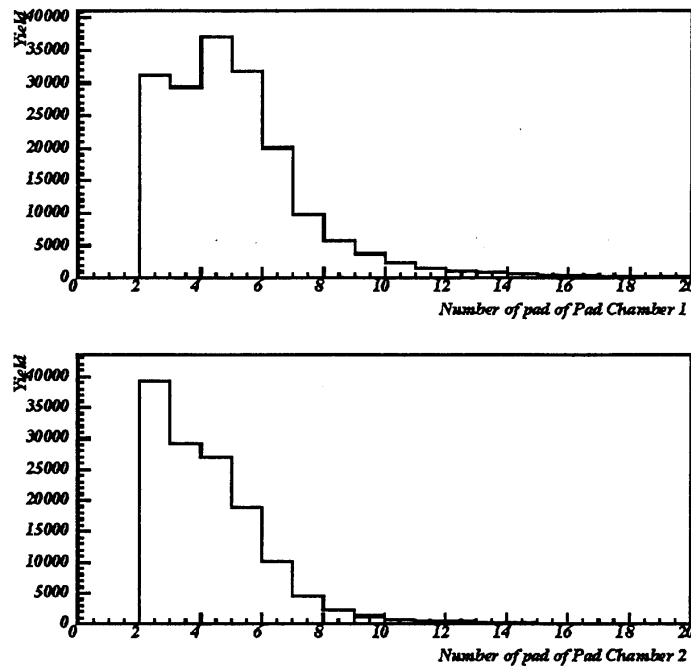


Fig. 21: Number of fired pads in cluster for PAD1 (top) and for PAD2 (bottom).

To reject accidental noise on adjacency pads, when three or more pads are fired in a cluster, the cluster is used for tracking. As shown in Fig. 22, the most probable number of fired pads in a cluster which belongs to

reconstructed track is 5 (a pad has 1mm in width), which is consistent with a 5 mm diameter acquired by simulation and bench test.

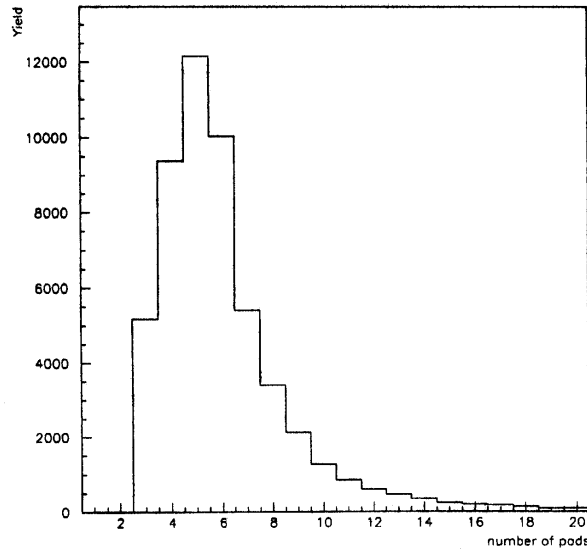


Fig. 22: Number of fired pads in cluster belonging to reconstructed tracks in the tracking system.

Fig. 23 shows number of fired pads in STD1 and STD2. As the pad size of STDs is similar to region affected by ionizing particle traversing in the streamer tube, cluster with 2 or more fired pads are used for tracking.

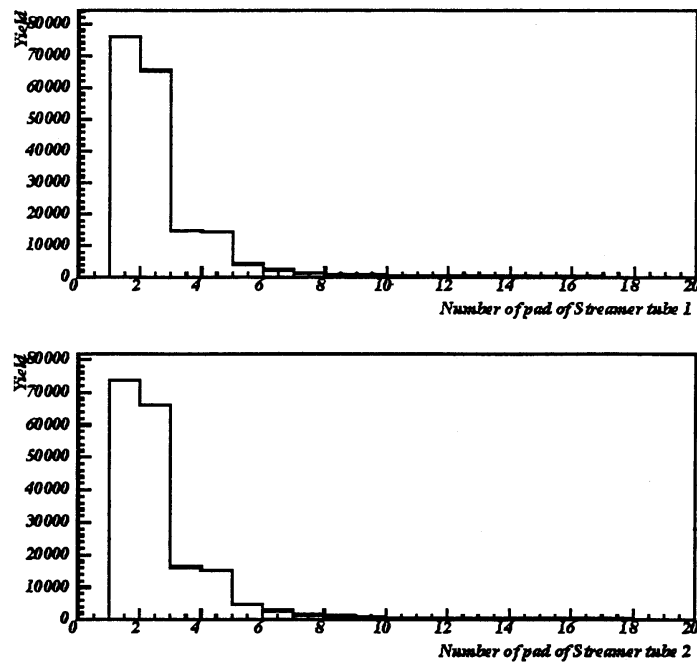


Fig. 23: Number of fired pads in cluster for STD1 (top) and STD2 (bottom).

Position (x for horizontal direction, and y for vertical direction) and their variance (s_x and s_y , respectively) of cluster are defined as follows:

$$\begin{aligned}
 x &= \frac{1}{A} \sum_{i=1}^N x_i \cdot a_i (\equiv \langle x_i \rangle), \\
 y &= \frac{1}{A} \sum_{i=1}^N y_i \cdot a_i (\equiv \langle y_i \rangle), \\
 s_x &= \langle x_i^2 \rangle - \langle x_i \rangle^2 \\
 &= \frac{1}{A} \sum_{i=1}^N x_i^2 \cdot a_i - \left(\frac{1}{A} \sum_{i=1}^N x_i \cdot a_i \right)^2, \\
 s_y &= \langle y_i^2 \rangle - \langle y_i \rangle^2 \\
 &= \frac{1}{A} \sum_{i=1}^N y_i^2 \cdot a_i - \left(\frac{1}{A} \sum_{i=1}^N y_i \cdot a_i \right)^2,
 \end{aligned}$$

where $A = \sum_{i=1}^N a_i$, a_i is the ADC value of pad i , and N is number of pads participating to the considered cluster.

3.2 Track Reconstruction

Track reconstruction is done in 6 steps. From the 1st step to the 5th step, track candidates are listed in the following steps from (1a) to (1e). In the 6th step, among the track candidates, track is selected by the tracking quality as shown in the following step (2). In this section, PAD-1, PAD-2, STD-1, STD-2, and JTOF are called chamber 1, 2, 3, 4 and 5, respectively.

(1st step) For all combination of clusters from 2 in 4 chambers (chamber i , and chamber j) which is not positioned next to each other, make straight line, l_{ij} . The relation between i and j is

$$j = i + 2 \text{ (where } i = 1, 2),$$

which yield the combination of $(i, j) = (1, 3), (1, 4), \text{ and } (2, 4)$.

(2nd step) On different chamber (chamber k) from the 2 used chambers, find clusters around a crossing point with line l_{ij} .

(3rd step) If a cluster is found on the chamber k , deviations between the

cluster and the crossing point (\mathbf{dx}_k and, \mathbf{dy}_k for horizontal and vertical direction, respectively) are calculated as.

$$\mathbf{dx}_k = x_k - x_{ij \rightarrow k},$$

$$\mathbf{dy}_k = y_k - y_{ij \rightarrow k},$$

where x_k and y_k the cluster position on the chamber, and where $x_{ij \rightarrow k}$, $y_{ij \rightarrow k}$ are the position of crossing point. If both 2 deviations, \mathbf{dx}_k and \mathbf{dy}_k are smaller than $7R_{xk}$ and $7R_{yk}$, where R_{xk} and R_{yk} is expected deviation from position resolution of the chamber k .

$$\mathbf{dx}_k < 7R_{xk}$$

$$\mathbf{dy}_k < 7R_{yk}$$

Tab. 4 summarizes difference of cluster position expected from the position resolution of the tracking chambers and of JTOF.

Chamber	k	R_{xk} (mm)	R_{yk} (mm)
PAD-1	1	1.28	2.10
PAD-2	2	1.26	2.25
STD-1	3	2.61	6.95
STD-2	4	4.66	7.71
JTOF	5	20.0	50.0

Tab. 4: Deviation of cluster position expected from position resolution for the chambers and TOF in ARM -II.

(4th step) Target image in y (which is not effected by magnetic field) is also required to be less than 108 mm.

(5th step) The minimum number of clusters used for tracking is 3.

For tracks satisfy the above criteria are called *track candidates*.

(6th step) For the track candidates, (i) χ^2 values for tracking are calculated, and (ii) momentum and (iii) flight path length are reconstructed. The candidates are sorted in ascendant order for the χ^2 value. Track candidates sharing the same cluster with other candidates with smaller χ^2 are rejected.

3.3 Momentum Reconstruction and Flight Path Length Calculation

For the momentum reconstruction, 3 steps are performed. In the 1st and the 2nd steps, general formula based on the relation between a momentum kick and a charged particle in a magnetic field is applied. Then in the 3rd step, especially for the negative p_x particles (namely, once going toward ARM-I at the target, and then bending to ARM-II in the magnetic field), a Monte Carlo simulation is used to eliminate dependences of the reconstructed momentum on the polar and the azimuthal angles of the particle trajectory. Flight path length is also reconstructed in the step 1a.

(1st step) Momentum kick ($\Delta\vec{p}$ [GeV/c]) to a charged particle (charge q [e]) in a magnetic field (\vec{B} [T]) is generally given as follows:

$$\Delta\vec{p} = 0.29979 \cdot q \int_{A1 \rightarrow A2} \vec{B} \times d\vec{s},$$

where $\int_{A1 \rightarrow A2}$ denotes an integration along the particle trajectory beginning at a point $A1$ and ended at a point $A2$, $d\vec{s}$ denotes differential of the trajectory. As in the WA98 experiment the magnetic field is generated in vertical direction (parallel to the Y_B -axis (see WA98 coordinate system in Appendix D)) and the ARM-II spectrometer is well segmented perpendicular to the Y_B -axis, momentum is reconstructed on the horizontal plane (X_B - Z_B plane) as shown in Fig. 24.

Also flight path length is reconstructed as a sum of following three lengths, distance between target and A1, length of bending path (ϕ), and distance between A2 and JTOF.

where Δp_x denotes x-component of the momentum kick $\Delta \vec{p}$, and $\Delta \mathbf{q}$ is the bending angle of the trajectory on the X_B - Z_B plane.

To calculate Δp_x , a straight line is extrapolated from the reconstructed track with an assumption that the particle is coming from the target. In the magnetic field, the measured field values are referred at equally-divided 20 points ($s(1) \sim s(20)$) along the trajectory. Therefore Δp_x is calculated as following:

$$\Delta p_x = 0.29979 \cdot \sum_{i=s(1)}^{i=s(20)} (By_i \cdot \Delta z_i - Bz_i \cdot \Delta y_i),$$

where By_i , Bz_i , Δy_i and Δz_i are the value at the points $s(1) \sim s(20)$ for By (y-component of magnetic field), Bz (z-component of magnetic field), Δy (position kick in Y_B direction) and Δz (position kick in Z_B direction), respectively. $\Delta \mathbf{q}$ is acquired from a geometrical calculation (see Fig. 24):

$$\Delta \mathbf{q} = \mathbf{b} - \sin \left(\frac{R_0}{z_0} \sin \alpha \right) \mathbf{a},$$

where α is an angle of A2 with respect to center O (O: the center of magnetic field, A2: an exit point of the trajectory from magnetic field), α is an angle of the trajectory measured by the second arm, R_0 is the first order of radius of magnetic field, and Z_0 is the distance between the target and the magnet.

(3rd step) To eliminate dependence of reconstructed momentum on the polar and the azimuthal angle especially for the negative p_x particles, best parameters are searched based on the following formula.

$$\begin{pmatrix} p \\ \sin \mathbf{q} \cdot \cos \mathbf{f} \\ \sin \mathbf{q} \cdot \sin \mathbf{f} \end{pmatrix} = \begin{pmatrix} M_{11} & M_{12} \\ M_{21} & M_{22} \\ M_{31} & M_{32} \end{pmatrix} \cdot \begin{pmatrix} \sin \mathbf{q} \cdot \cos \mathbf{f} \\ \sin \mathbf{q} \cdot \sin \mathbf{f} \end{pmatrix},$$

Where M_{ij} ($i=1,2,3; j=1,2$) is free parameters for lease dependence.

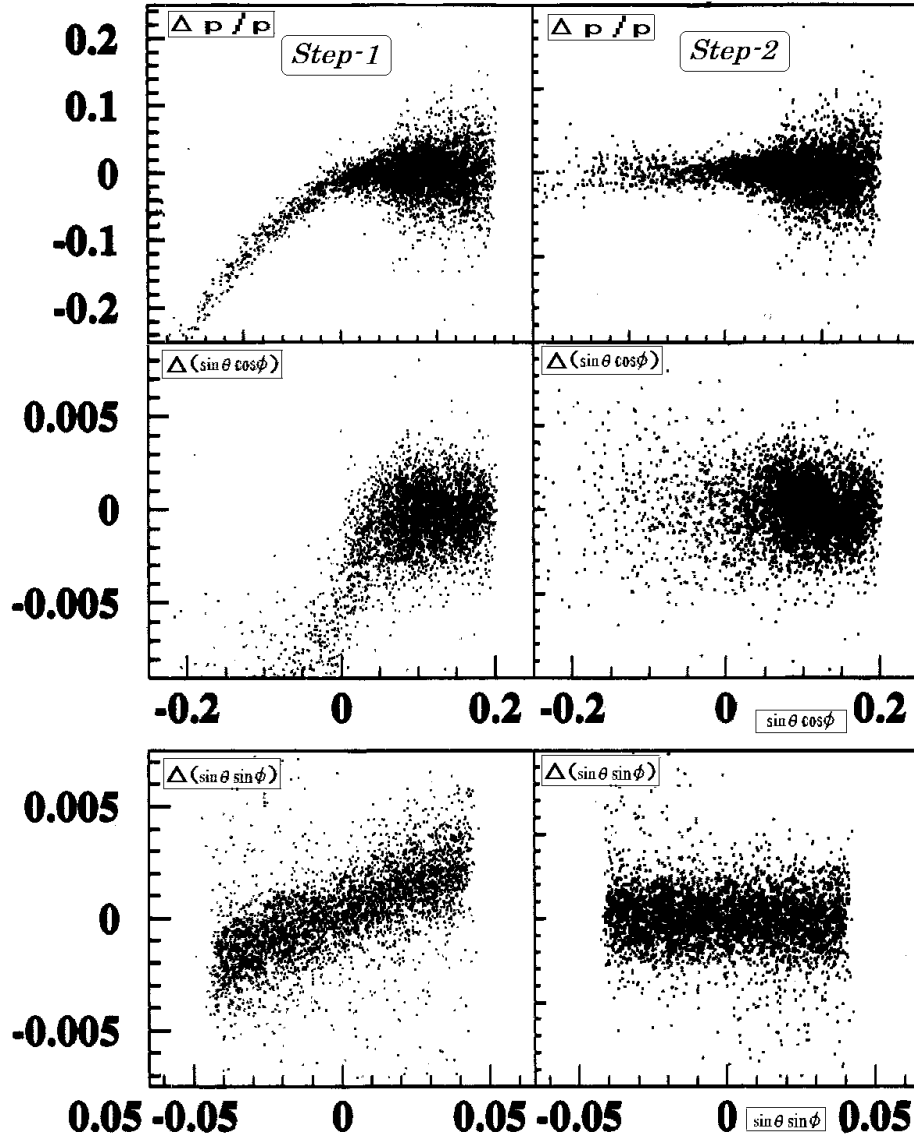


Fig. 25: Elimination of angle dependence for momentum reconstruction. (left) before correction, (right) after correction.

Fig. 25 shows the results of the correction, where the left and the right figure correspond to before and after the second step of the correction. Note that negative p_x particles are plotted in the negative region of $\sin \theta \cos \phi$ for the two top pictures (because $p_x = p \sin \theta \cos \phi$).

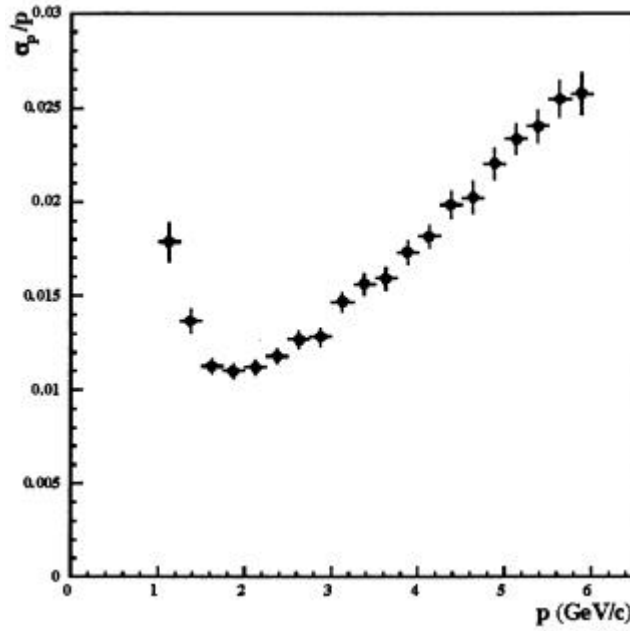


Fig. 26: momentum resolution of Arm -II.

Fig. 26 shows the momentum resolution of the ARM-II. Polynomial fitting (up to second order) of the momentum resolution results in the following equation.

$$\frac{\mathbf{S}_p}{|\vec{p}|} \cong 1.03 - 0.08p + 0.06p^2 [\%],$$

where p is momentum in GeV/c. The typical values of $\frac{\mathbf{S}_p}{|\vec{p}|}$ are $\sim 1\%$ at $|\vec{p}|$

$= 2$ GeV/c and $\sim 2\%$ at $|\vec{p}| = 5$ GeV/c. Degradation of resolution toward lower momentum than about 1.8 GeV/c is mainly because of multiple scatterings in the spectrometer. And degradation toward higher momentum than about 1.8 GeV/c is mainly due to position resolution of the tracking chambers.

3.4 Time of Flight Calibration

Timing chart of the timing measurement and the energy deposit measurement at the JTOF is schematically shown in Fig. 27.

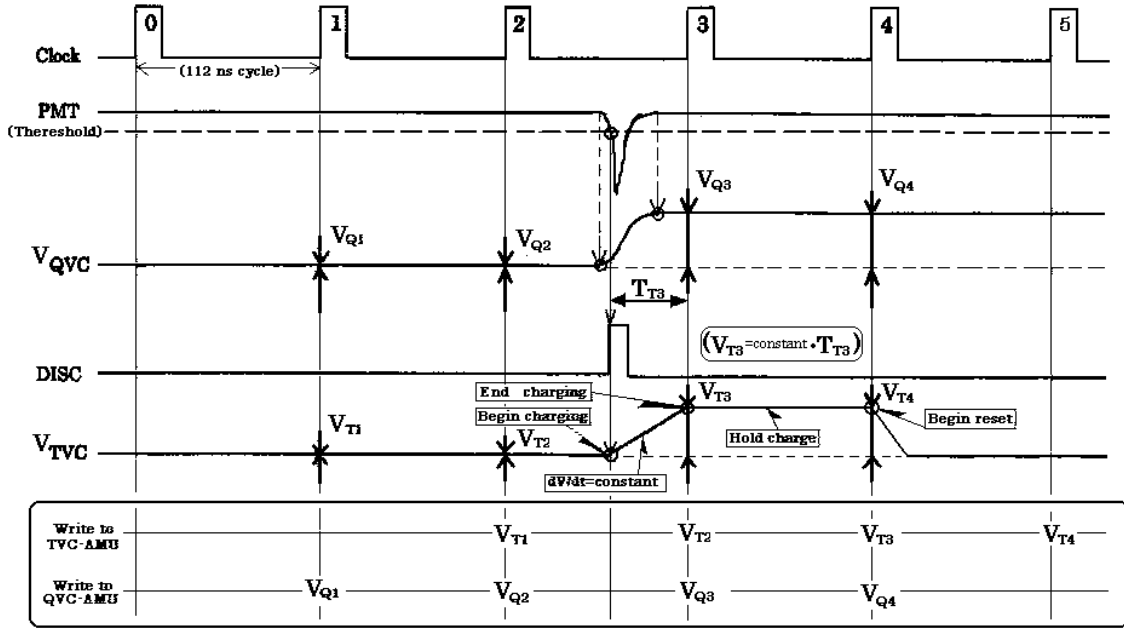


Fig. 27: timing diagram for the JTOF readout. The timing is measured as V_{T3} and the energy deposit is measured as $V_{Q3} - V_{Q1}$.

Time of flight (TOF) of the charged particle is defined as a difference in two measured timings. The one is measured by the JTOF ($timing_{JTOF}$), and the other is measured by the start counter ($timing_{Start}$);

$$TOF = timing_{JTOF} - timing_{Start}.$$

The time calibrations are done in the following 4 steps.

(1st step) To eliminate hardware channel dependence of conversion parameter from the TVC value [channel] to time [ps], the timing at the start counter and the JTOF are defined by the weighted timing $T_{JTOF}(J)$ (J denotes the slat of the JTOF) and T_{Start} for the JTOF and the start counter, respectively.

$$T_{JTOF}(J) \equiv \frac{1}{2} \left(k_{J1} \cdot TVC_{J1} + k_{J2} \cdot TVC_{J2} \right),$$

$$T_{Start} \equiv \frac{1}{2} \left(k_{S1} \cdot TVC_{S1} + k_{S2} \cdot TVC_{S2} \right),$$

These conversion parameters (k_i) are acquired at bench test using a quartz clock generator, where i denotes the FEE channel ($J1$ and $J2$ for the JTOF, and $S1$ and $S2$ for the start counter). Therefore the time of flight calibrated in this step ($TOF_1(J)$) is following.

$$TOF_1(J) \equiv T_{JTOF}(J) - T_{Start},$$

(2nd step) To eliminate cable length dependence for each slat, a time offset for each JTOF slat ($T_0^{1st}(J)$) is derived by the following definition:

$$T_0^{1st}(J) \equiv \langle TOF_{\mathbf{p}}(J) \rangle,$$

$$TOF_{\mathbf{p}}(J) \equiv TOF_1(J) - TOF_{\mathbf{p}}(p, L), \text{ and}$$

$$TOF_{\mathbf{p}}(p, L) \equiv \frac{L}{c \cdot \left(\frac{p}{\sqrt{m_{\mathbf{p}}^2 + p^2}} \right)},$$

where L and p is the evaluated flight path length and the reconstructed momentum via track reconstruction routine. Therefore the time of flight calibrated in this step ($TOF_2(J)$) is following.

$$TOF_2(J) = TOF_1(J) - T_0^{1st}(J).$$

(3rd step) To eliminate time walk effect through variation in pulse height (equivalent to QVC value here), a time offset parameters for each JTOF FEE channel ($T_Q(J1), T_Q(J2)$) are derived by the following definition.

$$T_Q(J1) \equiv \langle \sqrt{QVC(J1)} \cdot TOF_2(J) \rangle,$$

$$T_Q(J2) \equiv \langle \sqrt{QVC(J2)} \cdot TOF_2(J) \rangle.$$

Therefore the time of flight calibrated in this step ($TOF_3(J)$) is following.

$$TOF_3(J) \equiv TOF_2(J) - \frac{T_Q(J1)}{\sqrt{QVC(J1)}} - \frac{T_Q(J2)}{\sqrt{QVC(J2)}}.$$

(4th step) To eliminate time dependence of the time conversion factor, the cable length and other factors, more time offsets ($T_0^{2nd}(run)$ for run dependence, $T_0^{2nd}(slat)$ for slat dependence, and $T_0^{2nd}(FEE \text{ range})$ for dynamic range dependence of FEE) are derived in the same way in step 2.

$$T_0^{2nd}(parameter_i) \equiv \langle TOF_{\mathbf{p}}(parameter_i) \rangle,$$

$$TOF_{\mathbf{p}}(parameter_i) \equiv TOF(parameter_i) - TOF_{\mathbf{p}}(p, L),$$

where parameter_i are run, slat, and FEE range.

This step is repeated for certain periods shown in Tab. 5 for each parameter. And every step (step k to step (k+1)), the time of flight is calibrated in following way.

$$TOF_{k+1} = TOF_k - T_0^{2nd}(\text{parameter}_i).$$

<i>Parameter</i>	<i>Number(No.) of parameters</i>	<i>Cycle of calibration</i>
<i>K</i>	<i>No. of FEE channel (960 for JTOF + 2 for Start)</i>	<i>Constant</i>
<i>T₀^{1st}</i>	<i>No. of JTOF slat (480)</i>	<i>Constant</i>
<i>T_Q</i>	<i>No. of JTOF FEE channel (960)</i>	<i>Every 50 runs</i>
<i>T₀^{2nd(run)}</i>	<i>1</i>	<i>Every run</i>
<i>T₀^{2nd(slat)}</i>	<i>No. of JTOF slat (480)</i>	<i>Every 50 runs</i>
<i>T₀^{2nd} (FEE range)</i>	<i>(No. of JTOF slat + 2 for start) × 5 ranges (480 for JTOF + 2 for Start) × 5</i>	<i>Every 50 runs</i>

Tab. 5: Time calibration parameters for JTOF and for start counter.

The y-position (height) at JTOF (Y_{JTOF}) is calculated by the time difference between PMT located at the top and the bottom side of scintillators.

$$Y_{JTOF}(J) = \frac{v(J)}{2} \cdot (TVC(J1) - TVC(J2)) + Y_{JTOF,0}(J),$$

where $v(J)$ is the propagation velocity [mm/channel] of light in the scintillator, , and $Y_{JTOF,0}(J)$ is a y-position offset [mm]. The horizontal position at JTOF (X_{JTOF}) is a position where difference between an extrapolated position from the tracking and a center of the scintillator is minimal. Tab. 6 shows the position calibration parameters for JTOF.

<i>Parameter</i>	<i>Number(No.) of parameters</i>	<i>Cycle of calibration</i>
<i>V</i>	<i>No. of JTOF slat(480)</i>	<i>Every 50 runs</i>
<i>Y_{JTOF,0}</i>	<i>No. of JTOF slat(480)</i>	<i>Every 50 runs</i>

Tab. 6: Position calibration parameters for JTOF.

Resolution of time of flight between the start counter and the JTOF is 85 pico seconds as shown in Fig. 28. And residuals for the hit position at JTOF are 12.5 mm and 26.4 mm for the horizontal and vertical direction, respectively.

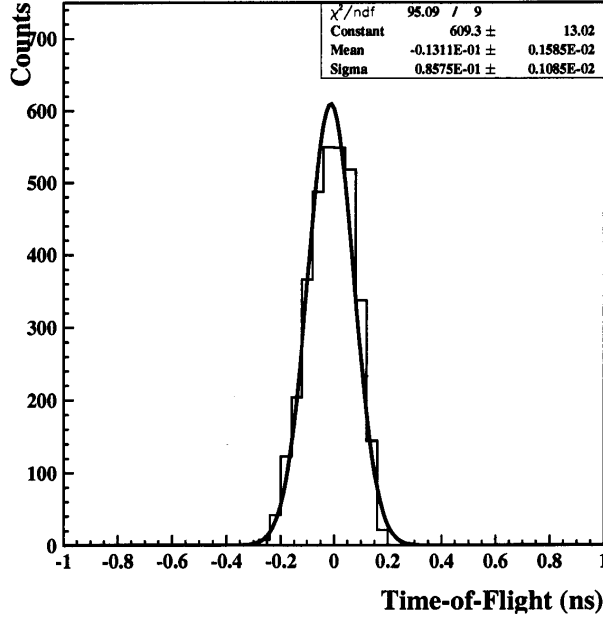


Fig. 28: Time of flight resolution between the start counter and the JTOF.

3.5 Particle Identification

Mass of the particle (m [GeV/ c^2]) is reconstructed using the following formula driven by the Lorentz transformation.

$$p = m\mathbf{b}\mathbf{g} ,$$

where

$$\mathbf{b} = \frac{L}{TOF \cdot c} ,$$

$$\mathbf{g} = \frac{1}{\sqrt{1 - \mathbf{b}^2}} .$$

And p [GeV/ c] is momentum of the particle, TOF [sec] is the time of flight, L [m] is the flight path length, and c [m/sec] is the velocity of the light. From those equations the TOF can be rewritten as a function of the path length and the momentum $f_1(L, p)$, or (square of) particle mass can be rewritten as a function of the path length, the momentum, and time of flight $f_2(L, p, TOF)$.

$$\begin{aligned}
TOF &= f_1(L, p) \\
&= \left[\frac{L}{c} \right] \cdot \sqrt{\frac{m^2 + p^2}{p^2}},
\end{aligned}$$

or

$$\begin{aligned}
m^2 &= f_2(L, p, TOF) \\
&= p^2 \left[\frac{TOF \cdot c}{L} \right]^2 - 1.
\end{aligned}$$

When we define expected time of flight (TOF) for the pion (mass is m^2) as

$$TOF_p \equiv \left[\frac{L_{measured}}{c} \right] \cdot \sqrt{\frac{m_p^2 + p_{reconstructed}^2}{p_{reconstructed}^2}},$$

,where $L_{measured}$ is measured flight path length and $p_{reconstructed}$ is the reconstructed momentum. And we take difference between the measured time of flight ($TOF_{measured}$), the clear separation among particle species is seen in Fig. 29.

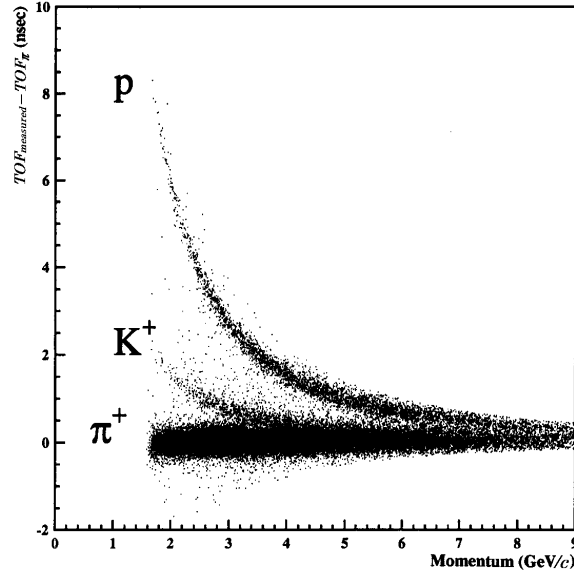


Fig. 29: Relation between $TOF_{measured} - TOF_{\pi}$ and momentum.

Then we derive particle mass ($m_{reconstructed}$) as follows,

$$m_{reconstructed}^2 = p_{reconstructed}^2 \left(\frac{TOF_{measured} \cdot c}{L_{measured}} \right)^2 - 1$$

Fig. 30 shows mass square distribution of positive particle with momentum lower than 3.5 GeV/c measured in the Arm-II.

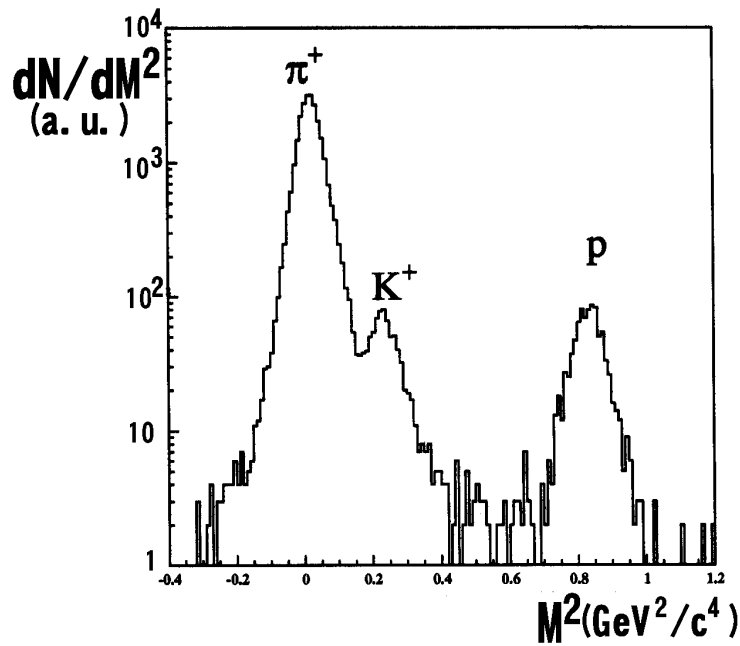


Fig. 30: Mass square (GeV^2/c^4) distribution of positive particle with momentum lower than 3.5 GeV/c measured in the Arm -II.

And the resolutions of mass square are shown in Fig. 31 for π^+ and proton.

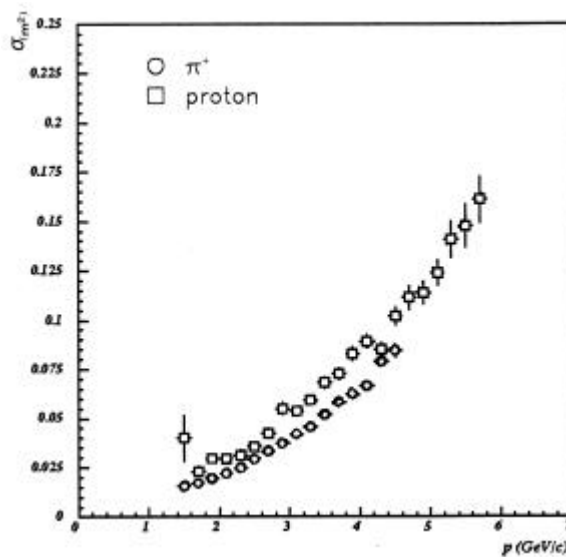


Fig. 31: Mass square resolution for the positive pion and proton.

3.6 Event Selection

To choose central collision events, transverse energy measured by the hadronic calorimeter MIRAC, E_T , is used. For hardware scheme of MIRAC, see section 2.2.3.1 . The top 10 % of minimum bias events in the order of the E_T are used in this analysis. The minimum bias events, MB , are defined by the following coincidence logic made by four detectors.

$$MB \equiv \overline{Halo} \cap \overline{STR} \cap \overline{Veto} \cap MIRAC^{(low)}$$

Here, $Halo$, STR , $Veto$, and $MIRAC^{(low)}$ represent detection by a halo detector, the start counter (see 2.2.2.4), a veto detector, and the MIRAC calorimeter, respectively. And bars above $Halo$ and $Veto$ represent anti-coincidence. The inner halo counter is a scintillation counter with a hole in its center, which is located about 5.7 m upstream of the target in order to detect interaction in upstream. The veto detector is a scintillation counter located about 50 cm down stream of the start counter in order to detect off-axis beam. For $MIRAC^{(low)}$, threshold is set as low as possible to distinguish from noise.

The minimum bias cross section, s_{INT} [mb], is defined as follows.

$$s_{INT} \equiv \frac{N_{INT} \cdot 10^{27}}{N_{beam} \cdot r \cdot t}$$

Here, N_{INT} and N_{beam} are the numbers of interaction and beam, respectively, r [cm⁻³] is the numbers of nuclei per unit volume, and t [cm] is the target thickness. To correct target-out background, N_{INT} should be replaced with N_{INT}^{cor} calculated as follows.

$$N_{INT}^{cor} = N_{INT} - N_{INT(emp)} \cdot \frac{N_{beam}}{N_{beam(emp)}}$$

where $N_{INT(emp)}$ and $N_{beam(emp)}$ are the numbers obtained for the empty target runs. Tab. 7 shows the minimum bias cross section of the different target used in WA98 experiment. The *r.m.s.* in the table denotes the root mean square of run-by-run fluctuation.

Target	Thickness (mm)	Thickness (mg/cm ²)	Minimum Bias Cross Section (mb)	Minimum Bias Cross Section (Magnet on) (mb)
²⁰⁸ Pb	0.210	239	6202 ± 1 (r.m.s.=58)	6451 ± 0.1 (r.m.s. =53)
²⁰⁸ Pb	0.436	495	-	-
⁵⁸ Ni	0.250	223	3599 ± 5 (r.m.s.=17)	3704 ± 3 (r.m.s. =20)
⁹³ Nb	0.254	218	4332i ± 12 (r.m.s.=24)	4496 ± 2 (r.m.s. =11)

Tab. 7: Minimum bias cross sections of for different targets used at WA98 experiment.

3.7 Invariant Mass Spectra

To measure Δ resonance abundance, invariant mass spectra analysis is proceeded for proton- π^+ pairs. The accidental combinatorial background in spectra is evaluated by mixed event technique.

(a) Invariant Mass of Real Event

The yield of Δ resonance is evaluated in invariant mass of real events. For all the pairs of identified as proton and positive pion, invariant mass, m_{inv} , is calculated by the following definition.

$$m_{inv} = \sqrt{|E_{\mathbf{p}} + E_p|^2 - |\vec{p}_{\mathbf{p}} + \vec{p}_p|^2}.$$

Fig. 32 shows the invariant mass distribution for the real events. The pairs consist of two components. One is the pairs decayed form the same Δ^+ decay and the other is pairs essentially uncorrelated combinatorial background.

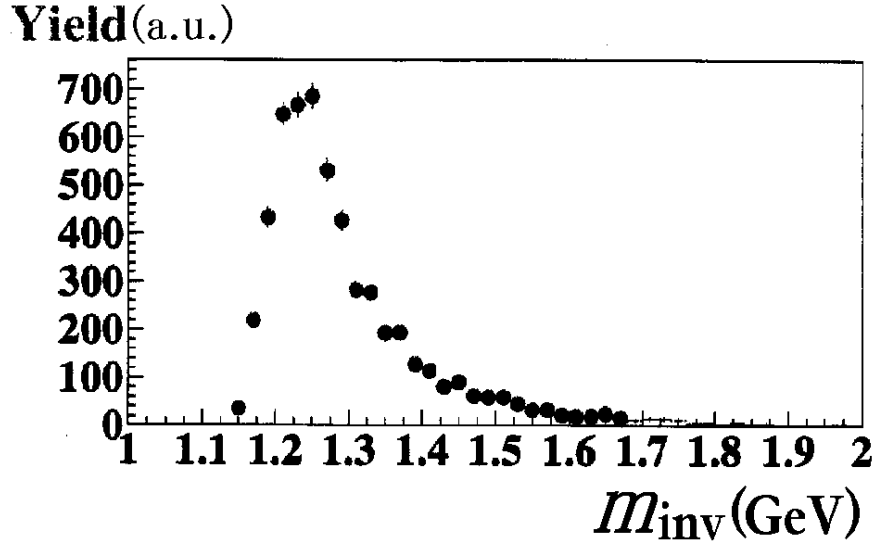


Fig. 32: invariant mass distribution of identified positive pions and protons.

(b) Invariant Mass of Mixed Event

As the spectrometer covers a fraction of the kinetic phase space of daughter particles, not all the resonance can be reconstructed. Moreover, accidental combinatorial background contaminates resonance spectra. To evaluate the background, mixed event technique is used. The accidental combinatorial background is made by particles not decayed from resonance, by daughter particles (e.g. pion and proton for delta resonance) interacting in momentum space after decay, and by daughter particles decayed from resonance but without other corresponding daughter particles measured. The accidental combinatorial background is evaluated by the invariant mass of different event, hereafter called *mixed event*.

The invariant mass of mixed events is calculated as follows. Pions are taken from an event and protons are taken from different 100 events with same category of the centrality (central events as the top 10% of minimum bias events). To extract the fraction of $\pi^+\pi^+$ among $p^+\pi^+$ -pairs N_{pair} , the assumption that the mixed event invariant mass spectrum has the same shape as the combinatorial background in the real events. The mass resolution of the $p^+\pi^+$ is estimated from momentum resolution, and the about a few MeV. A pion from an event and a proton from the other hundred events which have similar centrality (about 10 % top of minimum bias event measured by the hadron calorimeter MIRAC; $E_{MIRAC} > 326.05$ channel)

and have the same local multiplicity in the spectrometer are used to evaluate combinatorial background. It is assumed that distribution of four dimensional products of the pion's and proton's momenta not from the same events are in similar shape with the distribution of the four dimensional products of pions and protons momenta not decayed from the same delta resonance.

As described in section 4.1 , stable yield is extracted regardless of local multiplicity in the spectrometer which follows the Poisson distribution. This indicates dominant contribution of the background is accidental combinations of pion and proton, and such combinations are evaluated by the mixed events. And effects of two track separation are evaluated to be small as the chamber resolutions (of the order of some mm) are smaller than the nominal track distance (of the order of a few tens cm).

(c) Normalization of Mixed Event Spectra

The invariant mass of $p\pi^+$ pairs, m_{inv} , defined as follows gives resonances as peaks or enhancements in yields around their masses.

$$m_{inv} = \sqrt{(|\vec{E}_p + E_p|^2 + |\vec{p}_p + \vec{p}_p|^2)}$$

To extract delta yield, we assume that the invariant mass distribution, $f_{raw}(m_{inv})$, is a sum of a combinatorial background and a resonance. We evaluate the shape of combinatorial background by the mixed event distribution, $f_{mix}(m_{inv})$, with a normalization factor ϵ . Therefore the invariant mass distribution is expressed as follows;

$$f_{raw}(m_{inv}) = f_{\Delta^{++}}(m_{inv}) + \epsilon \cdot f_{mix}(m_{inv}).$$

And the shape of the resonance is assumed to be expressed by a modified Breit-Wigner function, $f_{B.W.}(m_{inv}, m_0, \Gamma)$, as follows [H⁺-92];

$$\begin{aligned}
f_{\Delta^{++}}(m_{inv}) &= f_{B.W.}(m_{inv}, m_0, \Gamma) \\
&= \mathbf{a} \cdot \frac{q^3}{q^3 + \mathbf{m}^3} \cdot \frac{1}{\left[(m_{inv.} - m_0)^2 + (\Gamma/2)^2 \right]^{3/2}},
\end{aligned}$$

where \mathbf{a} is a normalization factor of Δ^{++} resonance yield, q is the momentum of the proton (or pion) in the rest frame of the pair, i.e. half of relative momentum, and $\mu = 180$ (MeV). We assume $m_0 = 1.232$ (GeV/c²), and $\Gamma = 0.111$ (GeV), which are the values in free space. The two normalization factors, \mathbf{e} and \mathbf{a} , are defined at the \mathbf{c}^2 minimum point in the fitting.

Fig. 33 shows the extraction of Δ^{++} resonance yield by the subtraction.

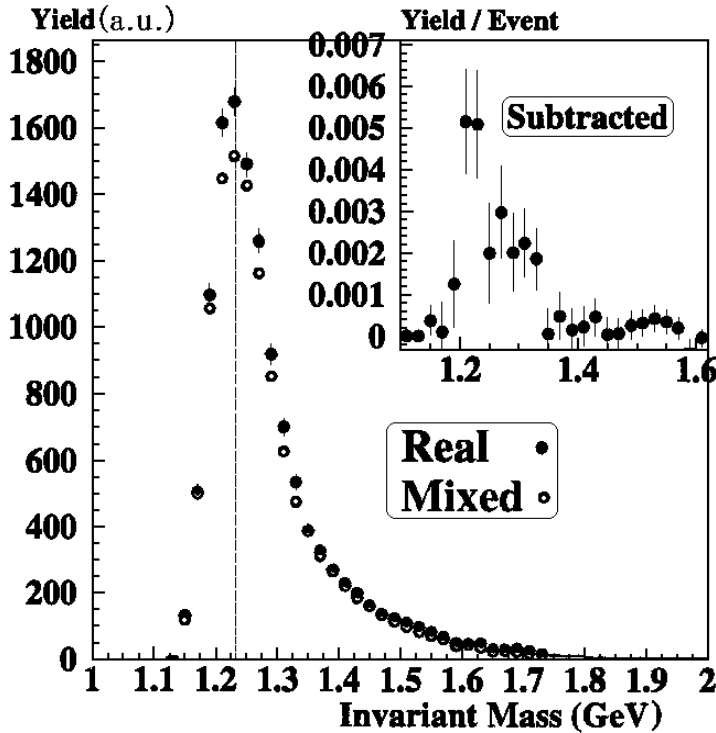


Fig. 33: Subtraction to extract delta yield.

The extracted number of Δ^{++} per event by the subtraction is 0.022 ± 0.010 , where $\chi^2/n.d.f. = 19.4 / 18 = 1.07$. The about 45% of error corresponds to the statistical fluctuation in normalization due to the similarity of invariant

mass spectra between for real events and for mixed events. The details of calculations are studied in section 4.1.1 . The extracted number of protons per event is 1.080 ± 0.010 . The error corresponds to the statistical one. The raw yields of proton and Δ^{++} per event in the Arm-II spectrometer are summarized in the Tab. 8.

	Proton	Δ^{++}
Number (raw) /spectrometer /event	$1.080 \pm 0.010(\text{stat.})$	$0.022 \pm 0.010(\text{stat.})$

Tab. 8: Raw yields of proton and Δ^{++} per event in the spectrometer (Arm-II)

3.8 Acceptance, Efficiency, and Decay Correction

For protons and positive pions identified by the time-of-flight method, transverse kinetic energy spectra are derived. Geometrical acceptance, chamber efficiencies, and particle decay correction is proceeded.

To evaluate geometrical acceptance and efficiency correction factor, a Monte Carlo simulation called GEANT [G^E-93] was used. The process to obtain the correction factors is described as follows.

(1st step) Generate a single track and make them traverse in the simulated detector positioned according to the geometrical survey. The single tracks are generated in random distribution in azimuthal angle, f , momentum, p , and cosine of the polar angle, $\cos(q)$, are used for the kinetic value. The random distributions are shown in Fig. 34.

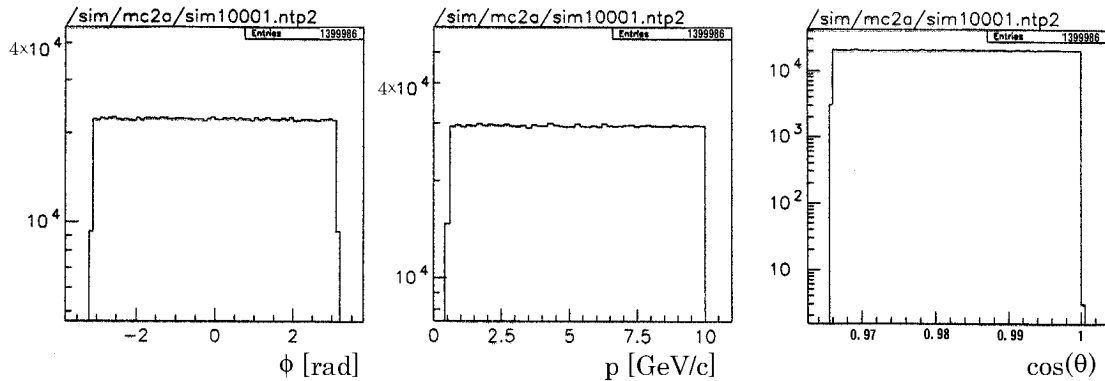


Fig. 34: Distribution of tracks used for acceptance and efficiency correction. Random distribution in azimuthal angle, f , momentum, p , and cosine of the polar angle, $\cos(q)$, are used.

The physical reaction, like energy deposit, multiple scattering, and particle decay, is simulated in the GEANT package. The decay effect of the pion is shown in Fig. 35 as a function of L/p , where L is the flight path length in meter and p is the momentum in GeV/c. As mass difference between pion and decayed particle, most of which is muon, large fraction (about 93%) of the decayed pions can be identified as pions.

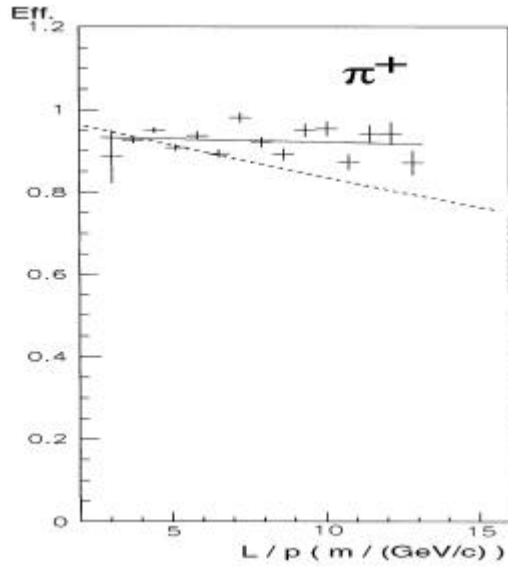


Fig. 35: (Solid line and cross) Fraction of decayed pions which are identified as pions at the TOF detector. For the comparison, fraction of decayed pion (dashed line) is shown. Note that average flight path length from target to the TOF detector is 17.9m.

(2nd step) Store hits position for each chamber with consideration of detector resolution. The resolutions are 0.5 mm and 1.7 mm for PADs in perpendicular and parallel directions to the Magnetic field, respectively. And for STDs, 3.0 mm and 6.5 mm in the same manner of directions, respectively

(3rd step) Reconstruct the tracks with hardware efficiency of the chambers. The chamber efficiencies are evaluated during the track reconstruction. The efficiency is defined as a probability to find a hit around the track, which is reconstructed by the three chambers other than the examined one out of the four tracking chambers. Namely,

$$e_i \equiv \frac{\text{Number of tracks with hit on "the chamber } i\text{"}}{\text{Number of tracks with hit on "all the 3 chambers other than the chamber } i\text{" or "4 chambers"}}$$

The efficiency for each chamber is shown in Fig. 36. The average chamber hardware efficiencies are 83.2%, 79.7%, 90.7%, and 96.8% for PAD1, PAD2, STD1, and STD2, respectively.

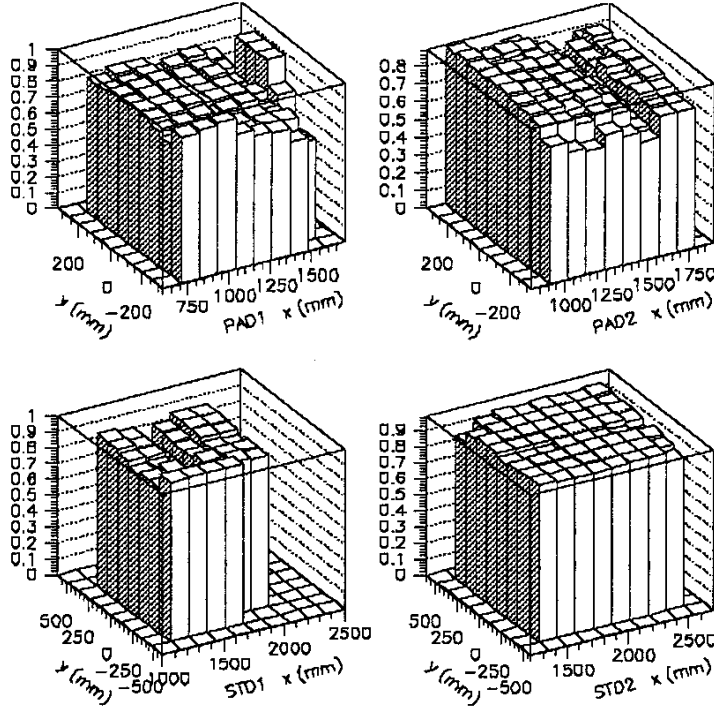


Fig. 36: Efficiency of the chambers in Arm-II. From top, for PAD1 (left) and PAD2 (right), and in bottom for STD1 (left) and STD2 (right).

(4th step) Reconstruct momentum of the particles. The same reconstruction routines as the real data are used. The procedure are already described in section 3.3 .

(5th step) Acquire the geometrical and efficiency correction factor in each bin, which is divided in the coordinate of rapidity, y , and transverse kinetic energy, m_t-m . The widths of the bins for rapidity, Dy , and transverse kinetic energy Dm_t , are $Dy = 0.25$ and $Dm_t = 0.020$ GeV. The correction factors are applied to the real data in each (y, m_t-m) bin.

For the evaluation of delta abundance as a ratio to nucleon, measured ratio is corrected acceptance and efficiency, and isospin symmetry in target and projectile nuclei. For the Geometrical acceptance and efficiency correction of the delta resonance, to reduce systematic error in the yield, the correction is applied to the ratio. The efficiency for $^{++}$ detection is the product of the efficiencies for proton and pions. The tracking efficiency, k_{track} , is 0.79 ± 0.02 both for the detection of track at least three of four

tracking chambers and for qualification of reconstruction. The particle identification efficiency, k_{pid} , is 0.60 ± 0.02 both for the detection of JTOF and for the qualification of identification. The geometrical acceptance factor, k_{geo} , is 0.145 ± 0.005 for the $\Delta^{++}/\text{proton}$ ratio for the limited azimuthal coverage. About 3 % of the errors indicated here are statistical ones due to the number of simulated tracks. Then from the raw $\Delta^{++}/\text{proton}$ ratio tabulated in Tab. 8, corrected $\Delta^{++}/\text{proton}$ ratio is calculated as 0.31 ± 0.14 . About 45 % of the error here are dominated by the statistical fluctuation in subtraction for Δ^{++} yield (for the error, see section 4.1). The error of the corrections for geometrical acceptance and efficiencies are summarized in Tab. 9.

	Proton	Δ^{++}
Number (raw) /spectrometer /event	1.080 ± 0.010	0.022 ± 0.010
$\Delta^{++}/\text{proton}$ (raw)	0.021 ± 0.009	
ε_1 (tacking in 3 cham. or 4 cham.)	0.79 ± 0.02	$(0.79 \pm 0.02)^2$
ε_2 (particle identification)	0.60 ± 0.02	$(0.60 \pm 0.02)^2$
ε_3 (geometrical)	0.1127 ± 0.0022	$0.01634^* \pm 0.00032$
Number ($\varepsilon_1, \varepsilon_2, \varepsilon_3$ corrected) /full- f /event	20.2 ± 0.6	$6.1^* \pm 2.7$
$\Delta^{++}/\text{proton}$ ($\varepsilon_1, \varepsilon_2, \varepsilon_3$ corrected)	0.31 ± 0.14	

* indicates correction where proton is assumed to be in detector acceptance.

Tab. 9: Summary of acceptance and efficiency corrections for the $\Delta^{++}/\text{proton}$ ratio. The errors indicated here are statistical ones.

3.9 Isospin Consideration

By using the measured ratio between Δ^{++} and proton (0.31 ± 0.14 , see section 3.8), the abundance of the Δ resonance is derived as a ratio with respect to number of nucleon. In the correction the following assumptions are taken.

The net baryons, namely proton and neutron, is taken into account. The numbers of up-isospin, N_u , and down-isospin, N_d , are evaluated as follows.

$$N_A = 2 \cdot N_p + N_n$$

$$N_B = N_p + 2 \cdot N_n,$$

where N_p and N_n denote number of net protons and net neutrons in incident nuclei, namely lead ions, respectively. And for four states of the Δ resonances are taken into account as being proportional to the following factors.

$$N_{\Delta^{++}} \propto \left[\frac{N_A}{N_A + N_B} \right]^3$$

$$N_{\Delta^+} \propto \left[\frac{N_A}{N_A + N_B} \right]^2 \cdot \left[\frac{N_B}{N_A + N_B} \right]^1$$

$$N_{\Delta^0} \propto \left[\frac{N_A}{N_A + N_B} \right]^1 \cdot \left[\frac{N_B}{N_A + N_B} \right]^2$$

$$N_{\Delta^-} \propto \left[\frac{N_B}{N_A + N_B} \right]^3$$

Then, those factors are carried for all nucleons in lead ion with $N_p=82$ and $N_n=126$. Then the corresponding numbers to Δ 's are $N_{\Delta^{++}} = 41.4$, $N_{\Delta^+} = 48.1$, $N_{\Delta^0} = 55.1$, $N_{\Delta^-} = 63.4$. At last the factor between $N_D/N_{nucleon}$ and $N_{D^{++}}/N_p$ comes out to be 2.0. Therefore the isospin corrected Δ /nucleon ratio is 0.62 ± 0.28 . The following Tab. 10 summarize the Δ^{++} / proton and Δ /nucleon ratios.

Δ^{++} / proton (acceptance and efficiency corrected)	0.31 ± 0.14
Δ / nucleon (isospin corrected)	0.62 ± 0.28

Tab. 10: D/ nucleon ratio corrected for isospin asymmetry. The measured D^{++} / proton ratio is also shown.

4. Experimental Results

For proton and positive pion, transverse momenta are measured in central Pb + Pb collisions. And Δ resonance abundance with respect to the nucleon is measured in proton- π^+ invariant mass in the 158 A GeV Pb + Pb central collisions.

4.1 Error Evaluation

In the acceptance and efficiency correction, bins divided in m_t and y with statistical error within two percents are used. Especially at a few bins from the edge of the acceptance this requirement is applied. Therefore dominant contribution of the statistical error in single spectra is coming from statistics of the real data in each m_t - y bin. Also about 10% systematic error for the efficiency due to high multiplicity is evaluated through the Monte Carlo simulation. For the Δ^{++} yield, due to the similarity of invariant mass spectra between the real events and the mixed events, the following possibilities are studied for cause of error. One is statistical fluctuation of the combinatorial background in the $p\pi^+$ invariant mass. The other is systematic fluctuation of subtracted Δ^{++} yield as fitting method dependences.

4.1.1 Statistical Fluctuation in Subtraction of Combinatorial Background

The error of Δ^{++} resonance yield, d , is calculated by the following way. The Δ^{++} resonance yield in the i -th bin of the invariant mass, $N_{\Delta^{++}}(i)$, is given as follows.

$$N_{\Delta^{++}}(i) = N_{raw}(i) - e \cdot N_{mix}(i),$$

Eq. 1

where $N_{raw}(i)$ and $N_{mix}(i)$ are the number of $p\pi^+$ pairs in the i -th bin for the raw data and for the mixed events, respectively.

We define error of the Δ^{++} resonance yield as a sum of errors in the i -th bins,

$\mathbf{d}_{N_{\Delta^{++}}(i)}$. And the error is propagated by the partial differential of the

Eq. 1 as follows.

$$\begin{aligned} \mathbf{d}^2 &\equiv \sum_i \left[\left(\frac{\partial \mathbf{d}_{N_{\Delta^{++}}(i)}}{\partial N_{raw}(i)} \right)^2 \right] \\ &= \sum_i \left[\left(\frac{\partial \mathbf{d}_{N_{\Delta^{++}}(i)}}{\partial N_{raw}(i)} \right)^2 + \mathbf{e}^2 \cdot \left(\frac{\partial \mathbf{d}_{N_{\Delta^{++}}(i)}}{\partial N_{mix}(i)} \right)^2 \right], \end{aligned}$$

where $\mathbf{d}_{N_{raw}(i)}$, $\mathbf{d}_{\mathbf{e}}$, and $\mathbf{d}_{N_{mix}(i)}$ are errors of $N_{raw}(i)$, \mathbf{e} , and $N_{mix}(i)$, respectively. For evaluation of the $\mathbf{d}_{\mathbf{e}}$, we use the following approximation.

$$\begin{aligned} \mathbf{e} &\cong \frac{N_{raw} - N_{\Delta^{++}}}{N_{mix}} \\ &\equiv \tilde{\mathbf{e}}, \end{aligned}$$

where

$$\begin{aligned} N_{raw} &= \sum_i N_{raw}(i) \\ N_{\Delta^{++}} &= \sum_i N_{\Delta^{++}}(i) \\ N_{mix} &= \sum_i N_{mix}(i) \end{aligned}$$

then $\mathbf{d}_{\mathbf{e}}$ is expanded by error propagation formula as follows.

$$\mathbf{d}_{\mathbf{e}}^2 = \left[\frac{1}{N_{mix}} \right]^2 \cdot \left[\left(\mathbf{d}_{N_{raw}} \right)^2 + \left(\mathbf{d}_{N_{\Delta^{++}}} \right)^2 + \tilde{\mathbf{e}}^2 \cdot \left(\mathbf{d}_{N_{mix}} \right)^2 \right],$$

where $\mathbf{d}_{N_{raw}}$, $\mathbf{d}_{N_{\Delta^{++}}}$, and $\mathbf{d}_{N_{mix}}$ are errors of N_{raw} , $N_{\Delta^{++}}$, and N_{mix} , respectively. Each of errors is evaluated from statistical fluctuation as

follows.

$$\begin{aligned}
|d_{N_{raw}(i)}|^2 &= N_{raw}(i), \\
|d_{N_{mix}(i)}|^2 &= N_{mix}(i), \\
|d_{N_{raw}}|^2 &= N_{raw}, \\
|d_{N_{\Delta^{++}}}|^2 &= N_{\Delta^{++}}, \\
|d_{N_{mix}}|^2 &= N_{mix},
\end{aligned}$$

We finally rewrite \mathbf{d} as follows.

$$\begin{aligned}
\mathbf{d}^2 &= N_{raw} \\
&+ \tilde{\mathbf{e}}^2 N_{mix} \\
&+ \frac{\left(|N_{raw}| + |N_{\Delta^{++}}| + \tilde{\mathbf{e}}^2 \cdot |N_{mix}| \right)}{|N_{mix}|} \cdot \sum_i |d_{N_{mix}(i)}|^2
\end{aligned}$$

Eq. 2

The error of delta abundance, $\frac{\mathbf{d}}{N_{\Delta^{++}}}$, is 45 %. Fraction of the three terms shown Eq. 2 in the error is 50.0%, 49.9%, and less than 0.1%, respectively. The first two terms are caused by the fact that large fraction of the combinatorial background exists in the invariant mass of the real event.

The error is mostly dominated by the statistical fluctuation in the number of Δ^{++} .

4.1.2 Fitting Method Dependence in Subtraction of Combinatorial Background

To evaluate systematic fluctuation in subtraction of combinatorial background, fitting method dependences are studied. In the section 3.8 , while whole the region in the invariant mass is used for the normalization, other method called *tail method* is also used.

The subtraction in the tail method is shown in Fig. 37. Horizontal axis is invariant mass in GeV/c². The insert shows subtracted peak of the Δ^{++}

resonance, and the mass, E_0 , and the width, Γ , of the resonance can be reasonably extracted. The fitted value of the mass and width are 1.237 ± 0.006 MeV and 0.086 ± 0.014 MeV, respectively. The error shown in the insert is only for fitting. The subtracted yield as Δ^{++} yield in the tail method in an event is 0.021. The difference between the two methods in normalization (using whole region and using only tail region) is 4 % of extracted yield.

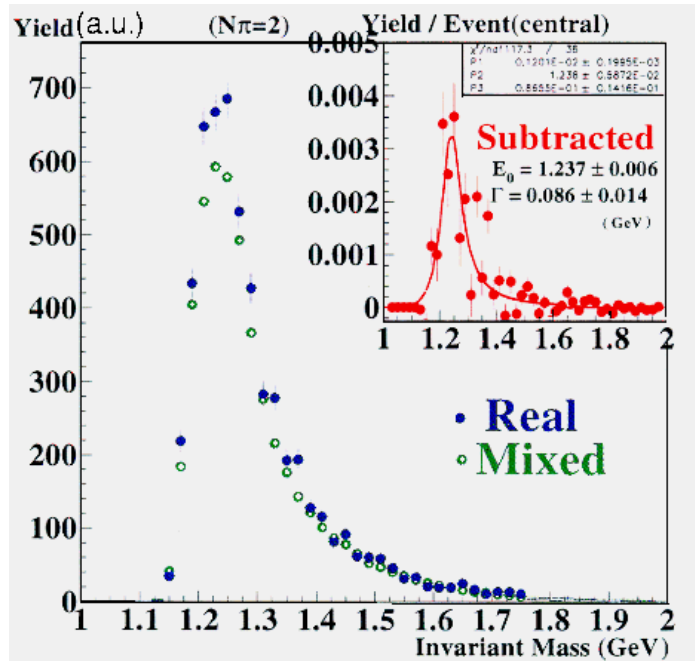


Fig. 37: Subtraction of combinatorial back ground by tail method. Invariant mass spectra for real events (filled circle) and for mixed events (open circle) are shown. The insert shows subtracted yield of D^{++} . The error shown is only for fitting.

4.1.3 Dependence on Local Multiplicity

The In the tail method, only the high invariant mass region is used for the normalization of mixed event spectrum. This method may be sensitive to the shape of the tail region, the events are divided by the local multiplicity of the pions (Arm-II). Fig. 38 shows the local multiplicity, Np , distribution. The solid line is the fitted line with Poisson distribution. From the distribution, 3% of the events are deviated. Average local multiplicity, $\langle Np \rangle$, is 2.6.

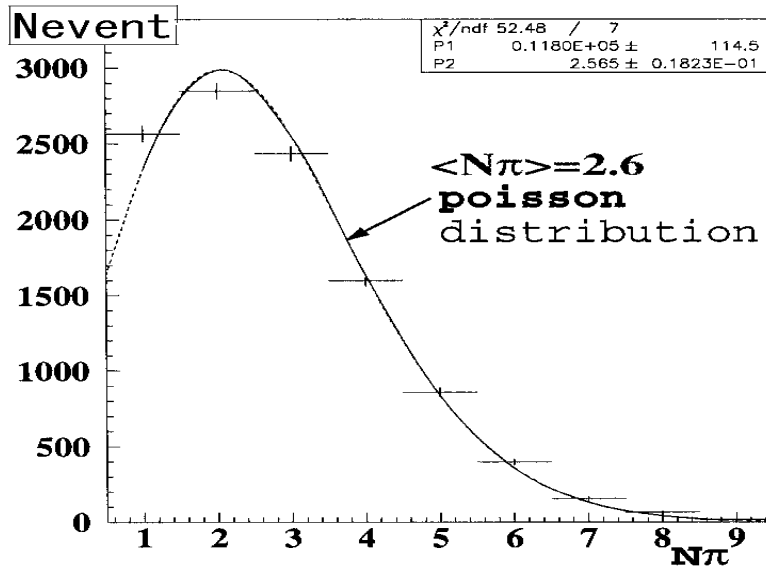


Fig. 38: Local multiplicity, N_p , distribution. N_p is number of pion in the spectrometer (Arm-II). The mean value $\langle N_p \rangle$ is 2.6.

For each local multiplicity, threshold dependences are studied. Fig. 39 shows the dependence. The stable subtraction can be done for the lower threshold below about 1.6 GeV in invariant mass, M_{inv} . Less dependence on the local multiplicity can also be found. The subtracted yield in an event is 0.021 with fluctuation of 0.003. The difference among subsets of events divided by the local multiplicity is 13 % of extracted Δ^{++} yield.

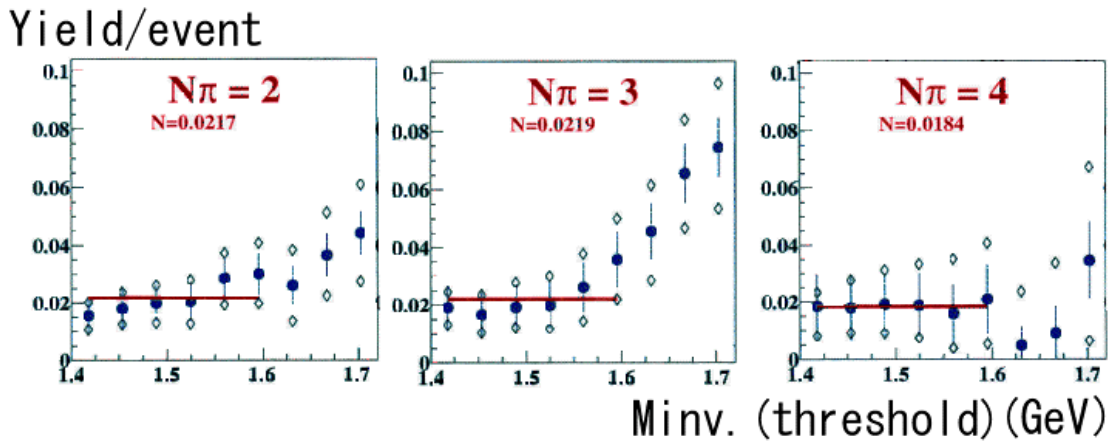


Fig. 39: Dependence on threshold value of invariant mass in normalization for the tail method. Different histogram shows local multiplicity, N_p , dependence.

4.2 Transverse Momentum Distribution

Transverse momentum distributions are usually presented in terms of the invariant cross section. Study of the m_t differential invariant yield (hereafter, simply called as the invariant differential yield) is important since this quantity represents how much incident energy is transferred to the energy of produced particles during collisions. Fig. 40 shows inclusive transverse kinetic energy spectra for positive pions and protons in central events. The centrality of the events is top 10 % of minimum bias as described in section 3.6 . Filled circle and open circle represent positive pion and proton measured by WA98 experiment, respectively. For the comparison, results by NA44 experiments are overlaid. Open triangle and open diamond mark represent positive pion and proton measured by NA 44 experiment, respectively. Shapes of the spectra are similar with each other.

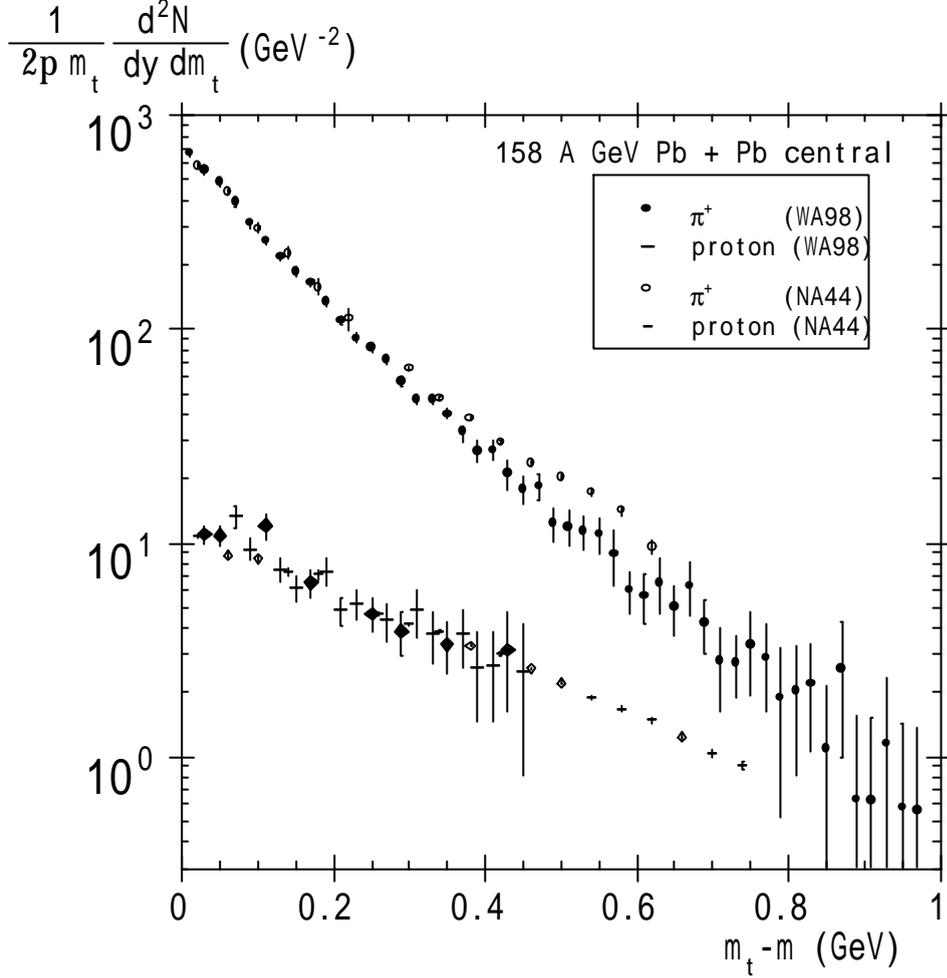


Fig. 40: Inclusive m_t spectra for proton and positive pion for 158 A GeV Pb + Pb central collision (top 10% of minimum bias). (Closed circle: positive pion by WA98, Closed diamond: proton by WA98). For the comparison, positive pion by NA44 (Open circle), and proton by NA44 (Open diamond) are shown.

The slope of the spectra is fitted with a single exponential as follows.

$$\frac{1}{m_t} \cdot \frac{d^2N}{dm_t dy} = N_0 \cdot \exp\left[-\frac{m_t - m}{T}\right]$$

Eq. 3

Here N_0 is a normalization constant and T is an inverse slope. These two valuables are fitting parameters. Inverse slope for the positive pion above

0.20 GeV in $m_t - m$ is 142 ± 3 MeV, and slope for the proton is 251 ± 25 MeV. NA44 shows 156 ± 3 MeV for positive pion and 289 ± 7 MeV [N⁴⁴-96]. When the differential yield shown as Eq. 3 is integrated by m_t , the rapidity density, dN/dy , is evaluated as

$$\begin{aligned} \frac{dN}{dy} &= \int_m^\infty \frac{d^2N}{2\mathbf{p}m_t dm_t dy} \cdot 2\mathbf{p}m_t dm_t \\ &= 2\mathbf{p}N_0 T(T+m). \end{aligned}$$

For the rapidity density of the pion, approximation of spectrum by a sum of two exponential is used as follows,

$$\begin{aligned} \frac{d^2N}{2\mathbf{p}m_t dm_t dy} &= \frac{1}{2\mathbf{p}T_1(T_1+m)} \cdot \frac{1}{1+w} \cdot \frac{dN}{dy} \cdot \exp\left[-\frac{m_t-m}{T_1}\right] \\ &+ \frac{1}{2\mathbf{p}T_2(T_2+m)} \cdot \frac{w}{1+w} \cdot \frac{dN}{dy} \cdot \exp\left[-\frac{m_t-m}{T_2}\right]. \end{aligned}$$

where T_1 , T_2 , w , and dN/dy are parameters. Evaluated rapidity densities are 138 ± 16 for positive pion, and 25 ± 6 for proton. For the comparison, NA44 shows the rapidity density as 155 ± 10 for pion, and 27 ± 5 for proton. NA44 shows slightly higher inverse slope and rapidity density as their centrality is slightly higher. As described in 3.6, our centrality is top 10% measured by hadronic calorimeter around mid rapidity. The data shown for NA44 is top 3.7% measured by scintillation multiplicity counter (what they call *T0 counter*, and the counter covers pseudo-rapidity range $0.6 \leq \mathbf{h} \leq 3.3$). Evaluation of corresponding impact parameter for NA44 is less than 4.5 fm [K^a-99], while evaluated value of the impact parameter for WA98 is less than 5 fm [S^c-98].

4.3 D/Nucleon Ratio

The yields of proton and Δ^{++} , and correction factors are summarized in Tab. 11. The errors in the table are statistical errors.

	Proton	Δ^{++}
Number (raw) /spectrometer /event	1.080 ± 0.010	0.022 ± 0.010
$\Delta^{++}/$ proton (raw)	0.021 ± 0.009	
ϵ_1 (tacking in 3 cham. or 4 cham.)	0.79 ± 0.02	$(0.79 \pm 0.02)^2$

ε_2 (particle identification)	0.60 ± 0.02	$(0.60 \pm 0.02)^2$
ε_3 (geometrical)	0.1127 ± 0.0022	$0.01634^* \pm 0.00032$
Number ($\varepsilon_1, \varepsilon_2, \varepsilon_3$ corrected) /full- f /event	20.2 ± 0.6	$6.1^* \pm 2.7$
$\Delta^{++}/$ proton ($\varepsilon_1, \varepsilon_2, \varepsilon_3$ corrected)	0.31 ± 0.14	
$\Delta/$ nucleon (isospin corrected)	0.62 ± 0.28	

* indicates correction where proton is assumed to be in detector acceptance.

Tab. 11: Baryon yields and the statistical errors (see text)

The errors including systematic errors discussed in 4.1 are summarized in Tab. 12. The last column named *Descriptions* in the table shows the corresponding section for the evaluation of the value. The Δ /Nucleon ratio is 0.62 ± 0.28 (stat.) ± 0.16 (sys.), where *stat.* and *sys.* correspond to the statistical error and systematic errors, respectively.

	Yield and Errors	Descriptions
$\Delta/\text{Nucleon Ratio}$ (Acceptance, efficiency and isospin corrected)	0.62 ± 0.28 (stat.) ± 0.16 (sys.)	Section 3.9
Statistical Fluctuation in Subtraction of Background	0.28 [45 %] (stat.)	Section 4.1.1
Uncertainty of Tracking Efficiency	0.06 [10 %] (sys.)	Section 4.1
Difference in Normalization Method	0.02 [4 %] (sys.)	Section 4.1.2
Difference for Different Local Multiplicity	0.08 [13 %] (sys.)	Section 4.1.3

Tab. 12: Summary of yield and errors of D abundance as a D/Nucleon ratio. For detail of the statistical error (stat.) and the systematical error (sys.), see corresponding section shown in the last column named *Description*.

5. Discussions

In relativistic heavy ion collisions, excited states of nucleon are expected to play important roles. First, in primary collisions of the constituent nucleons, collisions may be different from nucleon - nucleon collision in free space, which is primarily due to the short time interval of collisions ($\sim 1\text{fm}/c$). Participant nucleons collide at excited states. Second, the mean free path ($\sim 1.5\text{ fm}$) is shorter than the size of the nucleus ($\sim 7.1\text{ fm}$ for lead nucleus); re-scatterings of emitted particles also lead excited nucleons. Experimental interest is how much fractions of constituent nucleons are in such excited states. Direct measurement of lowest resonance, namely $\Delta(1232)$ shed light on this information because the chance to the lowest energy might be largest. Also by assuming two states of nucleons based on the Ising model, a derivation of parameter corresponding to a temperature is possible.

The effects of Δ abundance to the inclusive spectra of pions need to be studied. Especially for the SPS energy, as large fraction of the nucleons are in resonance states at freeze-out, therefore the effect might be large. One should note that the region where the enhancement of pion spectra is seen is the low m_t region where daughter pions from Δ decay contribute. For the consideration, other contribution like Coulomb effect should be compared.

5.1 Δ /Nucleon Ratio

As described in section 4.3 , the ratio measured in 158 A GeV Pb + Pb central (top ca. 10 % of minimum bias) collisions is 0.62 ± 0.28 (stat.) ± 0.16 (sys.). The ratio shows about two thirds of the nucleons are in excited states at the time of freeze-out. Such fractions have been measured in lower energy of nucleus - nucleus collisions at 95 A MeV [B⁺-96], and at 1 and 2 A GeV [F^{OPL}-97], and at 13.7 A GeV [E⁸¹⁴-95]. Fig. 41 shows the $\Delta(1232)$ ratios over nucleon as a function of beam energy per nucleon. As the beam energy goes higher, the Δ /nucleon ratio becomes higher. An increase of the error bars in 13.7 A GeV and more in 158 A GeV reflects the difficulty of Δ resonance measurement in relativistic heavy ion collisions. This is because larger fractions of combinatorial backgrounds due to the higher multiplicities at higher energies.

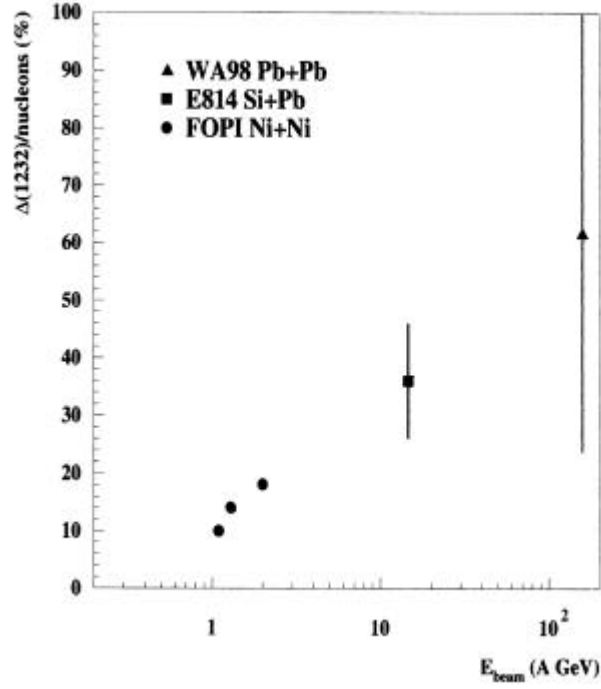


Fig. 41: the experimental ratio $\Delta(1232)$ / nucleons as a function of beam energy per nucleon.

A simple description of excited nucleons using lowest nuclear resonance states is applied to evaluate the temperature through the Ising model. Fig. 42 shows the schematic idea of the Ising model. A certain state of nucleus is expressed by a combination of filled circles, where the circles represent constituent nucleons. Two rows of circles correspond to the energy level of $\Delta(1232)$ resonances and ground state nucleons, which are at the energy of m_b and m_N , respectively. Here m_b and m_N represent the mass of $\Delta(1232)$ resonance and ground state nucleon, respectively. Out of N_0 constituent nucleons, N_D of nucleons are in $\Delta(1232)$ state, and the rest of $N_N (=N_0 - N_D)$ nucleons are in the ground state. In the figure, an example state are shown where 3 nucleons are in $\Delta(1232)$ state.

The temperature, T_{Ising} , is derived from the ratio by two values. One is energy difference, dE , and the other is entropy difference, dS , between two kinds of nuclear matter. One is a fireball including $\Delta(1232)$ resonances and ground states nucleons, and the other is a nucleus consisting of only ground states nucleons. Namely, the relation is the following.

$$T_{Ising} = \frac{dE}{dS}$$

For the energy level, mass of the $\Delta(1232)$ resonance and ground state nucleon, namely $1232 \text{ MeV}/c^2$ and $938 \text{ MeV}/c^2$, is used. When the measured ratio is applied to the model, a parameter corresponding to temperature gives $176^{+95}_{-68} \text{ MeV}$.

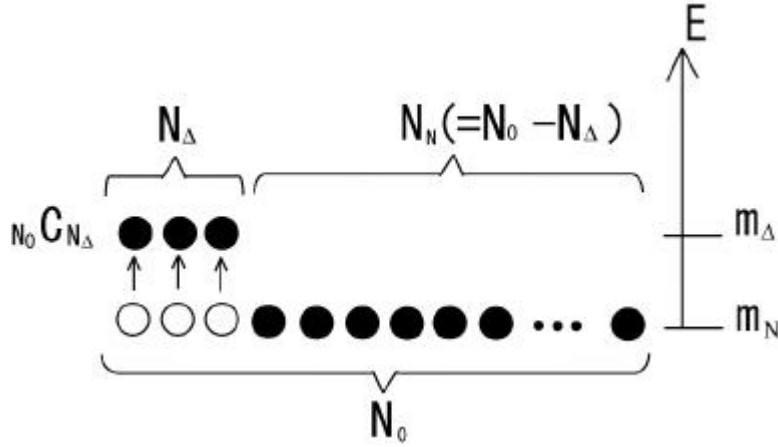


Fig. 42: Schematic drawing of the Ising model for the resonance states. Two rows of circles correspond to the energy level of $D(1232)$ and ground state nucleon, which are in the energy of m_D and m_N , respectively. The combination shown in filled circles represents a state of nucleus. Out of N_0 constituent nucleons, N_D of nucleons are in $D(1232)$ state, and the rest of $N_N (= N_0 - N_D)$ nucleons are in the ground state. In the figure, an example state are shown where 3 nucleons are in $D(1232)$ in state (see text).

5.2 Single-Particle Spectra and Two-Particle Correlation in Expanding Fireball Picture.

During later stages of development of the nucleus - nucleus collision, the hadronic fireball expands. This is reasonable because the average (transverse) kinetic energy ($> 100 \text{ MeV}$ per nucleon) is much larger than the typical binding energy ($\sim 8 \text{ MeV}$ per nucleon). As the system expands, frequency of interactions of particles in the fireball decreases. When interactions cease, the situation is often called freeze out. Evaluation of temperature at the freeze out gives information to reconstruct an equation of states of the fireball.

For experimental approaches, different kinds of observables are proposed.

As examples, inclusive single-particle spectra and two-particle correlations are of prime interest. For the inclusive single spectra of transverse kinetic energy, namely m_t spectra, slopes are studied. When the fireball has collective motion during the expansion, velocity of the collective expansion affects the transverse spectra. Corresponding to a common expansion velocity, the transverse kinetic energies for different particle species are different due to the difference in mass. Therefore, to measure the temperature and collectivity of the fireball, shapes of different particle species are useful. Also two-particle correlations, like HBT effects, are used. When collective motion exists, transverse radius measured through the HBT correlation has m_t dependences. From the study of m_t dependencies, a constrain on collective velocity and temperature can be obtained.

Though the low m_t enhancement of pion spectra cannot be explained, the interpretation with expanding fireball picture shows a consistent description with thermal freeze out at temperature, T , and a collective radial expansion velocity, b , where an examples of the value are $T \sim 139$ MeV and $b \sim 0.42c$. Those values are used for m_t spectra of kaons, protons, and not-low- m_t of pions and two-particle HBT correlations [S^{SX}-98].

The fitted value to our single particle spectra of proton is 143 ± 8 MeV for temperature, and $0.40c \pm 0.05c$ for the transverse velocity as shown in Fig. 43, which is consistent with the other experiment [S^{SX}-98]. The parameterization of the fit is the expression-1 in the section 5.3.2.3 , which is used in the interpretation of for the pion spectra.

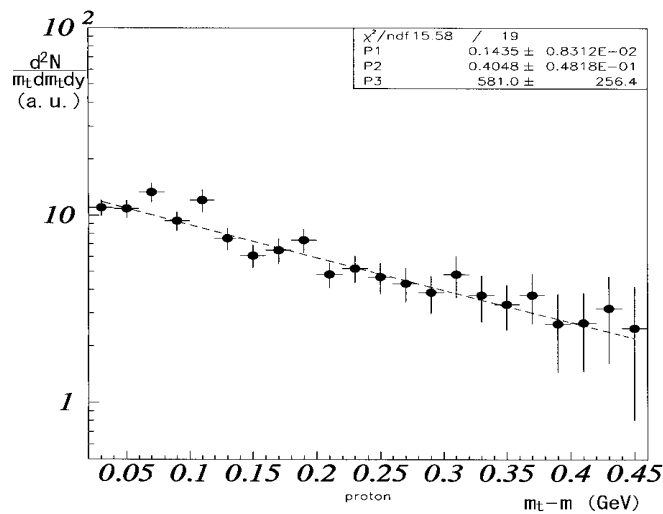


Fig. 43: Proton spectra with parameterization of the expanding fireball (dashed line. see text for detail).

5.3 Low m_t Enhancement of Pion Spectra

While the consistent interpretation can be achieved in expanding fireball picture both for single particle spectra and for two-particle correlation, the low m_t region of pion spectra is not used to extract the temperature nor the collectivity. The m_t spectrum of inclusive positive pion is shown in the Fig. 44 for 158 A GeV Pb + Pb central (top 10 % of minimum bias) collisions. The horizontal axis is transverse kinetic energy, $m_t - m$, in GeV. And the vertical axis is the invariant yield in logarithmic scale. The enhancement is easy to see when the local slope is shown. Clear departure from a single exponential shape is seen below 0.2 GeV. The local slopes are derived in neighboring data points of the pion m_t spectrum. The local slopes are plotted in the insert of Fig. 44. Horizontal axis shows transverse kinetic energy at the center of the fitting region. A decreasing tendency of the local slope parameters in lower m_t region represents the low m_t enhancement. While rapidity and transverse momentum of our acceptance is correlated as shown in Fig. 16, difference of the pion yield in our acceptance is about 2.5% [N⁴⁹⁻⁹⁹], which is within the marks of Fig. 44. It should be noted that contribution of hard components is reported as enhancement in higher region than about 2.8 GeV in $m_t - m_0$, in proton - nucleus collisions, and called Cronin effect [C⁺⁷⁵]. Therefore the effect from hard components is small for the low m_t enhancements discussed here.

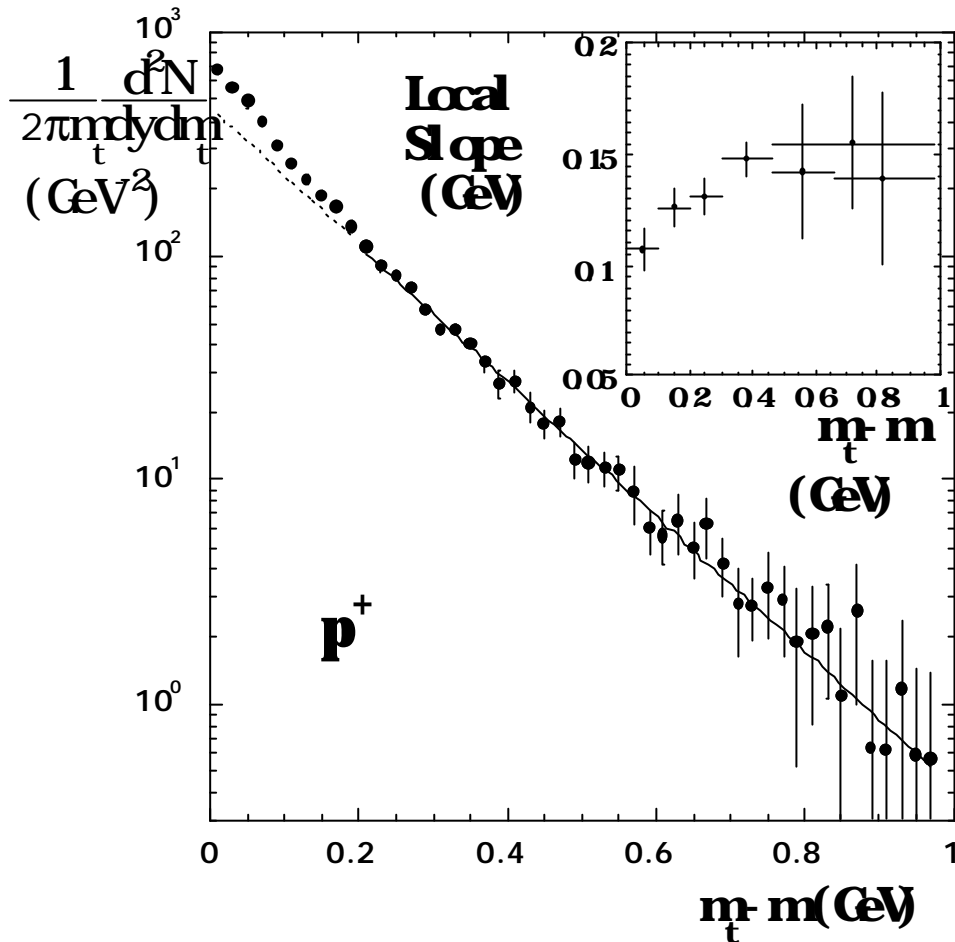


Fig. 44: Inclusive m_t spectrum for positive pion in 158 A GeV Pb +Pb central collisions (top 10 % of minimum bias). The solid line is an exponential fit for the data above 0.2 GeV in $m_t - m$, and the dashed line is the extrapolation to the lower m_t region. In the insert, local slope parameters of positive pion as a function of center value of the fitting region in $m_t - m$ mass (GeV) are shown.

5.3.1 Proton - Proton Collision

As a comparison, inclusive positive pion m_t spectrum in mid-rapidity in proton - proton collisions at $s^{1/2} = 23$ GeV are shown in Fig. 45 [BS-75]. The horizontal axis is transverse kinetic energy, $m_t - m$, and the vertical axis is

the invariant cross section. The solid line is an exponential fit with χ^2/ndf of 8.83/6. The inverse slope is 153 ± 3 MeV. The m_t spectrum is well described in the exponential function. Although slight enhancement at < 0.2 GeV is seen even in proton - proton collisions, compared with nucleus - nucleus collisions, this enhancement is much small.

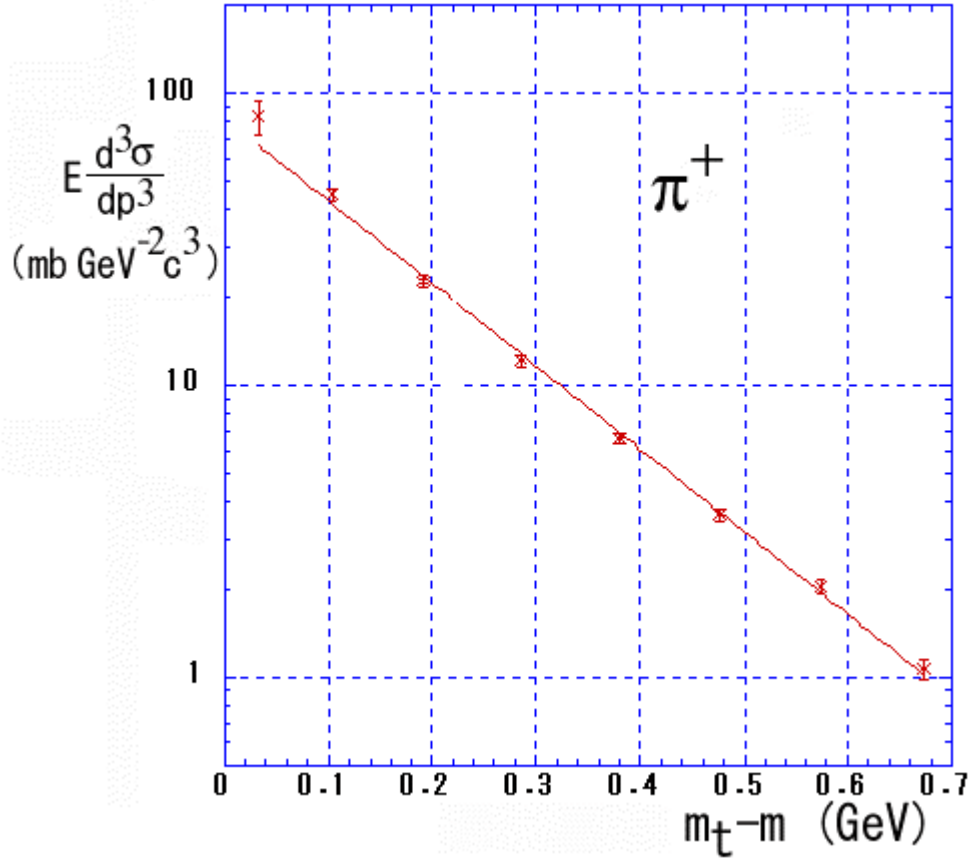


Fig. 45: positive pion transverse kinetic energy spectrum in proton - proton collisions at the center of mass energy of 23 GeV [B^S-75]. The solid line is an exponential fit with goodness in χ^2/ndf of 8.83/6.

5.3.2 Source of Low m_t Enhancement

As candidates of possible source of the low m_t enhancement, the following mechanisms are considered in nucleus - nucleus collisions.

(1) Collective motion

In relativistic nucleus -nucleus collisions, hot and/or dense fireball

regions are created. In the region, mean free paths for produced hadrons (~ 1.5 fm) are shorter than the size of nucleus (~ 7.1 fm for ^{208}Pb nucleus). And the (transverse) kinetic energy (> 100 MeV per nucleon) is much larger than the binding energy of nucleus (~ 8 MeV per nucleon due to the saturation of nuclear force). Because of the kinetic energy large enough not to be bound, and a short mean free path, it leads collective expansion of the fireball. The collectivity is expected to be commonly seen in different particle species. From a naive relation of kinetic energy as $m\mathbf{b}^2$ where m is particle mass and \mathbf{b} is a velocity to characterize the collectivity, particle species with lighter mass is affected in smaller kinetic energy. Therefore for lighter mass particle like pions, enhancement is expected in low m region.

(2) Coulomb effect

In relativistic nucleus - nucleus collisions a large number of charged particles are concentrating in an interaction region, and the net charge must be positive. The transverse kinetic energy distributions of charged particles are affected by the Coulomb effect. Most extreme case can be evaluated by the Gamov correction assuming all the charges of incident nuclei are located at the collision point.

(3) Resonance contribution

In relativistic nucleus - nucleus collisions, produced particles are readily excited. One of the reasons is short time interval of the primary collisions of constituent nucleons. This enables the primary collisions in excited states rather than nucleon - nucleon collisions. And other reason is multiple secondary interactions after primary collisions. The decay of the resonances especially resonance of the nucleons are contributing to the low m_t enhancement.

5.3.2.1 Collective Motion

In heavy ion collisions, high particle multiplicity and short mean free paths result collective motion of participant nucleon and produced particles. In such case, common features in transverse mass spectrum among different particle species can be derived.

In order to evaluate effects of such collectivity to transverse spectra, one of typical pictures, hydro dynamical description, is applied. Hydro dynamical developments of the thermalized hot and/or dense system are based on equations of state [S^{SX}-98]. Fig. 46 shows transverse mass distributions for protons, positive kaons and positive pions. Solid lines represent hydro dynamical developments of collective system with a freeze out temperature of 139 MeV and a collective (radial) velocity of 0.42c. And the dashed line is a pure exponential line. As is expected, solid curve shows concave shape, creating low m_t enhancement relative to single exponential shape. But still disagreement is seen in the low m_t region of pions.

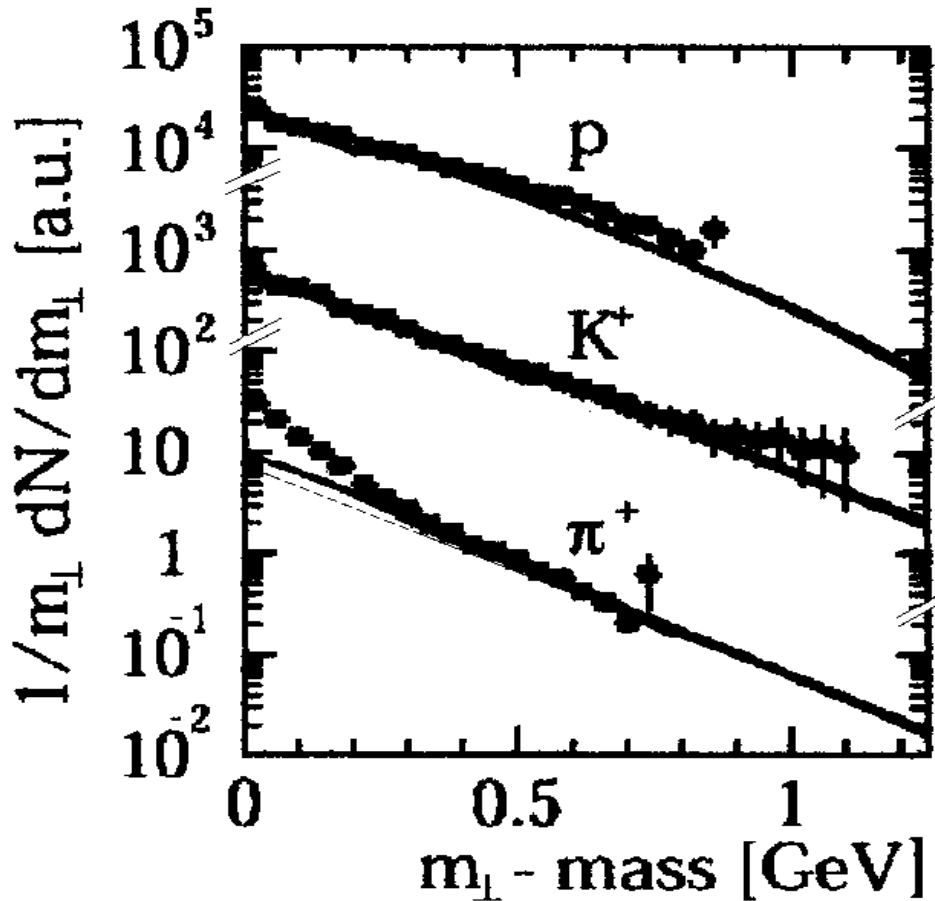


Fig. 46: Hydro dynamical description for three particle species (protons, K^+ , and π^+). Discrepancy for pion is seen for lower transverse mass region [S^{SX}-98]. The dashed line for the pion spectrum is an exponential line for eye guide.

5.3.2.2 Coulomb Effects

In the interaction region of relativistic nucleus-nucleus collisions, charges of protons in the target and the projectile are concentrated. From the positively charged source, negative pions get attractive forces, and positive pions get repulsive forces [Hⁱ-99]. Fig. 47 shows invariant differential cross section for the negative and the positive pions [K^a-99]. Both negative and positive pions have much larger enhancements than the level of the difference with each other. This means the main source of the low m_t enhancements is different from the Coulomb effects.

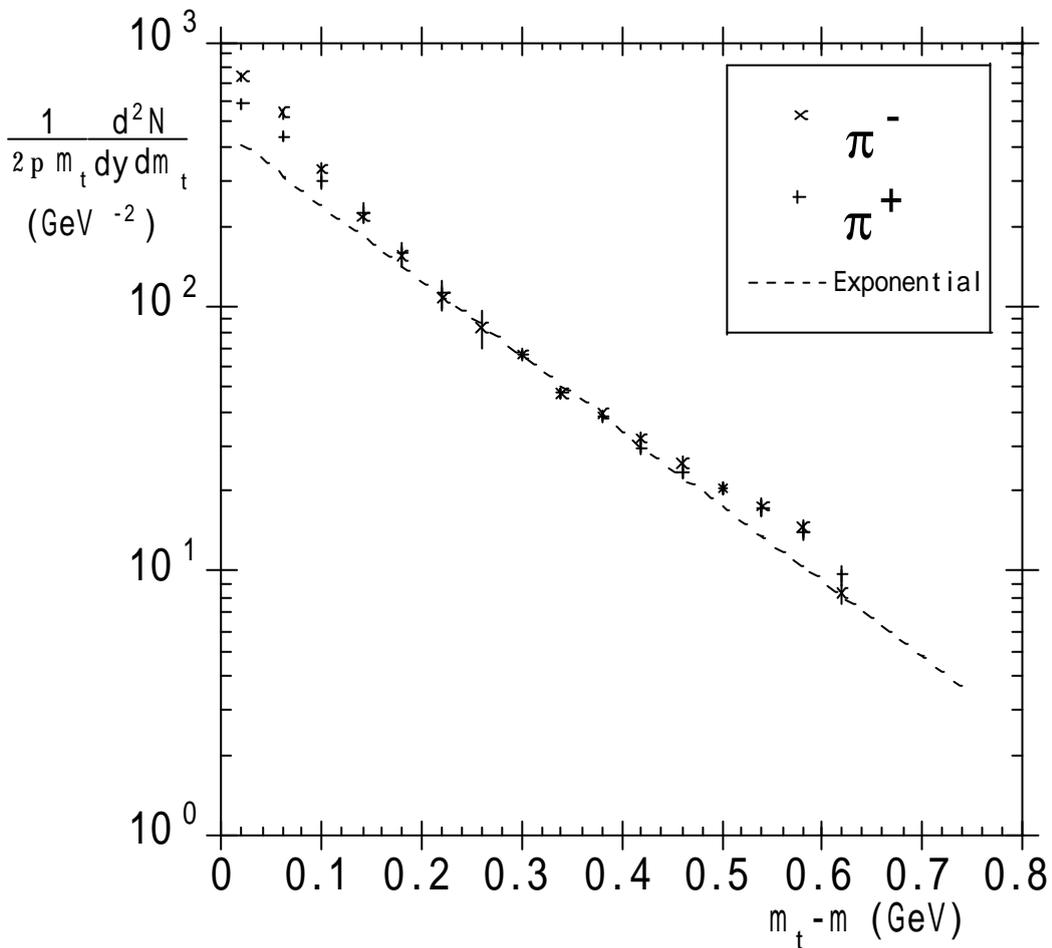


Fig. 47: Invariant cross section for the negative pion (crossing sign) comparing to positive pion (plus sign) [K^a-99]. For an eye guide, an exponential line is shown as a dashed line.

For a closer look, the ratio between positive and negative pion is plotted in

Fig. 48 [N⁴⁴⁻⁹⁶]. The difference from the unity in the experimental data (closed circle) is represented by considering Coulomb effects (open circle) in a cascade simulation, while without Coulomb effect (open triangle) such representation is hardly possible. Therefore the Coulomb effect explains the difference between positive pion and negative pion below 0.1 GeV, but the larger enhancement seen below 0.2 GeV both for positive and negative pion should be due to other reasons.

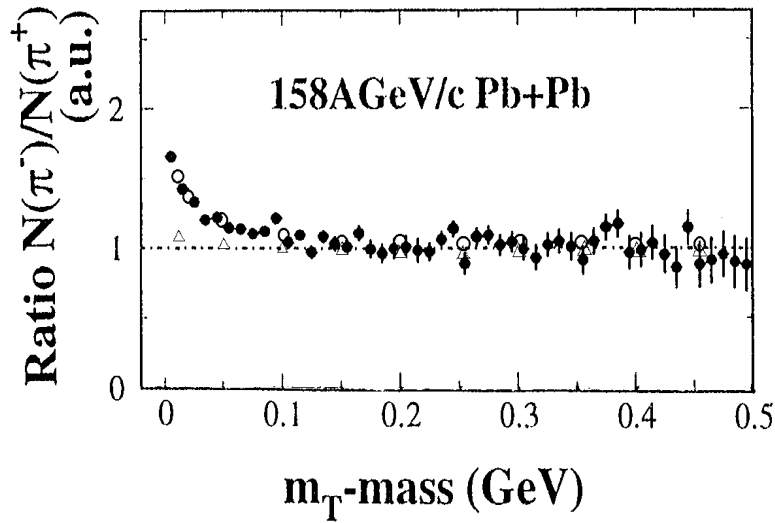


Fig. 48: Ratio of yield between negative pion and positive pion. Experimental data (Closed circle) and simulation (RQMD v.1.08) with Coulomb effects (Open circle). For the comparison, the simulation without Coulomb effects are also shown (Triangle), where the slight difference from the unity is coming from acceptance effects.

5.3.2.3 Contribution from Resonances

In the relativistic nucleus-nucleus collisions, excited states are readily created not only by the primary collisions, but also by the secondary collisions. First insight of such effect is possible by taking the lowest state of nuclear resonance, namely $\Delta(1232)$ resonances, into account. Pions decayed from the Δ resonances ($\Delta \rightarrow N + \pi$) are included in inclusive m_T spectra. Transverse kinetic energy of the daughter pion is much lower than that of Δ resonances. This is simply caused by decay kinematics owing to large mass difference between the nucleons ($M_N = 1.232 \text{ GeV}/c^2$, and $M_{proton} = 0.938 \text{ GeV}/c^2$) and the pions ($M_{pion^\pm} = 0.139 \text{ GeV}/c^2$) (see Fig. 12).

To consider the contribution of Δ resonance, thermal source with

collective velocity is assumed. The slope, T , of the resonance is assumed to be the same as protons.

$$T = T_p.$$

The yield of Δ^{++} is evaluated by our measured ratio, $N_{\Delta^{++}}/N_p$, as

$$dN_{\Delta^{++}}/dy = (N_{\Delta^{++}}/N_p) \times (dN_p/dy),$$

and the four charge states of delta are equally distributed as,

$$N_{\Delta}/dy = 4 \times (dN_{\Delta^{++}}/dy).$$

The yield of decayed pion from delta resonance are evaluated from following procedure. Nucleon yield for $^{208}\text{Pb}^{82} + ^{208}\text{Pb}^{82}$ system is given as,

$$dN_N/dy = (208/82) \times (dN_p/dy).$$

As four charge states of delta are decayed with following branching ratio,

$$\begin{array}{ll} ++ & p + \pi^+ (100 \%), \\ + & p + \pi^0 (50 \%) \\ & n + \pi^+ (50 \%), \\ 0 & p + \pi^- (50 \%) \\ & n + \pi^0 (50 \%), \\ - & n + \pi^0 (100 \%). \end{array}$$

Ratio between Δ^+ decayed from delta resonance and delta resonance, N_{Δ^+}/N_{Δ} , is assumed as

$$N_{\Delta^+}/N_{\Delta} = 1.5/4.$$

A factor, $f = 1 + \alpha$, should be considered, where α is the ratio between $N_{\pi^+}(\Delta \rightarrow p^{\text{scat}}, \pi^{\text{not-scat}})$ and $N_{\pi^+}(\Delta \rightarrow p^{\text{not-scat}}, \pi^{\text{not-scat}})$, where the former N_{π^+} is the number of pion decayed from delta whose daughter proton of the pion has re-scattered after the decay therefore the invariant mass hardly evaluated as delta, and the latter N_{π^+} is the number of pion decayed from delta whose daughter proton does not get additional re-scattering after decay.

$$f = 1 + \alpha,$$

where

$$\alpha = \frac{N_{\pi^+}(\Delta \rightarrow p^{\text{scat}}, \pi^{\text{not-scat}})}{N_{\pi^+}(\Delta \rightarrow p^{\text{not-scat}}, \pi^{\text{not-scat}})}$$

and the value of α is about 1.5.

The shape of the enhancements is evaluated from the contribution of the delta resonance decay. To consider the transverse kinetic energy dependence of the factor, f , a cascade simulation *JAM* [N¹-98, N²-98] is used, while the factors are less dependent on the transverse kinetic energy. The contribution of the mesonic resonance is assumed to be close to the thermal spectrum.

The contribution of higher baryonic resonance is about a tenth of the lowest resonance, the main $\Delta(1232)$ contributing is only considered. The results is shown in Fig. 49.

The single particle spectra, $P_1(m_t, y)$, of pions from expanding fireball is described as follows [N⁴⁹-98, C^{SH}-95]. It refers to the space-time source function [H⁺-96] as was used for the correlation function described in section 1.2.3.

$$\begin{aligned}
 P_1(m_t, y) &\propto m_t \cdot R_*^2 \cdot \Delta \mathbf{h}_* \\
 &\times \left\{ \left| 1 + \frac{R_*^2}{2R_G^2} \partial \Delta \mathbf{h}_*^2 - \frac{m_t}{8T} \partial \Delta \mathbf{h}_*^4 \right| \right\} \\
 &\times \exp \left\{ \left| \frac{m_t}{T} + \frac{\mathbf{b}_t^2 (m_t^2 - m^2)}{2T(T + m_t \mathbf{b}_t^2)} - \frac{0.5y^2}{\partial \Delta \mathbf{h}_*^2 + T/m_t} \right| \right\},
 \end{aligned}$$

Expression - 1

where

$$\frac{1}{R_*^2} \equiv \frac{1}{R_G^2} \left| 1 + \mathbf{b}_t^2 \frac{m_t}{T} \right|$$

and

$$\frac{1}{\partial \Delta \mathbf{h}_*^2} \equiv \frac{1}{\partial \Delta \mathbf{h}^2} + \frac{m_t}{T}.$$

Here T is the temperature, and \mathbf{b}_t is the transverse expansion velocity. And R_G is geometrical source radius which is assumed to be 6.5 fm and $\Delta \mathbf{h}$ is width of source in the space-time rapidity, which is related to the width of the rapidity distribution $\mathbf{D}y$ as follows.

$$\partial \Delta y^2 = \partial \Delta \mathbf{h}^2 + \frac{T}{m_t}.$$

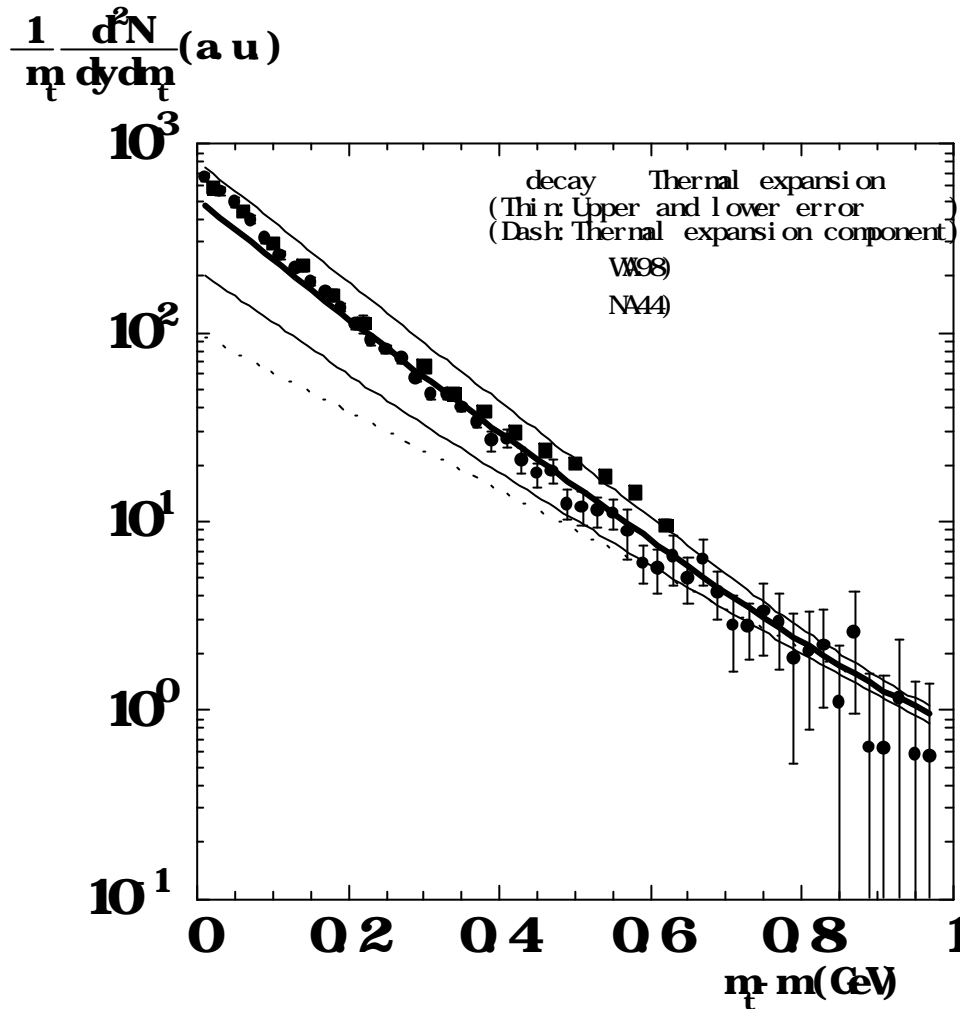


Fig. 49: Comparison of inclusive p^+ spectra at SPS energy. Closed circle, and closed square shows experimental data by WA98 and NA44 [K^a-99]. and thick solids line shows delta decay contribution plus a thermal source with expansion (2 thin lines are lower and upper limits of error coming from uncertainty of delta measurement and uncertainty of parameter in thermal plus expansion model). For the comparison, the dotted line shows only contribution from a thermal source with expansion.

Though the error is large due to the uncertainty of the determination of delta yield resulted from huge combinatorial background in the invariant mass of the resonance, the shape of the enhancement is consistent with the experimental measurement. A slight higher value in data than the calculation might indicate contributions of the higher baryonic resonance

6. Conclusions

We have presented the results of single particle spectra and direct measurement of Δ resonance yield in $p\pi^+$ decay channel in Pb + Pb collisions at the energy of 158 A GeV, at WA98 experiment using Super Proton Synchrotron (SPS) of the European organization for nuclear research (CERN).

For systematic study of hadron production in relativistic heavy ion collisions near mid rapidity region, we have constructed a magnetic spectrometer, called Arm-II. It is designed for good particle identification capability under the condition of high particle density and for large momentum coverage in Pb + Pb collisions at SPS. Using the data taken by the Arm-II spectrometer, single particle spectra and Δ resonance yield are analyzed.

For the single particle, we have carried out the analysis of transverse kinetic energy spectra for π^+ and proton. By using single exponential fitting, inverse slope parameter is 142 ± 3 MeV (fitting region $m_t - m > 0.2$ GeV), and 251 ± 25 MeV. In the transverse kinetic energy spectra of pion, we have observed clear low- m_t enhancement.

We have evaluated Δ resonance yield with $p\pi^+$ invariant mass distribution. Considering the isospin asymmetry in incident $^{208}\text{Pb}^{82+}$ nuclei, $\Delta/\text{nucleon}$ ratio is determined as $0.62 \pm 0.28(\text{stat.}) \pm 0.16(\text{sys.})$. This ratio is larger than those measured in the lower beam energies.

Motivated by partial success of collective expanding fireball model, which can explain both single particle spectra and HBT correlation but cannot describe low m_t region in pion spectra, different kinds of contributions are considered. Those are collective motion, the Coulomb effect, and contribution of Δ resonance. As the collective motion and the Coulomb effects are qualitatively smaller than the observed low m_t enhancement, the contribution of Δ resonance is therefore studied. Using the value of temperature and collective velocity, evaluated from single particle spectra and HBT measurement, about 1.5 times more contribution from Δ resonance than measured in the invariant mass is used to follow the shape of pion spectra. The factor is consistent with the results of a cascade simulation. The simulation tells the factor comes from such Δ resonance that decays into proton which is re-scattered and pion which is, however, not re-scattered after decay, and those Δ resonances are not measured in the invariant mass.

7. References

The notation in quotations is [Author(s)-YY], where Author(s) shows the author's name(s), and YY denotes the published year. For collaboration work, author name is referred as such. And plus sign (+) in author name indicate several authors.

- [A⁺-93] N. Angert et al. CERN Heavy-Ion Facility Design Report. *Yellow Report CERN 93-01* (1993).
- [A⁺-77] Aachen - Berlin - Bonn - CERN - Cracow - Heidelberg - Warsaw Collaboration, *Nucl. Phys.* B120 (1977) 14-22.
- [A^{FS}-84] T. Akesson et al. *Nucl. Phys.* B246 (1984) 1.
- [B⁺-96] A. Badala et al. *Phys. Rev.* C54 (1996) R2138.
- [B⁺-79] G. Battistoni et al., Proposal for an experiment on nucleon stability, Frascati - Milano - Torino (1979).
- [B^S-75] British - Scandinavian Collaboration, *Nucl. Phys.* B100 (1975) 237 - 290.
- [BSM-76] British-Scandinavian-MIT Collaboration, *Phys. Lett.* 64B (1976) 111-116.
- [B^O-96] J. -P. Blaizot and J. -Y. Ollitrault. J/ψ suppression in Pb+Pb collisions at $158 \times A$ GeV/c. *Phys. Rev. Lett.*, 77 (1996) 9.
- [B^{SW}-91] G. E. Brown, J. Stachel and G. M. Welke, *Phys. Lett.* B253 (1991) 19.
- [C⁺-75] J.W. Cronin, H. J. Frisch, M. J. Shochet, J. P. Boymond, P. A. Piroue, and R. L. Sumner, *Phys. Rev.* D11 (1975) 3105-3123.
- [C^r-78] N. S. Craigie, *Phys. Rep.* 47 (1978) 1-108.
- [C^{SH}-95] S. Chapman, P. Scotto, and U. Heinz, *Heavy Ion Physics* 1 (1995) 1.
- [E⁸⁰²-91] T. Abbot et al. (E802 collaboration), *Phys. Rev. Lett.* 66 (1991) 1567.
- [E⁸⁰²-96] L. Ahle et al. (E802 collaboration), *Nucl. Phys.* A610 (1991) 139c-152c.
- [E⁸¹⁴-95] E814 collaboration, *Phys. Lett. B* 351 (1995) 93-98.
- [F^e-76] E. L. Feinberg, *Nuovo Cimento*, 34A (1976) 39.
- [F^{OPL}-97] FOPI Collaboration, J. Barrette et al., *Phys. Lett.* B407 (1997) 115.
- [G^E-93] CERN Computing and Network Division, GEANT 3.1.5 Manual.
- [G^K-93] K. Geiger and J. I. Kapusta. Dilepton Radiation from Cascading Partons in Ultrarelativistic Nuclear Collisions. *Phys. Rev. Lett.*, 70 (1993) 13.
- [G^{KS}-87] C. Greiner, P. Koch and H. Stocker, *Phys. Rev. Lett.* 58 (1987)

- [GR-93] Edited by H. Gutbrod and J. Rafelski, "Particle Production in Highly Exited Matter", *NATO ASI Series B, Physics Vol. 303* (1993). For the particle formation time, see for example in page 34.
- [GRSK-88] C. Greiner, D. -K. Rischke, H. Stoecker and P. Koch, *Phys. Rev. D* 38 (1988) 2797.
- [G+-89] H. H. Gutbrod et al., *Rep. Prog. Phys.* 52(1989)1267.
- [H+-92] E.L. Hjort et al. *Phys. Rev. Lett.* E79(1997)4345.
- [H+-96] U. Heinz, B. Tomasik, U. A. Wiedemann, and Y. -F. Wu, *Phys. Lett.* B382 (1996) 181-188.
- [Ha-83] R. Hagedorn, *Riv. Nuovo Cimento* 6 (1983) 1
- [He-95] M. Mase for the HELIOS/3 collaboration. Dimuon Production below Mass $3.1 \text{ GeV}/c^2$ in p- W and S- W Interactions at $200 \text{ GeV}/c/A$. *Nucl. Phys. A* 590 (1995) 93c - 102c.
- [Hi-99] T. Hirano, *Master's Thesis*, (1999), *Univ. of Tsukuba*.
- [HT-54] R. Hanbury-Brown and R. Q. Twiss, *Phil. Mag.* 45 (1954) 633.
- [HL-92] T. Hatsuda and S. H. Lee, *Phys. Rev. C* 46 (1992) R24.
- [HK-85] T. Hatsuda and T. Kunihiro, *Phys. Rev. Lett.* 55 (1985) 158.
- [HK-92] T. Hatsuda and T. Kunihiro, *Nucl. Phys. A* 544 (1992) 27.
- [Iar-93] E. Iarocci, *Nucl. Inst. And Meth.* 217 (1993) 30 - 42.
- [Ka-99] M. Kaneta, Thermal and Chemical Freeze-out in Heavy Ion Collisions, *Ph. D thesis*, 1999Jan, *Hiroshima Univ.*
- [Ku-98] M. Kurata, Azimuthal Anisotropy of Particle Emission at Target Rapidity Region in Pb + Pb 158 A GeV Collisions, *Ph. D thesis*, 1998, *Univ. of Tsukuba*.
- [Mi-79] C. Michael, *Part. Nucl. Phys.* 2 (1979) 1
- [MS-86] T. Matsui and H. Satz. J/ ψ suppression by quark-gluon plasma formation. *Phys. Lett. B* 178 (1986) 4.
- [Mu-85] B. Mueller, "The Physics of the Quark-Gluon Plasma", Lecture Note in Physics 225, Springer-Verlag 1985.
- [MW-92] B. Mueller and X. Wang. Probing Parton Thermalization Time with Charm Production. *Phys. Rev. Lett.*, 69 (1992) 16.
- [LTKG-98] L. Carlen, K. El Chenawi, K. Enosawa, S. Garpman, H. -A. Gustafsson, M. Kurata, H. Lohner, M. Martin, Y. Miake, Y. Miyamoto, H. Naef, P. Nilsson, S. Nishimura, J. Nystrand, A. Oskarsson, L. Osterman, I. Otterlund, E. Perrin, L. Rosselet, J. M. Rubio, S. Sato, K. Soderstrom, N. Solomey, E. Stenlund, T. Svensson, S. Voros, K. Yagi, Y.

- Yokota (Lund Univ., Tsukuba Univ., KVI, Geneva Univ.).
 PERFORMANCE OF MULTI-STEP AVALANCHE CHAMBERS
 EQUIPPED WITH TWO-DIMENSIONAL ELECTRONIC READOUT.
Nucl. Instr. and Meth., A 412 (1998) 361-373.
- [N¹-98] Y. Nara, "JAM 1.009: A microscopic simulation program for ultra-relativistic nuclear collisions" at <http://hadron31.tokai.jaeri.go.jp/jam.html>.
- [N²-98] Y. Nara, Microscopic Simulation for Strangeness Nuclear Physics at <http://hadron31.tokai.jaeri.go.jp/~ynara/>.
- [N³⁵-90] NA35 collaboration, *Z. Phys.* C48 (1990) 191.
- [N⁴⁴-96] NA 44 collaboration, *Nucl. Phys.* A610(1996)175c-187c. For Fig. 48, results from model calculations are clearly shown.
- [N⁴⁵-99] NA45/CERES Collaboration, *Nucl. Phys.* A661(1999)23.
- [N⁵⁰-97] NA50 collaboration, *Phys. Lett.* B410 (1997) 337.
- [N⁴⁹-98] NA49 collaboration, *Eur. Phys. J.* C2 (1998) 661-670.
- [N⁴⁹-99] NA49 collaboration, *Nucl. Phys.* A661 (1999) 45c-54c.
- [P^e-97] T. Peitzmann, Kernmaterie unter extremen Bedingungen - Die experimentelle Suche nach dem Quark-Gluon-Plasma - (in German), *Habilitationsschrift*, 1997 Nov., *Muenster Univ.* For Fig. 10, only WA98 results are shown.
- [R^M-82] J. Rafelski and B. Muller, *Phys. Rev. Lett.* 48 (1982) 1066.
- [R^M-86] J. Rafelski and B. Muller, *Phys. Rev. Lett.* 56 (1986) 2234.
- [R^u-91] P. V. Ruuskanen, *Nucl. Phys.* A525 (1991) 255c - 268c.
- [R^u-92] P. V. Ruuskanen, *Nucl. Phys.* A544 (1992) 169c - 182c.
- [R^u-98] J. M. Rubio, Transverse Flow from m_T Spectra in Pb + Pb Collisions at 158 GeV/c per Nucleon, *Ph.D. thesis*, 1998 Jan, *Univ. of Geneve No 2974*.
- [S^a-95] S. Sato, Production of High Resolution Time of Flight System for High Energy Heavy Ion Experiments (BNL-RHIC-PHENIX & CERN-SPS-WA98) *Master's thesis*, 1995 Feb., *Univ. of Tsukuba*.
- [S^c-98] H. Schlagheck, *Ph.D. thesis* (1998) *Muenster University*.
- [S^h-78] E. Shuryak, *Phys. Lett.* 78B (1978) 150.
- [S^t-98] P. A. Steinberg, Search for Disoriented Chiral Condensates in 158 A GeV 208Pb + Pb Collisions, *Ph.D. thesis*, 1998 Feb., *Massachusetts Institute of Technology, U.S.A.*
- [S^{SX}-98] B. R. Schlei, D. Strottman, N. Xu. *Phys. Rev. Lett.* 80 (1998) 3467, or

nucl-th/9710047, 1997/Oct/20. For Fig. 8 and Fig. 46, arbitrarily of the yield each other among pion, kaon, and proton is shown clearly.

- [T^a-85] Y. A. Tarasov, *Sov. J. Nucl. Phys.* 42 (1985) 260
- [T^C-94] M. Kurata, S. Kato, A. Kumagai, K. Kurita, Y. Miake, S. Sato, K. Tomizawa, S. Ueno-Hayashi, K. Yagi, S. Nagamiya, T.K. Nayak, O. Vossnack, X. Yang, W.L. Zhan (Tsukuba U. & Nevis Labs, Columbia U.). STUDY OF TIMING DEGRADATION AND LIGHT ATTENUATION IN LONG PLASTIC SCINTILLATION RODS FOR TIME-OF-FLIGHT COUNTERS IN RELATIVISTIC HEAVY ION EXPERIMENTS. *Nucl. Instr. Meth. A* 349 (1994) 447-453.
- [T^{su}-96] T. Chujo, K. Enosawa, R. Higuchi, K. Kanoh, M. Kurata, K. Kurita, Y. Miake, Y. Miyamoto, S. Nishimura, Y. Okuma, S. Sato, Y. Yokota, K. Yagi (Tsukuba Univ.). A GAS CHERENKOV BEAM COUNTER WITH A TIMING RESOLUTION OF 30 PS FOR RELATIVISTIC HEAVY ION EXPERIMENTS. *Nucl. Instr. and Meth.*, A383 (1996) 109-112.
- [W⁺-98] Wu Y. -F., U. Heinz, B. Tomasik, and U. A. Wiedemann, *Eur. Phys. J. C*1 (1998) 599-617, or *nucl-th / 9607044* (Jun/11/1997).
- [W⁸⁵-91] WA85 Collaboration, *Phys. Lett.* B259 (1991) 508.
- [W⁸⁵-95] WA85 Collaboration, *Nucl. Phys.* A590 (1995) 307c-316c.
- [W⁹⁴-95] WA94 Collaboration, *Nucl. Phys.* A590 (1995) 317c-332c.
- [W⁸⁰-94] R. Santo et al (WA80 Collaboration). Single Photon and Neutral Meson Data from WA80. *Nucl. Phys.* A566 (1994) 61c-68c.
- [W⁸⁰-95] T. Awes et al (WA80 Collaboration). Search for direct photon production in 200 A GeV S + Au reactions: a status report. *Nucl. Phys.* A, 590 (1995) 81c-92c.
- [W⁹⁸-91] A. L. Angelis et al. Proposal for a Large Acceptance Hadron and Photon Spectrometer. *CERN/SPSLC* 91-17, SPSLC/P260 (1991).
- [W⁹⁸-98] WA98 collaboration, *Nucl. Phys.* A638 (1998) pp. 385-388, 459-462, 147-158.
- [W⁹⁸-99] WA98 collaboration, Elliptic Flow of Kaons and Pions in 158 A GeV Pb + Pb collisions, *Phys. Lett.* B469 (1999) 30-36.

Appendix A: Relativistic Heavy Ion Accelerators

To create and study states of matter at extremely high temperature and high density, relativistic heavy ion accelerator is operated at a few or more GeV per nucleon in their center of mass energy. Tab. A-1 shows the current status of the relativistic heavy ion accelerators.

Accelerator	Laboratory	Accelerated Nuclear		First Operation
		Nuclear	$s^{1/2}(\text{A GeV})$	
AGS	BNL	$^{16}\text{O}, ^{28}\text{Si}$	5.4	1986
		^{197}Au	4.8	1992
SPS	CERN	$^{16}\text{O}, ^{32}\text{S}$	19.4	1986
		^{208}Pb	17.4	1994
RHIC	BNL	^{197}Au	130	2000

Tab A-1: Current status of relativistic heavy ion accelerators.

Appendix B: Examples of Calculation

(1) Angular Momentum

To see applicability of the impact parameter, an example of angular momentum calculation is shown for 158 A GeV Pb + Pb collisions in the center of mass frame.

Assuming impact parameter, b , is the radius of the lead nuclei, r_{Pb} ,

$$\begin{aligned} b & \stackrel{assumed}{=} r_{Pb} \\ & \sim 1.2 \cdot A^{1/3} (fm), \\ & \sim 7.1 (fm) \end{aligned}$$

and incident beam momentum, p_{in} , is 8.6 GeV/c (which is equivalent to $E_{in} = 8.7 \text{ GeV} = s_{SPS}^{1/2} / 2$),

$$\begin{aligned} p & \stackrel{assumed}{=} \sqrt{\left(\frac{\sqrt{s_{SPS}}}{2} \right)^2 - (m_N)^2} \\ & \sim 8.6 \text{ GeV} / c, \end{aligned}$$

angular momentum around the center of mass, $|l_{c.m.}|$ defined as (twice of) a product of $b/2$ and p is calculated as follows.

$$\begin{aligned} |l_{c.m.}| & \stackrel{assumed}{=} 2 \cdot \left| \frac{b}{2} \cdot p \right| \\ & \sim 60 \text{ GeV} \cdot \text{fm} / c. \end{aligned}$$

The angular momentum, $|l_{c.m.}|$, is much larger than the typical scale of quantum effects, $\hbar \sim 0.2 \text{ GeV} \cdot \text{fm} / c$.

$$|l_{c.m.}| (\sim 60 \text{ GeV} \cdot \text{fm} / c) \gg \hbar (\sim 0.2 \text{ GeV} \cdot \text{fm} / c)$$

Consequently, the classical parameter such as impact parameter, b , is applicable.

(2) Nucleon - Nucleon Collisions as Primary Processes

To see the applicability of picture where primary process of relativistic heavy ion collision (nucleus - nucleus collision) is nucleus - nucleus collisions, an example of calculations is shown for length comparison between de Broglie wavelength of incident beam and nuclear size. The example is for

158 A GeV Pb + Pb collisions in center of mass frame.

The de Broglie wavelength, λ_{dB} , of incident nuclei is

$$\begin{aligned} \lambda_{dB} &\equiv \frac{\hbar c}{p} \\ &\sim 0.9 \text{ fm} . \end{aligned}$$

And the size of lead nuclei, $2r_{Pb}$, where r is the radius, is

$$\begin{aligned} 2 \cdot r_{Pb} &\sim 2 \cdot (1.2 \cdot A^{1/3}) \text{ (fm)} \\ &\sim 14 \text{ (fm)} . \end{aligned}$$

The de Broglie wavelength is short enough than the size of the nucleus.

$$\lambda_{dB} \ll 2 \cdot r_{Pb} .$$

Consequently, collision unit is constituent nuclei, but not nucleus as a whole.

(3) Distinction between Participant Region and Spectator Region

To see the reasonability of distinction between participant region and spectator region, an example of calculation is shown for time comparison between transverse direction and parallel direction with respect to the incident beam.

The collision time, Dt_{col} , is in the order of 1 fm/c due to the Lorentz contract. Note also that corresponding number of nucleons in the diameter direction is about 4, and the collision time is for those plural nucleons.

The traversing time, Dt_T , for the nucleon with average transverse momentum ($\sim 250 \text{ MeV}/c$, $b \sim 0.25$) to reach nucleon located in the next ($\sim 1.7 \text{ fm}$) perpendicular to incident momentum is about 7 fm/c.

The average transverse momentum after a nucleon - nucleon collision is smaller enough than longitudinal momentum to have following collisions dominantly in tubular region in the same direction of incident momentum.

$$Dt_{col} \ll Dt_T$$

Consequently, geometrical distinction of participant region and spectator region is applicable.

Appendix C: Parameters Used in Relativistic Kinematics

At high energy physics, kinetic parameters are chosen as, from the Lorentz transformation,

$$\begin{aligned}E &= \gamma m \\ p &= \gamma m \mathbf{b} \\ m^2 &= E^2 - p^2 \\ (\gamma &= \text{energy} / \text{mass}, \beta = \text{momentum} / \text{energy}).\end{aligned}$$

where m is the mass of the particle, E is the total energy, p is the momentum.

Transverse momentum, p_t , is the transverse component of p , and it is Lorentz invariant.

The *rapidity*, y , is defined as,

$$y = \frac{1}{2} \ln \left\{ \frac{E + p_{\parallel}}{E - p_{\parallel}} \right\}$$

In the case of non-relativistic limits ($E \gg p > p_{\parallel}$),

$$\begin{aligned}y &= \frac{1}{2} \ln \left\{ \frac{E + p_{\parallel}}{E - p_{\parallel}} \right\} \\ &= \frac{1}{2} \ln \left\{ \frac{1 + \mathbf{b}}{1 - \mathbf{b}} \right\} \\ &\sim \mathbf{b}.\end{aligned}$$

In the case of relativistic limits ($E \sim p$),

$$\begin{aligned}y &= \frac{1}{2} \ln \left\{ \frac{E + p_{\parallel}}{E - p_{\parallel}} \right\} \\ &\sim \frac{1}{2} \ln \left\{ \frac{p + p_{\parallel}}{p - p_{\parallel}} \right\} \\ &= \frac{1}{2} \ln \left\{ \frac{p + p \cos \theta}{p - p \cos \theta} \right\} \\ &= - \ln \left\{ \tan(\theta/2) \right\}\end{aligned}$$

Generally, $- \ln \left\{ \tan(\theta/2) \right\}$ is called *pseudo rapidity*, \mathbf{h} .

Appendix D: WA98 Experiment Coordinate System

In the coordinate where origin is center of magnet, and horizontal (positive in left side), vertical (positive in upward), and beam (positive in down stream) directions are X_B , Y_B , and Z_B , respectively, as shown in Fig. D-1, the Arm-II is located in positive X_B and the Arm-I is in negative X_B .

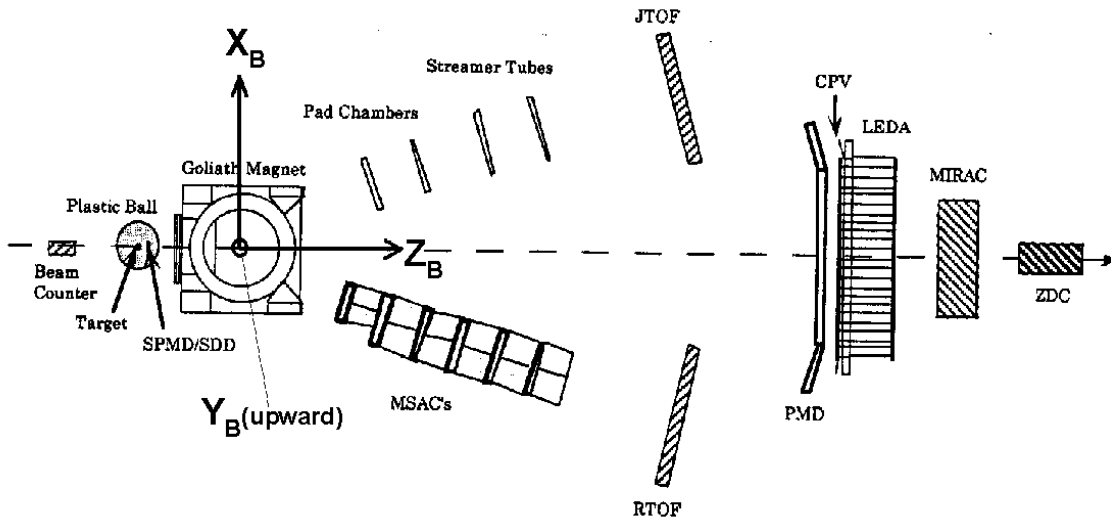


Figure D-1: WA98 coordinate system.

The position and the tilted angle with respect to the beam axis (Z_B) of the start counter, the target, the magnet and the tracking detectors are summarized in Tab. D-1.

Arm	Detector	Position (the center for ARM-II, and the inner edge for ARM-I)		Tilted angle from X_B axis (degree)
		X_B (mm)	Z_B (mm)	
	Start counter	0	-6,680	0
	Target	0	-3,280	0
	Center of Magnet	0	0	0
ARM-II	PAD-1	+1,233	+3,850	+14.6
	PAD-2	+1,396	+4,811	+14.6
	STD-1	+1,637	+6,311	+8.6
	STD-2	+1,995	+7,811	+8.6
	JTOF	+3,595	+14,120	+14.6
ARM-I	MSAC-1	-1,156	+3,175	-19
	MSAC-2	-1,504	+4,130	-19
	MSAC-3	-1,938	+5,322	-19
	MSAC-4	-2,372	+6,513	-19

<i>ARM-I</i>	<i>MSAC-5</i>	<i>-2,805</i>	<i>+7,705</i>	<i>-19</i>
	<i>MSAC-6</i>	<i>-3,239</i>	<i>+8,896</i>	<i>-19</i>
	<i>RTOF</i>	<i>-3,892</i>	<i>+13,039</i>	<i>-19</i>

Tab. D-1: Position of each detectors in WA98 magnetic spectrometers in (X_B , Z_B) coordinate (refer Fig. D -1).

Appendix E: Other Detectors in WA98

We have other detectors in WA98 to measure simultaneous signals for the characterization of heavy ion collisions.

(1) Multi Step Avalanche Chamber: MSAC

In the Arm-I, there are 6 planes of multi step avalanche chambers have active area. First plane is a size of $1.2 \times 0.8 \text{ m}^2$ and the other five is sizes of $1.6 \times 1.2 \text{ m}^2$ (called "small chamber" and "big chamber", hereafter) respectively.

The chambers are filled with Ne and Ar based mixture with Triethylamine (TEA). As schematically shown in Fig. E-1, (the gap size and the applied HV value are shown in Fig. E-2) position detection of charged particles is done in following steps [R^u-98].

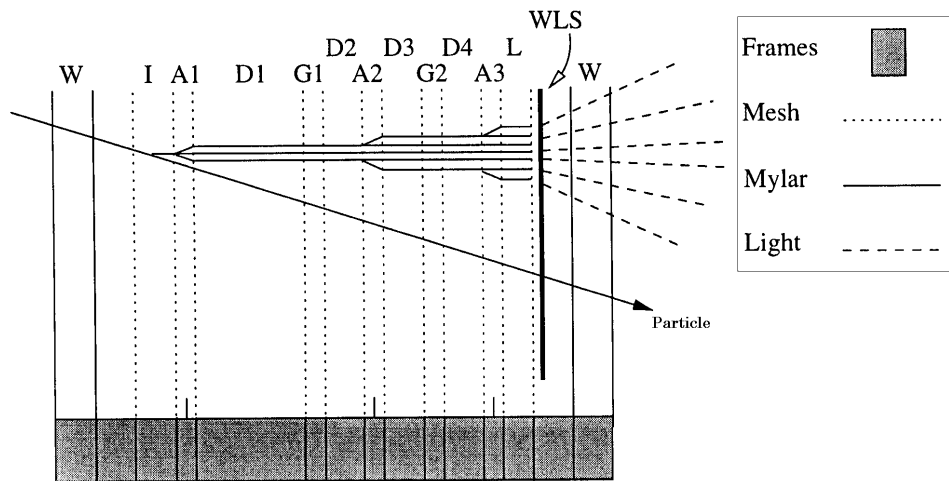


Fig. E-1: Schematic cross section of MSAC. W: double window with a flow of pure Argon, I: ionization gap, A: amplification gaps, D: drift gaps, G: gate gaps, L: light gap, WLS: wavelength shifter.

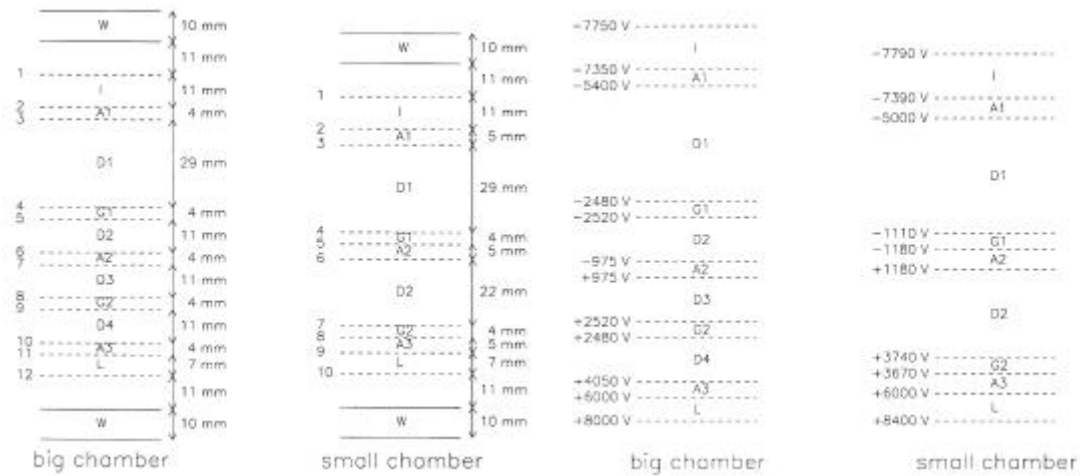


Fig. E-2: (Left) Gap size in the MSACs. (Right) Voltage setting for the MSAC.

The primary ionization is performed in the 11 mm long ionization gap (I). The emitted electrons are directed with a low electric field to the first 4 mm long amplification gap (A1). At the gap (A1), a strong electric generates an avalanche. The avalanche enters a 29 mm long drift gap (D1), which provide time for the trigger decision. Next the electron cloud enters the first gate gap (G1) where reversed electric field is applied except when a trigger comes. A 450 V pulse with 1 μ s width is used for electrons to pass through and to reach the second 4 mm (for big chamber; for small chamber, 5 mm) long amplification gap (A2). The second gate gap is opened 1400 ns after the first gate (G1) has been opened. Then the electrons traverse the last high electric field of amplification gap (A3). Finally the electrons enter the 7mm long light production gap (L) where a lower electric field favors the excitation of the light emitting TEA molecules. In order to match the spectral sensitivity of the cameras, a Wave Length Shifter (WLS) plate is mounted after the light production gap (L).

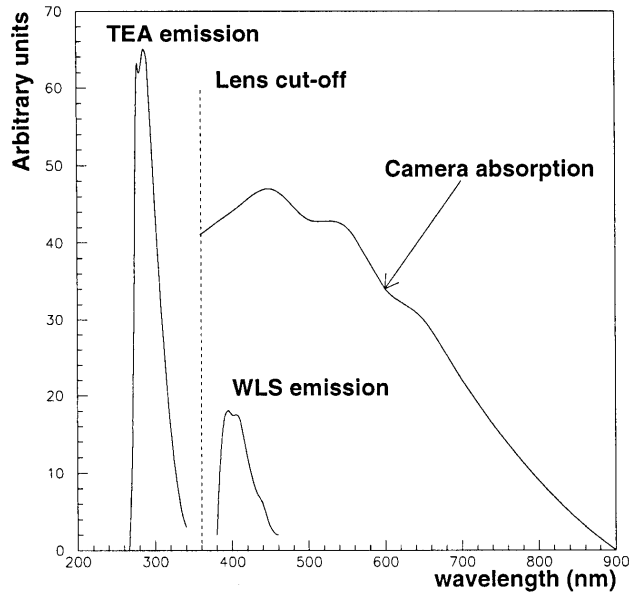


Fig. E-3: Emission spectra for the TEA and the Wave Length Shifter (WLS), and a bsorption spectra for the CCD camera. The spectra are n ot normalized with respect to the others.

The wavelength shifter absorbs 280 nm light emitted by TEA and emit 400 nm light as shown in Fig. E-3. The total number of produced photons are measured to be around 5×10^7 to 5×10^8 .

(2) Time of Flight Detector (in Arm-I): TOF_{Arm-I}

Time Of Flight detector in Arm-I (TOF_{Arm-I}) is made of 480 (120 in width, and 4 in height) plastic scintillators (similar to NE110 plastic), which results in an active area of 398 mm in width and 1920 mm in height. The sizes of each scintillator are 32 mm in width, 480 mm in height, and 24 mm in depth. On the both edge of scintillator, a photomultiplier (PMT) XP2972 is directly coupled via optical grease. Each analog signal from the last dynode of PMT is, in time wise, discriminated by a leading edge discriminators and is carried in 108 m to the counting house. The logical signal starts a overlap coincidence unit, and the trigger timing is used for the stop of the overlap unit. The integrated charge as an output of the overlap unit is digitized by ADC (LeCroy, LRS2280) with the conversion parameter of 20 ps/channel, and typical time of flight resolution is about 100ps as shown in Fig. E-4.

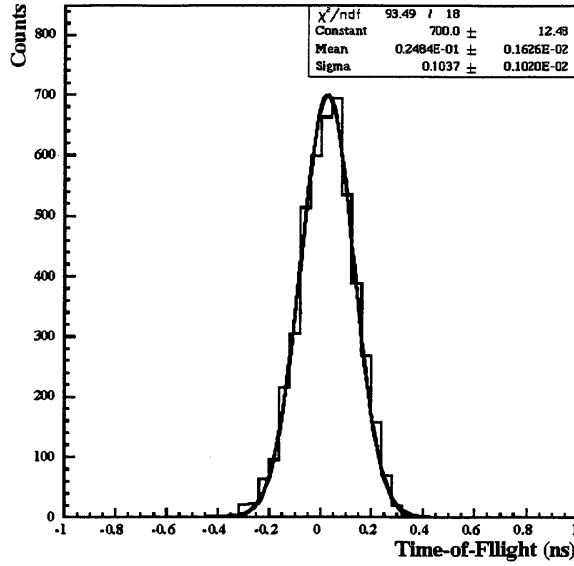


Fig. E-4: RTOF resolution ($T_{OF} = 103 \pm 1$ ps).

(3) Lead Glass Calorimeter: LEDA

For the photon measurements in region of $2 < \theta < 3$, an electromagnetic calorimeter LEad glass Detector Array (LEDA) is installed 21.5m downstream of from target. The LEDA consists of 10,000 lead-glass modules, and each module is made from a lead-glass block sized 40 mm (width) \times 40 mm (height) \times 400 mm (depth) with PMT readout. The measured energy resolution by 10 GeV electron beam is [P^e-97]

$$\frac{\sigma(E)}{E} = \frac{(5.5 \pm 0.6)\%}{\sqrt{E/GeV}} + (0.8 \pm 0.2)\% .$$

(4) Plastic Ball

For the charged particles around target fragmentation region ($-1.7 < \theta < 0.5$, or $160^\circ < \theta < 30^\circ$) in full azimuthal are measured by the plastic ball detector [G⁺-89]. The plastic ball consists of 665 E-E modules, as schematically shown in Fig. E-5.

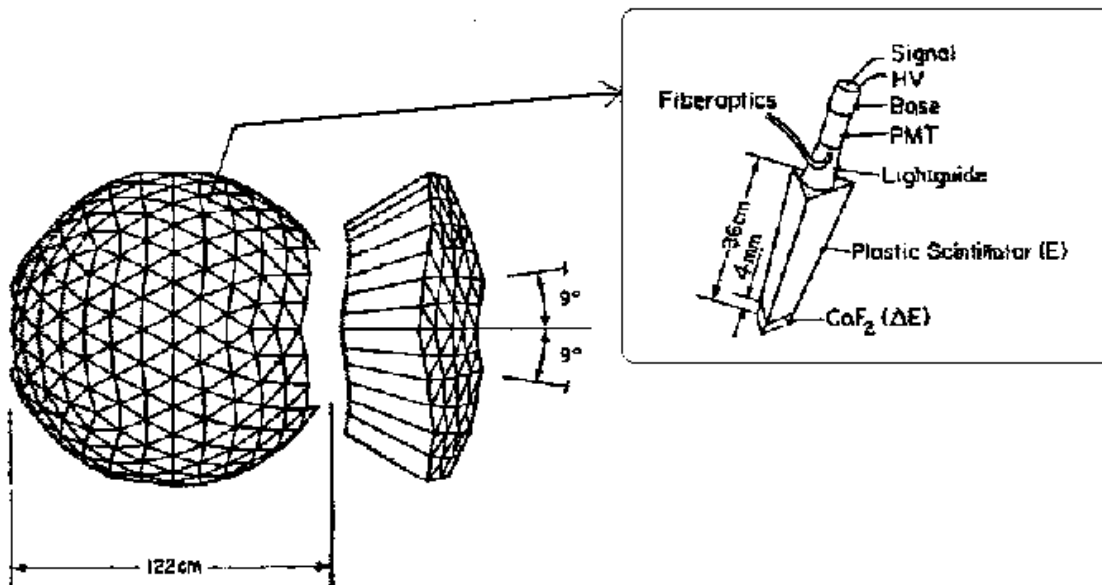


Fig. E-5: Schematic view of the Plastic Ball detector.

Each module has a 4mm-depth $\text{CaF}_2(\text{Eu})$ crystal as ΔE counter, and a 356 mm-depth plastic scintillator as E counter. E-E measurement allows identification of charged pions, protons, and heavier fragments (deuterons, tritons, ^3He). Protons up to 240 MeV are stopped in the plastic E counter. Positively charged pion are measured and identified in the energy window of $11 < E_{\pi^+} < 110$ MeV via a coincidence tag from their delayed decay $\pi^+ \rightarrow \mu^+ + \nu_{\mu}$ in the plastic E counter in addition to E-E measurement. In condition of high particle densities the plastic ball can resolve single particles nominally in the region of $-0.7 < \eta < 0.1$. The plastic ball is useful for reaction plane determination [Ku-98, W⁹⁸⁻⁹⁹].

(5) Silicon Pad Multiplicity Detector: SPMD

For the charged particle passing in $2.35 < \eta < 3.75$, a circular pad detector named SPMD (Silicon Pad Multiplicity Detector) is used [St-98]. The detector is a $300 \mu\text{m}$ n-type wafer implanted with p^+ pads to create p-n junction. To fully deplete the silicon, 50V is applied across the junction. When a charged particle traverse the silicon wafer, the energy loss invoke electron-hole pairs (most probable value for energy loss is about 84 keV which corresponds 24,000 electron-hole pairs). The liberated charge induces a signal on aluminum pads, which is separated from p^+ pads by dielectric. The readout is done using the IDE VA-1 chip, which has a 128-channel

charge sensitive amplifier and storage capacities.

(6) Photon Multiplicity Detector: PMD

At mid rapidity ($2.4 < \eta < 4.4$), photon multiplicity is measured by a large photon multiplicity detector called PMD (Photon Multiplicity Detector). The PMD consists of $3X_0$ -depth lead converter sheets and 53200 pads of 3 mm-depth scintillator. The scintillator pads are sized in four manners from 15(width) \times 15(height) mm² to 25(width) \times 15(height) mm², and arranged in 28 modules. Each module contains 1900 scintillator pads and coupled with a CCD camera through wavelength shifting fibers and clear fibers (each pad is covered by one wavelength shifting fiber followed by one clear fiber). Each camera consists of a 3 stage electrostatic image intensifier, a multi channel plate and a Charge Coupled Device (CCD) with 31600 pixels. The total light amplification is 4×10^4 . Photon detection efficiency is about 80% for photons with energy greater than 0.4 GeV, and the hadron contamination is estimated to be about 20%.

Appendix F: Selection of Radiator of Start Counter for Heavy Ion Beam

In advance of physics run, best radiator is investigated among following three materials. (1) Nitrogen gas in $p = 1$ atm. ($n = 1.000297$) and in 75 mm of thickness (0.5 % interaction length) is for Cherenkov light radiator (named RAD-1). (2) Quartz in 0.2 mm of thickness (0.5 % interaction length) is also for Cherenkov light radiator (RAD-2). And (3) plastic scintillator in 0.5 mm of thickness (0.6 % interaction length) is for scintillation light radiator (RAD-3).

Name	<i>RAD-1 (used for heavy ion beam)</i>	<i>RAD-2</i>	<i>RAD-3</i>
Type	gas Cherenkov counter	Plastic scintillation counter	quartz Cherenkov counter
Description (n: refractive index)	N ₂ gas, 1 atm., (n= 1.000297)	scintillator: BICRON BC404	n = 1.45
Thickness	up: 3.0 cm, down: 4.5cm	0.5 mm	0.2 mm
Interaction rate	0.5%	0.6%	0.5 %
PMT	Up: H5321 -MOD down: H2431-02T	H2431 (glass window)	H2431-02T
Timing resolution	30 ps	48-135 ps	55 ps
Charge resolution (Z/Z)	2.0%	> 5%	2.6%
Deterioration of PMT output (*)	9%	17%	18%

(*) (Decrease of the PMT output during the exposure to 1.5×10^9 lead ions)

Tab. F -1: Selection of radiator for heavy ion beam.

Tab. F-1 shows the summary of the results. After injection of 1.5×10^9 lead ions, RAD-1 has the least deterioration in PMT outputs (9 %, 18% and 17%, for RAD-1, 2, and 3, respectively; most of deterioration for RAD-1 is caused by degradation of PMT itself because of its operation at the maximum dynode currents; for RAD-2 and 3, additional radiation damages are contributing). We conclude, therefore, RAD-1 is the best radiator.

Acknowledgements

I appreciate Prof. Dr. Y. Miake for providing me chances to make researches in this field of physics and showing me importance of steady attitude for research. I thank Prof. Dr. K. Yagi for showing importance to have both experimental and theoretical skill and understanding. I owe my experiences in WA98 experiment to Prof. Dr. H. Gutbrod. By his strong attitude for taking experimental data to get profound understanding, I realize interests of experimental physics.

To Dr. T. Awes I thank very much for his direction as a devoted spokesperson of WA98 collaboration. I should show my regards to Dr. S. Nishimura for his hundreds of daily advices depending on my achievements. I owe lots to Dr. K. Kurita for the basic attitudes for the young scientist. From Dr. H. Gustafson, I learned how experiments need patience and steady efforts, and I would like to appreciate him very much for the strong direction for the new Arm-II spectrometer. Owing to Prof. Dr. R. Santo and Prof. Dr. H. Lohner, I could experience a new experimental apparatus, namely STD tracking detector, with responsible attitude. With very experienced guide by Dr. B. Kolb, I experienced stable and robust software structure both in DAQ and control of experiment. Also I cannot forget his fair attitudes to defend for un-attending persons. I appreciate Dr. M. Purschke for spending lots of time to persuade me things and encourage almost every day. To Dr. T. Peitzmann I thank for showing faithful attitudes in discussion. I need to show my deep regards to Prof. Dr. S. Nagamiya to assist and guide our collaboration from far institute. I feel lots from Dr. C. Chi for careful attitudes in any kinds of situations.

I should show many thanks to Dr. M. Kurata, Dr. K. Chenawi, Dr. S. Garpman, Dr. K. Enosawa, Mr. Y. Yokota, Ms. Y. Miyamoto, Dr. T. Chujo, Dr. H. Sako, Mr. S. Kato, Ms. M. Aizawa, Mr. D. Hakozaki, Dr. Y. Nara, Mr. T. Hirano, Mr. H. Hayashi and Ms. M. Hirose for encouragements and for spending time with me at Tsukuba and at CERN.

I cannot proceed with this thesis without experienced support by Mr. H. Cunitz, Mr. Y. Au, Mr. N. Heine, Mr. H. Wolfgang, and technicians at NEVIS laboratory and CERN laboratory. Especially to Mr. A. Przybyla I deeply say thank-you for continuous encouragements. I like here to show my appreciations to collaborators of WA98 experiment.

I'm always happy with memories with my grand parents, Take Yamakawa, Kaneko Sato, and cap. Yasuhiko Sato, who keep me doing things by myself from very early childhood. I thank my elder brother, Kazuhiko Sato, who keeps me away from stubborn attitude to things, and my younger sister, Natsuko Sato-Fukunishi, who shows me an importance of smiling continuously. I cannot complete this work without steady trusts from my father, Tadashi Sato, and dedicated encouragements from my mother, Satoko Sato.

PUBLISHED PAPER

" Δ^{++} production in 158 A GeV $^{208}\text{Pb} + ^{208}\text{Pb}$ interactions at the CERN SPS "
(Physics Letters B 477 (2000) 37 - 44)



ELSEVIER

23 March 2000

PHYSICS LETTERS B

Physics Letters B 477 (2000) 37–44

Δ^{++} production in 158 A GeV $^{208}\text{Pb} + ^{208}\text{Pb}$ interactions at the CERN SPS

WA98 Collaboration

M.M. Aggarwal ^a, A. Agnihotri ^b, Z. Ahammed ^c, A.L.S. Angelis ^d, V. Antonenko ^e,
V. Arefiev ^f, V. Astakhov ^f, V. Avdeitchikov ^f, T.C. Awes ^g, P.V.K.S. Baba ^h,
S.K. Badyal ^h, A. Baldine ^f, L. Barabach ^f, C. Barlag ⁱ, S. Bathe ⁱ, B. Batiounia ^f,
T. Bernier ^j, K.B. Bhalla ^b, V.S. Bhatia ^a, C. Blume ⁱ, R. Bock ^k, E.-M. Bohne ⁱ,
Z. Böröcz ⁱ, D. Bucher ⁱ, A. Buijs ^l, H. Büsching ⁱ, L. Carlen ^m, V. Chalyshev ^f,
S. Chattopadhyay ^c, R. Cherbatchev ^e, T. Chujo ⁿ, A. Claussen ⁱ, A.C. Das ^c,
M.P. Decowski ^r, H. Delagrange ^j, V. Djordjadze ^f, P. Donni ^d, I. Doubovik ^e,
S. Dutt ^h, M.R. Dutta Majumdar ^c, K. El Chenawi ^m, S. Eliseev ^o, K. Enosawa ⁿ,
P. Foka ^d, S. Fokin ^e, V. Frolov ^f, M.S. Ganti ^c, S. Garpman ^m, O. Gavrishchuk ^f,
F.J.M. Geurts ^l, T.K. Ghosh ^p, R. Glasow ⁱ, S.K. Gupta ^b, B. Guskov ^f,
H.Å. Gustafsson ^m, H.H. Gutbrod ^j, R. Higuchi ⁿ, I. Hrivnacova ^o, M. Ippolitov ^e,
H. Kalechofsky ^d, R. Kamermans ^l, K.-H. Kampert ⁱ, K. Karadjev ^e, K. Karpio ^q,
S. Kato ⁿ, S. Kees ⁱ, B.W. Kolb ^k, I. Kosarev ^f, I. Koutcheryaev ^e, T. Krümpel ⁱ,
A. Kugler ^o, P. Kulinich ^r, M. Kurata ⁿ, K. Kurita ⁿ, N. Kuzmin ^f, I. Langbein ^k,
A. Lebedev ^e, Y.Y. Lee ^k, H. Löhner ^p, L. Luquin ^j, D.P. Mahapatra ^s, V. Manko ^e,
M. Martin ^d, G. Martínez ^j, A. Maximov ^f, R. Mehdiyev ^f, G. Mgebrichvili ^e,
Y. Miake ⁿ, D. Mikhalev ^f, Md.F. Mir ^h, G.C. Mishra ^s, Y. Miyamoto ⁿ,
B. Mohanty ^s, D. Morrison ^t, D.S. Mukhopadhyay ^c, V. Myalkovski ^f, H. Naef ^d,
B.K. Nandi ^s, S.K. Nayak ^j, T.K. Nayak ^c, S. Neumaier ^k, A. Nianine ^e,
V. Nikitine ^f, S. Nikolaev ^e, P. Nilsson ^m, S. Nishimura ⁿ, P. Nomokonov ^f,
J. Nystrand ^m, F.E. Obenshain ^t, A. Oskarsson ^m, I. Otterlund ^m, M. Pacher ^o,
A. Parfenov ^f, S. Pavliouk ^f, T. Peitzmann ⁱ, V. Petracek ^o, F. Plasil ^g,
W. Pinganaud ^j, M.L. Purschke ^k, J. Rak ^o, R. Raniwala ^b,
S. Raniwala ^b, V.S. Ramamurthy ^s, N.K. Rao ^h, F. Retiere ^j, K. Reygers ⁱ,
G. Roland ^r, L. Rosselet ^d, I. Roufanov ^f, C. Roy ^j, J.M. Rubio ^d,
H. Sako ⁿ, S.S. Sambyal ^h, R. Santo ⁱ, S. Sato ⁿ, H. Schlagheck ⁱ,
H.-R. Schmidt ^k, Y. Schutz ^j, G. Shabratova ^f, T.H. Shah ^h,

I. Sibiriyak^e, T. Siemiarczuk^q, D. Silvermyr^{m,1}, B.C. Sinha^c,
 N. Slavine^f, K. Söderström^m, N. Solomey^d, S.P. Sørensen^{g,t},
 P. Stankus^g, G. Stefanek^q, P. Steinberg^r, E. Stenlund^m, D. Stückenⁱ,
 M. Sumbera^o, T. Svensson^m, M.D. Trivedi^c, A. Tsvetkov^e,
 L. Tykarski^q, J. Urbahn^k, E.C. van der Pijll^l, N. van Eijndhoven^l,
 G.J. van Nieuwenhuizen^r, A. Vinogradov^e, Y.P. Viyogi^c,
 A. Vodopianov^f, S. Vörös^d, B. Wysłouch^r, K. Yagiⁿ,
 Y. Yokotaⁿ, G.R. Young^g

^a University of Panjab, Chandigarh 160014, India

^b University of Rajasthan, Jaipur 302004, Rajasthan, India

^c Variable Energy Cyclotron Centre, Calcutta 700 064, India

^d University of Geneva, CH-1211 Geneva 4, Switzerland

^e RRC “Kurchatov Institute”, RU-123182 Moscow, Russia

^f Joint Institute for Nuclear Research, RU-141980 Dubna, Russia

^g Oak Ridge National Laboratory, Oak Ridge, Tennessee 37831-6372, USA

^h University of Jammu, Jammu 180001, India

ⁱ University of Münster, D-48149 Münster, Germany

^j SUBATECH, Ecole des Mines, Nantes, France

^k Gesellschaft für Schwerionenforschung (GSI), D-64220 Darmstadt, Germany

^l Universiteit Utrecht / NIKHEF, NL-3508 TA Utrecht, The Netherlands

^m Lund University, SE-221 00 Lund, Sweden

ⁿ University of Tsukuba, Ibaraki 305, Japan

^o Nuclear Physics Institute, CZ-250 68 Rez, Czech Republic

^p KVI, University of Groningen, NL-9747 AA Groningen, The Netherlands

^q Institute for Nuclear Studies, 00-681 Warsaw, Poland

^r MIT Cambridge, MA 02139, USA

^s Institute of Physics, 751-005 Bhubaneswar, India

^t University of Tennessee, Knoxville, TN 37966, USA

Received 18 January 2000; received in revised form 11 February 2000; accepted 11 February 2000

Editor: L. Montanet

Abstract

The Δ^{++} -resonance production in central 158 A GeV $^{208}\text{Pb} + ^{208}\text{Pb}$ collisions at the CERN SPS has been studied. The Δ^{++} production was estimated from the invariant mass spectrum of $p\pi^+$ -pairs by subtracting a mixed event background. The measured Δ^{++} abundance is compared with the results from other experiments at lower energies, and with a model calculation assuming thermal and chemical equilibrium. © 2000 Elsevier Science B.V. All rights reserved.

PACS: 25.75.Dw

Keywords: Ultra-relativistic heavy ion collisions; Δ^{++} resonance production; Mixed event technique; Freeze-out temperature

Energetic heavy ion collisions provide the means for studies of nuclear matter under extreme condi-

tions in the laboratory. The copious interactions between pions and nucleons in the final state of ultra-relativistic heavy ion collisions make the determination of the $\Delta(1232)$ abundance an interesting probe of the thermal conditions during the collision.

¹ E-mail: david.silvermyr@kosufy.lu.se

The Δ -resonance, apart from playing a role in particle production and interaction dynamics, may probe the conditions in heavy-ion collisions at early freeze-out times and high freeze-out densities [1]. It has been suggested that a chemical freeze-out temperature can be extracted from the $\Delta(1232)$ /nucleon ratio [2]. The Δ -resonance is known to be readily produced in photon [3]- lepton [4]- and hadron [5]-induced nuclear interactions and the cross sections for production of Δ -resonances in elementary nucleon-nucleon collisions are large [6].

Recently, results on $\Delta(1232)$ production in nucleus-nucleus collisions at 95 A MeV [7], at 1 and 2 A GeV [8] and at 13.7 A GeV [9] have been reported. In this paper we present measurements on the production of Δ^{++} by means of an invariant mass analysis of $p\pi^+$ -pairs in 158 A GeV central $^{208}\text{Pb} + ^{208}\text{Pb}$ central collisions at the CERN SPS. The measurement utilizes the new high resolution tracking arm of WA98 [10], which consists of multi-step avalanche chambers, streamer tube detectors and a high resolution Time-Of-Flight system.

The fixed target experiment WA98 is a large-acceptance photon and hadron spectrometer designed to study ultra-relativistic heavy-ion collisions. Charged particles, produced in the interactions, traverse a large magnet and are deflected into two tracking arms, horizontally placed on both sides of the beam which allow for momentum determination and particle identification. For the Δ^{++} measurements, reported in this paper, we use the full data sample from the tracking arm for the positively charged particles [11]. This second tracking arm was installed and operated for only a portion of the final WA98 run period.

The tracking arm consists of two planes of Multi-Step Avalanche Chambers (MSACs) [12,13] and two planes of streamer tube detectors, all equipped with electronic pad readout and a highly segmented Time-Of-Flight (TOF) wall. Fig. 1a shows a schematic drawing of the second tracking arm as seen from above, with two tracks entering the acceptance. Here the z -axis is pointing along the beam and the x -axis is parallel to the bending plane of the magnet. The position resolution of the MSACs was $\sigma_x = 0.5$ mm in the horizontal direction, and $\sigma_y = 1.7$ mm in the vertical direction whereas the streamer tube detectors had an intrinsic resolution of $\sigma_x = 3.0$ mm and $\sigma_y =$

6.5 mm. The time resolution of the TOF wall was better than 90 ps and its spatial resolution was $\sigma_x = 12.5$ mm and $\sigma_y = 26.4$ mm. Fig. 1b and 1c show p versus $t_{\text{tof}} - t_{\text{exp}}$ assuming pion and proton mass, respectively. Here p is the momentum, t_{tof} the measured flight time of the particle and t_{exp} the expected flight time calculated from the track length and momentum of the particle. Separation between different particle species, especially for pions and protons, is good over a wide range of momenta. Kaons and pions are no longer separable at momenta above 4 GeV/c and thus a small contamination of kaons is present among the pions at larger momenta. The momenta of the particles are first approximated assuming a uniform magnetic field and straight line fits through the tracking arm and then corrected by GEANT [14] calculations using the measured field. The momentum resolution, $\Delta p/p$, is limited by the multiple scattering, mainly in the air between the target and the detectors, the intrinsic detector resolution and by methodical uncertainties. Based on GEANT simulations we estimate $\Delta p/p$ to be about 1% at 2 GeV/c and 2% at 5 GeV/c.

The most interesting events are those where the bulk of the nuclear matter interacts, i.e. the most central events. A trigger based on the transverse energy as measured by the Mid-Rapidity Calorimeter (MIRAC) is used to enhance central collisions. The present analysis has been performed using the 8.5% most central events of the WA98 minimum bias cross section (6450 mb for the used data set) based on an offline cut on the measured transverse energy. To reject beam particles other than Pb and possible event pile-up, lower and upper cuts in the ADC and TDC values from the start-counters, placed in the beam, were performed.

During and shortly after electrical discharges, the MSACs exhibited reduced efficiencies. This has been discussed in a previous paper [12]. Thus events recorded within a short time after such a discharge, are removed from the analysis.

The tracking procedure connects hits in at least three out of the four tracking planes, by means of straight line fits, and combines a track with a valid time measurement in the TOF wall at the correct position. Due to the excellent two-track resolution and two-dimensional position resolution of the tracking planes, this procedure works almost without

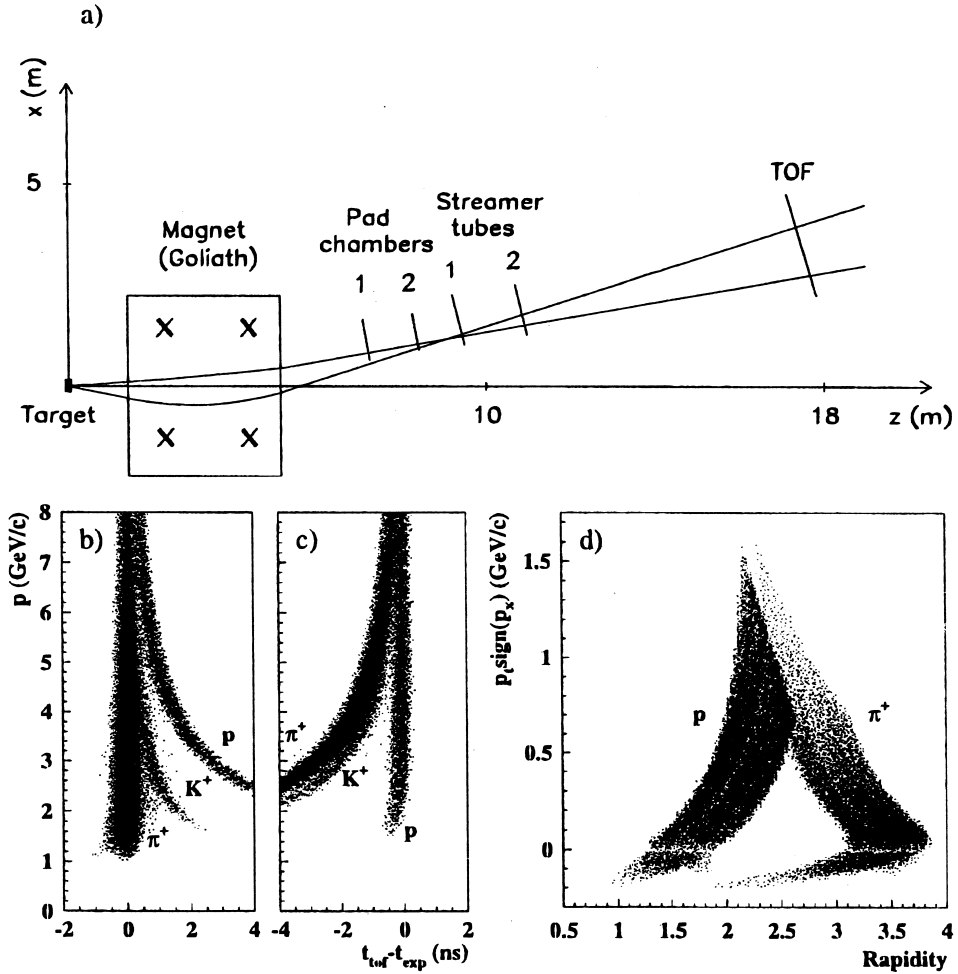


Fig. 1. (a) Overview of the tracking arm with two tracks within the acceptance. (b) Particle identification bands calculated assuming that all particles have the pion mass. (c) as in (b) assuming proton mass. (d) The distribution of accepted particles in terms of p_t and rapidity for protons and π^+ .

ambiguities, in spite of the large track multiplicity within the acceptance. Cuts have been applied on the hit association in the TOF wall and on the vertical distance between the track extrapolation and the interaction point. Finally, the particle identity is obtained by cuts in $t_{\text{tof}} - t_{\text{exp}}$. This works up to a particle momentum of 8 GeV/c, where the separation no longer can be done unambiguously. In order not to lose any observed Δ^{++} resonances, we have chosen to use particles up to 16 GeV/c, thereby introducing a small systematic error. The small amount of contaminating kaons among pions above

4 GeV/c only gives marginal effects on the extracted Δ^{++} yield. This sort of contamination will also be present in the mixed events and its effects are to a large extent removed.

Fig. 1d shows the distributions of accepted particles for the second tracking arm in terms of transverse momentum p_t and rapidity for protons and pions. Notice the $\text{sign}(p_x)$ factor, which unfolds the spectrum for particles with negative p_x and momentum low enough to bend across the beam line. Furthermore, a momentum cut of 8 GeV/c has been applied.

For all pairs of identified p and π^+ , the invariant mass, M_{inv} , was calculated from

$$M_{\text{inv}} = \sqrt{(E_\pi + E_p)^2 - (\mathbf{p}_\pi + \mathbf{p}_p)^2}.$$

The mass resolution of the $p\pi^+$ -pair, estimated from the momentum resolution, is a few MeV. An invariant mass spectrum of such pairs (real spectrum) will consist of one part where the pion and the proton are coming from the same Δ^{++} -decay and an essentially uncorrelated combinatorial background. Due to the high multiplicity of protons and pions, the combinatorial background will be by far the dominant contribution to the invariant mass spectrum. To account for this combinatorial background, the invariant mass spectrum was calculated also with protons and pions taken from different events (mixed event). To extract the fraction ξ , of Δ^{++} , among the $p\pi^+$ -pairs, N_{pair} , we assume that the mixed event invariant mass spectrum has the same shape as the combinatorial background in the real spectrum. This assumption has been verified by studies of ratios between real spectra and mixed event spectra. To essentially eliminate the statistical errors in the mixed event spectrum, it contains about ten times the statistics in that of the real spectrum. The real spectrum, $F(M_{\text{inv}})$ can then be written as

$$F(M_{\text{inv}}) = N_{\text{ev}} \cdot N_{\text{pair}} (\xi \cdot BW(M_{\text{inv}}, M_0, \Gamma) + (1 - \xi) g(M_{\text{inv}})). \quad (1)$$

$BW(M_{\text{inv}}, M_0, \Gamma)$ is a modified Breit-Wigner function, filtered through our geometrical acceptance, normalized to unity. M_0 and Γ are the peak position and width respectively of the modified Breit-Wigner function. Note that neither the real spectrum nor the mixed event spectrum are corrected for acceptance. N_{ev} is the number of events and $g(M_{\text{inv}})$ is the unit normalized mixed event spectrum. The modified Breit-Wigner function, before filtering, is given by

$$BW(M_{\text{inv}}, M_0, \Gamma) \propto \frac{q^3}{(q^3 + \mu^3)} \frac{1}{((M_{\text{inv}} - M_0)^2 + (\Gamma/2)^2)},$$

where q is the momentum of the proton (or pion) in the rest-frame of the pair, i.e half of the relative momentum, and $\mu = 180 \text{ MeV}/c$ [15]. The real spectrum can now be fitted using Eq. (1), treating ξ , M_0 and Γ as free parameters.

Fig. 2a shows the distribution of accepted Δ^{++} obtained from FRITIOF7.02 [16] events filtered through GEANT, i.e. for Δ^{++} where both decay particles fall inside the acceptance of the arm. The spectrum is unfolded in the same way as in Fig. 1d. Fig. 2b shows the invariant mass spectrum of

$$F(M_{\text{inv}}) - N_{\text{ev}} \cdot N_{\text{pair}} \cdot (1 - \xi) g(M_{\text{inv}}),$$

i.e. the real spectrum with the background subtracted. Also shown by the solid curve is

$$N_{\text{ev}} \cdot N_{\text{pair}} \cdot \xi \cdot BW(M_{\text{inv}}, M_0, \Gamma),$$

i.e. the acceptance-filtered modified Breit-Wigner function obtained from the best fit.

The extracted number of Δ^{++} has to be corrected for acceptance and inefficiencies. Table 1 gives the values of the different correction factors with their estimated errors.

The efficiency for Δ^{++} detection is the product of the efficiencies for protons and pions. The efficiency factors given in the table are the ratio between those Δ^{++} efficiencies and the corresponding efficiencies for protons. k_{trk} , which is about 80%, is the probability for a particle entering the arm, resulting in a track seen in at least three out of the four

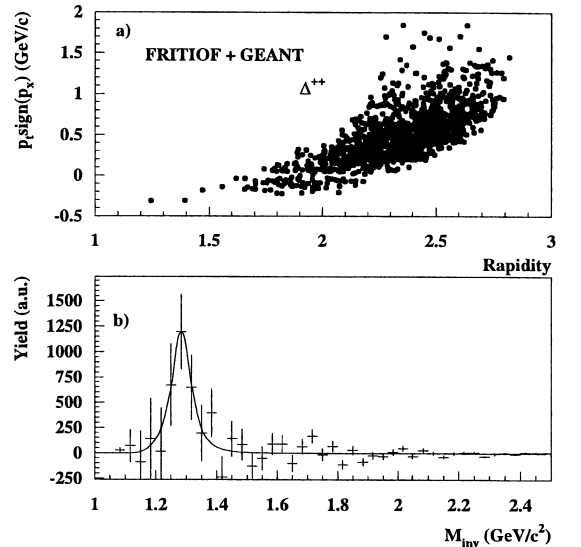


Fig. 2. (a) The distribution of accepted Δ^{++} obtained from Fritiof events. (b) The extracted Δ^{++} resonance together with the corresponding acceptance-filtered modified Breit-Wigner.

Table 1

Summary of the different correction factors and their estimated systematic errors.

Correction factors	Value
tracking efficiency, k_{trk}	0.79 ± 0.02
identification efficiency, k_{pid}	0.60 ± 0.02
geometrical acceptance, k_{geo}	0.145 ± 0.005

tracking planes and with a quality sufficient to pass the applied cuts, i.e. vertex association, χ^2 of the straight-line fit, et cetera. The k_{pid} factor corrects for the particle identification efficiency, including hardware efficiencies, effects of applied cuts on the flight times and particles decaying before reaching the TOF wall. The k_{geo} factor corrects the Δ^{++} /proton ratio for the limited azimuthal coverage of the arm estimated by GEANT simulations. The values of all the correction factors depend on the cuts we apply on the data and the systematic errors were estimated by varying these cuts within reasonable limits.

Table 2 gives the reconstructed and corrected ratio between the number of Δ^{++} and protons within the arm. Within our acceptance RQMD2.3 [17] predicts about 2.4 protons/central event and FRITIOF7.02 predicts about 5.5 protons/central event. Thus our proton multiplicity, which is about 1.83 proton per central event after efficiency corrections, seem to be in fair agreement with RQMD, whereas FRITIOF seems to overestimate.

The extraction of the Δ^{++} signal is by no means trivial as the peak is broad and the combinatorial background is large. Three different extraction methods were applied to simulated data to investigate the influence of the methods on the reconstructed number of Δ^{++} [18]. The method described above proved to be the most robust for different projectiles p, Si and Pb upon Pb target at the relevant beam energy.

Regarding the error of the extracted ratio we note that this is dominated by the statistical fluctuations in the number of combinatorial pairs under the resonance peak. Thus it is impossible to obtain the ratio with higher precision with the given statistics, independent of the extraction method. A study based on simulation results with different event generators, and variation of cuts applied to the data, indicates that the systematic error contributions resulting from the various cuts and correction factors applied to the

data are considerably smaller (of the order of 10% of the obtained value) and therefore negligible in comparison to the statistical error.

However, it was observed that the chosen extraction method tended to systematically overestimate the number of Δ^{++} in simulations. A special simplified Monte Carlo event generator was constructed in order to study this effect. With this generator, several hundreds of samples of the same size as the real data sample was studied [19]. The reason for the overestimation is that although the background estimated with mixed events is almost identical to the background in the data, small differences are present. For instance, correlations between the decay products from different Δ^{++} resonances are believed to add to the systematic error of the extraction method. Pairs with the pion and proton from two different Δ^{++} decays, are almost identical to a pair originating from the same Δ^{++} due to the restricted acceptance of the tracking arm. The magnitude of the overestimation and associated error has been determined from the simulations and a correction has been applied for the ratio and error as shown in Table 2. The correction leads to an increased relative error in the ratio.

The ratio of $\Delta(1232)$ /nucleons has been studied and an increase as a function of incoming beam energy has been established [8]. In a thermal model this can be interpreted as an increase of the freeze-out temperature which determines the relative population of the nucleonic resonances. The same ratio can be estimated from our data. In an isospin symmetric system, one could obtain the total number of $\Delta(1232)$ resonances, i.e. Δ^- , Δ^0 , Δ^+ and Δ^{++} , by multiplying the number of Δ^{++} by an isospin factor four. In the same way, the number of nucleons, including those from resonance decays, could be estimated by multiplying the measured number of protons with a factor two. In our case, where we have an isospin

Table 2
Summary of the results.

119677 central events	Δ^{++} /proton ratio
reconstructed (uncorrected)	0.031 ± 0.015
corrected for systematic fitting error	0.021 ± 0.013
full ϕ and eff. corrected	0.309 ± 0.190

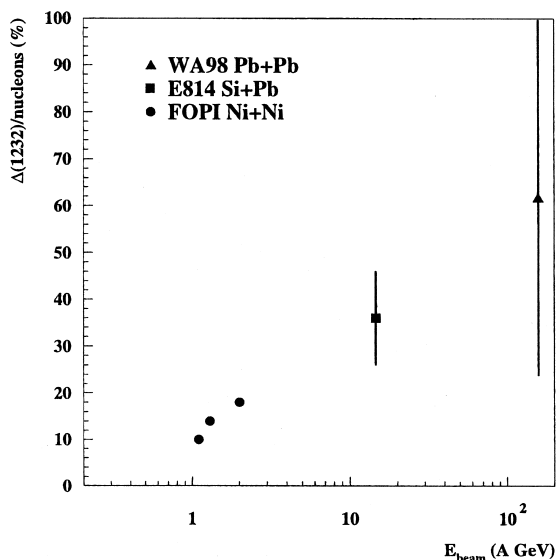


Fig. 3. The ratio $\Delta(1232)/\text{nucleons}$ as a function of beam energy/nucleon.

asymmetry, in a first approximation the nucleons and the Δ -resonances are affected in the same way, and thus no correction for the isospin asymmetry is applied. Only a small contribution of baryon number is present in deuterons and weakly decaying hyperons, where the decay proton might be lost in the tracking due to the secondary vertex being far from the interaction point.

Our obtained ratio for nucleons originating from $\Delta(1232)$ resonances, is found to be quite large at central rapidities, 0.62 ± 0.38 . Fig. 3 shows our results in comparison with similar results from experiments at lower beam energies. Note that the target and projectile rapidities are separated by 5.8 units at 158 A GeV. In this experiment the influence of spectator matter is thus much less than at lower beam energies.

Our obtained value of the $\Delta(1232)/\text{nucleon}$ ratio can be compared to the ratio obtained from thermal model calculations, assuming chemical and thermal equilibrium. In such a calculation the maximum ratio obtained is around 0.33 [2]. Furthermore this ratio is obtained over a large range of temperatures and baryon densities, used as input to the calculations.

However, it should be pointed out that the experimental ratio also contain contributions from prior to

freeze-out. For this and other reasons, e.g. the saturation of the ratio as a function of temperature, it is premature to use the experimentally extracted ratio for a precise temperature estimation and any temperature above 100 MeV seems to be in qualitative agreement with the obtained ratio.

Besides the yield, the fitting procedure also provides the width and mass of the delta peak. However the systematic errors in these values, estimated by changing cuts and extraction methods and by applying the methods to Monte Carlo samples with known parameters, are sufficiently large to preclude a meaningful discussion of a possible mass shift or changes of the width of the delta peak.

Acknowledgements

This work was supported jointly by the German BMBF and DFG, the US DOE, the Swedish NFR and FRN, the Dutch Stichting FOM, the Stiftung für Deutsch-Polnische Zusammenarbeit, the Grant Agency of the Czech Republic under contract No. 202/95/0217, the Department of Atomic Energy, the Department of Science and Technology, the Council of Scientific and Industrial Research and the University Grants Commission of the Government of India, the Indo-FRG Exchange Program, the PPE division of CERN, the Swiss National Fund, the INTAS under Contract INTAS-97-0158, ORISE, Grant-in-Aid for Scientific Research (Specially Promoted Research & International Scientific Research) of the Ministry of Education, Science and Culture, the University of Tsukuba Special Research Projects, and the JSPS Research Fellowships for Young Scientists. ORNL is managed by Lockheed Martin Energy Research Corporation under contract DE-AC05-96OR22464 with the US Department of Energy. The MIT group has been supported by the US Dept. of Energy under the cooperative agreement DE-FC02-94ER40818.

References

- [1] S.A. Bass et al., Phys. Rev. C 50 (1994) 2167.
- [2] G.E. Brown, J. Stachel, G.M. Welke, Phys. Lett. B 253 (1991) 19.

- [3] J.M. Laget, *Phys. Rep.* 69 (1981) 1.
- [4] J.S. O'Connell, B. Schröder, *Phys. Rev. C* 38 (1988) 2447.
- [5] R.E. Chrien et al., *Phys. Rev. C* 21 (1980) 1014.
- [6] J.P. DeBrion et al., *Phys. Rev. Lett.* 34 (1975) 910.
- [7] A. Badalà et al., *Phys. Rev. C* 54 (1996) R2138.
- [8] FOPI Collaboration, B. Hong et al., *Phys. Lett. B* 407 (1997) 115.
- [9] E814 Collaboration, J. Barrette et al., *Phys. Lett. B* 351 (1995) 93.
- [10] WA98 Collaboration, Proposal for a large acceptance hadron and photon spectrometer, 1991, Preprint CERN/SPSLC 91-17, SPSLC/P260.
- [11] L. Carlén et al., *Nucl. Instr. and Methods A* 431 (1999) 123.
- [12] L. Carlén et al., *Nucl. Instr. and Methods A* 412 (1998) 361.
- [13] L. Carlén et al., *Nucl. Instr. and Methods A* 413 (1998) 92.
- [14] R. Brun, F. Carminati, GEANT Detector Description and Simulation Tool, CERN Program Library, Long Writeup W5013, March 1994.
- [15] E.L. Hjort et al., *Phys. Rev. Lett. E* 79 (1997) 4345.
- [16] H. Pi, *Comp. Phys. Comm.* 71 (1992) 173.
- [17] H. Sorge, *Phys. Rev. C* 52 (1995) 3291.
- [18] K. El Chenawi, Ph.D. thesis, Lund University, 1999.
- [19] D. Silvermyr, Lic. thesis, Lund University, 1999.

Curriculum Vitae

General:

Name: Susumu Sato
Date of birth: 26, September, 1969 in Amagasaki, Hyogo, Japan
Domicile: Maizuru, Kyoto
Marital Status: Unmarried

Education:

1976-1978 Naruo-Higashi Elementary School, Nishinomiya, Hyogo
1978-1981 Japanese International School in Duesseldorf, Germany
1981-1982 Naruo-Higashi Elementary School, Nishinomiya, Hyogo
1982-1985 Hama-Koushien Junior High School, Nishinomiya, Hyogo
1985-1988 Ikeda Senior High School attached to National Osaka
Kyouiku University, Ikeda, Osaka
1989-1993 University of Tsukuba, College of Natural Science
1993-1998 University of Tsukuba, Graduate School of Physics
1995.3 Master of Science, University of Tsukuba

Employment:

1998-present Research Associate, Institute of Physics,
University of Tsukuba

